

Spring 4-9-2018

An exploration of the optical detection of ionizing radiation utilizing modern optics technology

Sean D. Fournier

The University of New Mexico, Sandia National Laboratories

Adam Hecht

The University of New Mexico

Cassiano de Oliveira

The University of New Mexico

Jeffrey B. Martin


Sandia National Laboratories

Richard K. Harrison

Sandia National Laboratories

See next page for additional authors

Follow this and additional works at: https://digitalrepository.unm.edu/ne_etds

 Part of the [Atomic, Molecular and Optical Physics Commons](#), [Electromagnetics and Photonics Commons](#), [Nuclear Commons](#), [Nuclear Engineering Commons](#), [Optics Commons](#), and the [Systems Engineering and Multidisciplinary Design Optimization Commons](#)

Recommended Citation

Fournier, Sean D.; Adam Hecht; Cassiano de Oliveira; Jeffrey B. Martin; Richard K. Harrison; and Charles Potter. "An exploration of the optical detection of ionizing radiation utilizing modern optics technology." (2018). https://digitalrepository.unm.edu/ne_etds/67

This Thesis is brought to you for free and open access by the Engineering ETDs at UNM Digital Repository. It has been accepted for inclusion in Nuclear Engineering ETDs by an authorized administrator of UNM Digital Repository. For more information, please contact disc@unm.edu.

Author

Sean D. Fournier, Adam Hecht, Cassiano de Oliveira, Jeffrey B. Martin, Richard K. Harrison, and Charles Potter

Sean Donovan Fournier

Candidate

Department of Nuclear Engineering

Department

This thesis is approved, and it is acceptable in quality and form for publication:

Approved by the Thesis Committee:

Adam Hecht, PhD, Chairperson

Cassiano de Oliveira, PhD

Jeffrey Martin, PhD

Richard Harrison, PhD

Charles Potter, PhD

**AN EXPLORATION OF THE OPTICAL DETECTION OF
IONIZING RADIATION UTILIZING MODERN OPTICS
TECHNOLOGY**

SAND2018-3699 T

BY

SEAN DONOVAN FOURNIER

BS NUCLEAR ENGINEERING

THESIS

Submitted in Partial Fulfillment of the
Requirements for the Degree of

**Master of Science
Nuclear Engineering**

The University of New Mexico
Albuquerque, New Mexico

May 2018

AN EXPLORATION OF THE OPTICAL DETECTION OF IONIZING RADIATION UTILIZING MODERN OPTICS TECHNOLOGY

by

Sean Donovan Fournier

B.S., Nuclear Engineering, University of New Mexico, 2010

ABSTRACT

Modern ultraviolet (UV) cameras, when combined with UV-transmitting lenses/filter arrangements, can be used to detect radiation dose in air. Ionizing radiation excites nitrogen molecules in ambient air, the resulting decay includes weak emission of ultraviolet photons. Previous work has proven this phenomenon is detectable using highly-sensitive electronically cooled cameras traditionally used in astronomy for low-background imaging. While the ability to detect the presence of radiation (i.e. qualitative measurement) has been demonstrated at Sandia National Laboratories, there are several challenges in correlating images to known dose-fields (quantitative measurement). These challenges include: a low signal to background ratio, interferences due to electronic noise and direct radiation interactions with the camera, and a complex source-dependent detection efficiency. Based on measurements of low-level radioactive sources as well as high-level sources at several irradiation facilities at Sandia National Laboratories, researchers are developing deeper understanding of these challenges in an attempt to engineer a system that can be used for quantitatively measuring radiation dose fields remotely. This thesis will describe these efforts and share the lessons learned from several experiments.

Table of Contents

I. Introduction.....	1
Molecular Spectroscopy.....	1
Ionizing Radiation.....	6
Alpha Radiation	7
Beta Radiation.....	7
Gamma and X Ray Radiation	8
Neutron Radiation.....	9
Other Energetic Particles	10
Nitrogen Florescence	11
Photon Yield of Nitrogen Florescence.....	13
Optical Detection of Radiation (ODR)	16
Overview of ODR.....	17
Prior Work	19
Our Approach to ODR	24
II. Optical filtering techniques.....	27
Sources of Optical Background	27
Optical Filtering.....	30
Determination of Transmissivity	31

Determination Out-of-Band Blocking Fraction	37
Effect of angle on transmissivity	42
Summary of Optical Filtering Optimization	47
III. Image Processing	50
Contrast and Signal-to-noise Ratio (SNR).....	53
IV. Light Detection for Imaging	57
Light Collection Techniques.....	57
Charge Coupled Device (CCD) Cameras	58
Optimization of Acquisition Settings for the ODR Application.....	61
Standard Acquisition Settings for the ODR application.....	61
Laboratory Setup for Acquisition Optimization	64
The Effect of Electronic Superpixel Binning on Detection Sensitivity	71
The Effect of CCD Temperature on Noise Reduction.....	76
The Effect of Acquisition Time on Detection Sensitivity and Background	79
Summary of Lessons Learned in Evaluating Acquisition Settings.....	84
Sandia's ODR Configurations	87
V. Optical Detection of Ionizing Radiation Tests.....	92
Po-210 Source in a Dark Box	92
Po-210 Source in a Dark Room	94

Cs-137 Shepherd Irradiator.....	96
Irradiated Yttrium-90 at the Annular Core Research Reactor at Sandia National Laboratories	98
VI. Conclusions.....	102
Summary.....	102
Potential Future Applications for ODR	104
Future Considerations for ODR Optimization.....	106
VII. References.....	108
VIII. Appendices.....	112
Appendix A: Andor camera automation code	112
Appendix B: ImageJ Image processing code.....	115
Appendix C: Transmissivity Curves of Single Filters	117

List of Figures

Figure 1: Dinitrogen Jablonski diagram	12
Figure 2: Filter transmission testing apparatus	33
Figure 3: Transmissivity curve of a single and double-filter stack.....	39
Figure 4: Parallel filter stack diagram.....	40
Figure 5: Off-parallel filter stack diagram.....	41
Figure 6: Effect of off-parallel filter stacking.....	43
Figure 7: Modified apparatus to determine the effect of off-angle light on transmissivity	44
Figure 8: Transmission band as a function of angle for the off-axis light experiment.....	45
Figure 9: Passband centroid as a function of filter angle.....	46
Figure 10: Passband sharpening effect.	48
Figure 11: ImageJ image processing algorithm flowchart.....	55
Figure 12: Quantum Efficiency (QE) curves	66
Figure 13: ET340BP10 stack transmission curve.....	68
Figure 14: ET340BP10 stack transmission curve in UV.....	68
Figure 15: Acquisition setting optimization experiment target image and apparatus	70
Figure 16: A visual description of electronic binning	73
Figure 17: Results from the binning evaluation experiment.....	74

Figure 18: Effect of deep thermoelectric (TE) cooling on CCD image noise.	78
Figure 19: The effect of acquisition time on ODR measurements.	81
Figure 20: Drawing of tungsten polymer camera shield.....	83
Figure 21: Optical Design of the Pathfinder and Demonstrator Systems.....	88
Figure 22: An image of a common 200 μ Ci Po-210 source compared with modeling results.	94
Figure 23: Camera comparison using the 40 mCi Po-210 source in a dark room	95
Figure 24: The Shepherd Irradiator.....	96
Figure 25: ODR measurement of the Shepherd port	97
Figure 26: ACRR foil experiment test configuration.	99
Figure 27: Results from the Y-90 foil irradiation experiment.	100
Figure 28: SP650 Transmission	117
Figure 29: ET360BP10 Transmission.....	118
Figure 30: ET360BP5.5 Transmission.....	119
Figure 31: ET340BP10 Transmission.....	120
Figure 32: Single-filter transmission zoomed scale comparison	121
Figure 33: 2X Dual Band filter stack transmission, full scale	122
Figure 34: 2X dual band filter stack transmission, zoomed scale.....	123
Figure 35: 2X ET360BP5.5 filter stack transmission, full scale.....	124

Figure 36: 2X ET360BP5.5 filter stack transmission, zoomed scale 125

Figure 37: 2X ET340BP10 filter stack transmission, full scale..... 126

Figure 38: 2X ET340BP10 filter stack transmission, zoomed scale 127

List of Tables

Table 1: Nitrogen fluorescence lines observable in ODR	16
Table 2: Optical Filters at Sandia for the ODR application.....	37
Table 3: Results from the off-axis light experiment	45
Table 4: Optimized filter stacks constructed at Sandia for the ODR application.....	49
Table 5: Acquisition settings evaluated for ODR application	71
Table 6: Quantitative image results of the binning evaluation experiment	75
Table 7: Detection Efficiency of the Pathfinder ODR System	89
Table 8: Detection Efficiency of the Demonstrator ODR System.....	90
Table 9: Detection Efficiency of the Compact ODR System	91

List of Equations

Eq. 1: General Filter Transmission	31
Eq. 2: Filter Transmissivity	36
Eq. 3: Contrast	53
Eq. 4: Signal-to-noise Ratio	54

Acronyms

1N	first negative system of ionized dinitrogen molecule
2P	second positive system of dinitrogen molecule
ACRR	Annular Core Research Reactor
AMU	atomic mass unit
CCD	charge coupled device
CIC	clock-induced charge
COTS	commercial off-the-shelf
EMCCD	electron-multiplied charge coupled device
ENSDF	Evaluated Nuclear Structure Data File
FWHM	full-width at half maximum
GIF	Gamma Irradiation Facility
iCCD	intensified charge coupled device
IR	Infrared
LED	Light-emitting diode
MCP	multi-channel plate
NIR	near-infrared
ODR	optical detection of radiation
QE	quantum efficiency
RGDs	radiation generating devices
SNL	Sandia National Laboratories
SNR	signal-to-noise ratio

TBP	tributyl phosphate
TE	thermoelectric
UK	United Kingdom
UV	ultraviolet
W-Halogen	tungsten-halogen

I. INTRODUCTION

Recent developments in optics technology, namely improvements to optical filtering and CCD camera chips, have made it possible to detect the fluorescence of nitrogen in air due to ionizing radiation or rather, to perform the optical detection of radiation henceforth referred to as ODR in this composition. This report will present a brief overview of molecular spectroscopy and the process of fluorescence, ionizing radiation, and how it can be observed with modern imaging equipment. Following the process from source to image data, this report will describe each component of the equipment used in recent experiments including optical filtering, light collection, light detection and imaging, image processing, and data presentation. Within each chapter, the results of several optimization experiments will be presented that demonstrate some of the nuances of ODR and suggest ways of optimizing the technique. The purpose of this report is to present a broad survey of this very new technique in radiation detection for the scientific community.

Molecular Spectroscopy

Molecules, like free atoms, exhibit quantum-mechanics of electron orbitals and transitions. Electrons, existing in bonds as well as outside of bonds exist in orbitals described by the systems wavefunctions, the energies of which are predictable through quantum mechanical analysis in simple molecules. Through this analysis, the absorption and emission spectra of some molecules can be predicted, and through measurement of these spectra, a great deal is learned about the physical and chemical properties of matter.

Molecules have six major degrees of freedom. Translation relates to the movement of the entire molecule in space from one place to another. While not specifically important to spectroscopy itself, the effects of translational motion are observable as features in the spectrum, which will be discussed later. Electrons occupy either bonding or non-bonding orbitals described by the system's wavefunctions. The energies of these orbitals are predictable through quantum mechanical analysis. Vibrational motion between the atoms in molecules essentially changes of the length of the molecular bond and gives rise to observable changes in energy. Rotational motion is also considered to be an important degree of freedom as it can be manipulated by photons and also gives rise to signatures in the observable spectrum. Electron orbital configuration is very important to spectroscopy as it is the principal defining factor of an electronic state for a molecule. Electron spin is another degree of freedom within the electron orbital and it drives many of the state configuration selection rules for allowable and forbidden state transitions. Finally, nuclear spin is the spin of each atom's nucleus independent of electron configuration and is the last degree of freedom.

The physics of diatomic molecules (like N_2) are of interest in this work. Diatomic molecules are molecules comprised of only two atoms bound together by electronic forces. Diatomic molecules are categorized as homonuclear, comprised of two similar atoms, and heteronuclear, comprised of two different atoms. Homonuclear molecules such as N_2 exhibit parity symmetry which simplifies the selection rules as they pertain to allowable and forbidden electronic transition states.

The electronic structure of molecules is described with what are called term symbols. Each electronic state will have a term symbol that describes its parity and orbital symmetry. The term symbol takes the form of $^{2S+1}\Delta_{u,g}^{\pm}$. The symbol S is the spin quantum number. The symbol, Δ describes the projection of the orbital angular momentum along the internuclear axis which relates to molecular symmetry. For homonuclear, diatomic molecules, u,g relate to the parity of the molecule. And finally, \pm , for $\Delta=\Sigma$ states describe the symmetry along the arbitrary internuclear axis plane. This symbol is left out when there is no possible anti-symmetry (when $\Delta=\Pi$).

Radiations from homonuclear, diatomic molecules are due to, in order of increasing energy, changes in rotational motion, changes in vibrational motion, and electronic transitions from shell to shell. Unlike atomic spectra which are due to only electronic transitions, the addition of the rotational and vibrational degrees of freedom give rise to complex spectra. Because of these complicating factors, detailed quantum mechanical modeling is often used to predict spectral characteristics for given molecules.

Spectroscopy is the study of these energetic transitions that shed light on the atomic and/or molecular bonding physics and in turn, the chemistry of the matter being observed. Spectroscopy can be carried out indirectly, by observing the net absorbance of a particular wavelength (or even a range of wavelengths) of light shining upon a sample of a given molecule or directly by the observation of the de-excitation of molecules. The observed results from such measurements tell us how the chemical bonds are structured in these molecules and how they behave when energy is added to the system or when it is emitted.

This work involves observing the electronic state transitions of the N_2 molecule through the process of fluorescence. When energy is absorbed by a molecule it is excited into a higher energy vibrational level. The excited molecule can collide with surrounding molecules producing heat through the process of relaxation. In relaxation, the excited electrons in the molecule de-excite through the various vibrational energy levels of the excited state through these collisions. When the molecule is in the ground level of the excited state, the molecule may spontaneously de-excite into its ground state by emitting a photon that carries away energy equal to the difference between the energy of the excited and ground states. This process is referred to as fluorescence. Fluorescence occurs relatively quickly as compared to the similar process of phosphorescence but much more slowly than vibrational and rotational relaxation processes responsible for heat transfer.

When the molecule exists in a region of space occupied by other molecules with different properties fluorescence can be “quenched” if the other molecules have accepted large quanta of electronic energies. Instead of emitting photons to transition from excited to ground state, the molecule can transfer all the required energy to other molecules via collision before the spontaneous emission occurs. The effect of quenching is more prevalent in aqueous media than in gasses, which have densities that are roughly three orders of magnitude lower.

Observing the light emitted from the process of fluorescence and phosphorescence relates directly to the energy levels of the states involved. The observable spectra emitted from molecules (sometimes referred to as spectral “lines”) are not infinitely sharp. Several types of broadening can occur prior to the observation of the spectra

Doppler broadening is due to molecular temperature. Doppler broadening is manifested by the translational movement of the molecules while they are emitting photons.

Molecules moving toward the observer will appear to be giving off different wavelengths than molecules moving away from the observer. The effect of Doppler broadening is minimized by reducing the temperature of the sample.

Lifetime broadening, also called uncertainty broadening, is described by the uncertainty principle. Since the momentum or position of anything can never be precisely observed radiations are emitted over a narrow bandwidth inversely proportional to the lifetime of the state. As the lifetime of the state increases, the energy range of the emission becomes narrower.

Collisional deactivation is the loss of energy due to collisions with other molecules in the system including those in the wall of the container the sample is in. Collisions can either add or remove small amounts of energy that lead to wider observable lines. Low density samples and large containers can be used to minimize this effect. While there are several phenomena leading to line broadening, the observable spectrum lines of nitrogen molecules have been shown to have very narrow widths of 1-2 nm at normal temperatures and pressures (Waldenmaier, April 2006). As will be discussed later, the passband of optical filters used in ODR, while small, are more than wide enough to pass the entire emission line of interest.

In summary, the N_2 molecule is categorized as a homonuclear, diatomic molecule, the simplest of all molecules. While the atomic structure of individual atoms is similar to that of molecules, the addition of several new degrees of freedom, namely vibrational and

rotational motion, when combined with electronic states, give rise to complex absorption and emission spectra. Through the use of quantum mechanics, the various state transitions and their probabilities can be predicted. Using the technique of spectroscopy, insight is gleaned as to the molecular structure and the physics of molecules. In contrast, the work presented here involves observing the fluorescence light and correlating it to the known emissions of N_2 to glean information about the incident radiation.

Ionizing Radiation

To fully understand the optical detection of radiation we should understand the different types of ionizing radiation and how they interact with matter. Ionizing radiation takes several different forms, each with unique characteristics and challenges for optical detection of radiation (ODR). Through natural decay or induced nuclear reactions by radiation generating devices (RGDs) or nuclear reactors, radiation is produced and can be detected through direct means (ionized atom charge collection) or indirect means (observation of secondary phenomena caused by the radiation interaction). Traditionally, the former method is used in detectors. Radiation interacts with the materials to produce a charge which is collected and processed through electronics to qualify and quantify the radiation field. Some detector systems, however, rely on the detection of secondary phenomena produced by the radiation interaction. Most notably, scintillation is the process by which radiation produces optical emissions from excited atomic electrons in detector media. Materials engineered to enhance their scintillation properties are placed in the radiation field and the light is collected from them by photomultiplier tubes and

processed electronically. ODR leverages this approach but instead utilizes the air itself as a scintillator.

Alpha Radiation

Of the several types of ionizing radiation, alpha radiation perhaps shows the most utility for detection by ODR. Alpha decay is the process by which an alpha particle is emitted from a nucleus. Typically, alpha particles are ejected from the heavier radionuclides and are characterized by having a mass of 4 AMU and a charge of 2^+ . These high-speed helium nuclei deposit most of their energy in a very short distance. A few centimeters of air can effectively stop alpha particles. Since alpha particles stop in such a short distance of air, the density of excited nitrogen molecules is large compared to other forms of radiation. The low external biological hazard and high relative dose rate to activity ratio make the optical detection of alpha radiation more straightforward when compared to the other forms and is a natural starting point to begin this research.

Because of their short range, the dose in air from alpha sources drops off to background only a few centimeters from the surface of the source. Consequently, this type of radiation is generally the easiest to detect and locate using the ODR imaging technique as will be shown later in this work. Because alpha particles are very easily shielded, the source material must be in direct contact with the surrounding air to be observed by ODR.

Beta Radiation

Another type of ionizing radiation detectable by ODR is called beta radiation. Beta radiation results from radioactive beta decay of a nucleus. In beta decay a high energy, high speed electron or positron may be emitted from the nucleus in addition to a neutrino

or anti-neutrino. Beta-minus decay (electron and antineutrino emission) occurs in neutron-rich radionuclides most commonly produced in the nuclear fission process. Beta-plus decay (positron and neutrino emission) occurs in proton rich radionuclides most commonly produced in photonuclear or accelerator-driven nuclear transmutation. Each type of beta decay results in the deposition of energy into matter. The primary interaction for beta particles is ionization, the dislodging of atomic electrons from their bound states.

Beta decay is a three-body physics problem (the nucleus, the beta particle, and the neutrino/antineutrino) and thus particles are emitted in a spectrum of energies rather than discrete quanta like alpha and gamma radiation. Beta particles have an intermediate range in air when compared to other forms of radiation. Higher energy beta particles can travel several meters in air and are shielded by a few millimeters of plastic (low-z) material. Because beta particles strongly interact with matter, they produce a concentrated dose in a region of space but not as dense as alpha particles due to the lower charge and mass of beta particles. Since beta radiation is emitted with a spread of energies, and thus ranges, the dose to air may not be as clear-cut as alpha since the dose is more diffuse than the highly concentrated dose from alpha particles.

Gamma and X Ray Radiation

Not all ionizing radiation takes the form of charged particles, the third type of ionizing radiation is called gamma radiation. Gamma radiation is the result of decay in which a radionuclide de-excites by the emission of a photon from the nucleus. X rays are the result of atomic de-excitation and are characterized by their emission from the electron orbitals rather than the nucleus. Gamma rays and x rays interact with matter similarly by

four major modes. The photoelectric effect, Compton scattering, pair production, and photonuclear reactions are the primary modes of photon interaction with matter for the relevant x-ray and gamma-ray energies. While different physically, each of these modes excite and/or ionize molecules. When compared with the other forms of radiation, gamma-ray and x ray radiation can travel much farther in air between interactions and energy deposition is spread out over much larger volumes which make it more difficult to detect by ODR.

Neutron Radiation

Another neutral particle ionizing radiation is called neutron radiation. Neutrons are emitted from radionuclides through the process of nuclear reactions (induced by incoming particles) or by the process of spontaneous fission. Fission-produced neutrons are emitted with a spectrum of energies. In fission, neutrons are absorbed by heavy nuclei to form a compound nucleus with an excitation energy greater than the fission barrier. De-excitation can cause the compound nucleus to split into two lighter, neutron rich nuclides, prompt gamma rays, and more free neutrons. The neutrons emitted are then available to produce more fissions, thus causing a chain reaction in the fissile (able to be fissioned by a zero-energy neutron) material they pass through.

Neutrons are neutral particles meaning they have no charge and they lose energy not by electronic interaction but by elastic and inelastic collisions with nuclei in the matter they pass through. Neutrons have a similar range in air to gamma rays but are stopped through a process called moderation. Moderation is the process of slowing neutrons down by several collisions. For several materials, neutron capture probabilities are maximized at lower energies which lead to transmutation. Transmutation is the process

by which a nuclide is made into another by the absorption of a particle, typically a neutron. The resultant nuclide is typically unstable and thus, radioactive. Neutrons can be detected through this process of transmutation or by the nuclear interactions with lighter isotopes such as B-10 and He-3.

The dose from neutrons is spread across large volumes of air which may make it difficult to detect by ODR. Furthermore, neutrons are extremely damaging to semiconductor materials. Neutrons can create defects in CCD chips which over time will yield to a less sensitive camera and permanently damaged pixels. Therefore, shielding is a very important factor in sensor design when neutrons are present.

Other Energetic Particles

Other energetic particles can be produced, not through the radioactive decay of atoms, but by other naturally or synthetically induced nuclear reactions. An example of this is nuclear fission in which a neutron is absorbed into a heavy nucleus and introduces enough energy to split the atom into fission products and more neutrons. These fission products are often much heavier than alpha particles and quickly slow down in the presence of matter, freeing many electrons from surrounding atoms during the slowing down process. Because of their size and charge, these fission products do not travel much farther beyond the atomic scale in solid or liquid materials. The extremely localized dose from these particles make them good candidates for localized measurements using ODR.

High energy particles and gamma rays from astronomical bodies strike the earth's atmosphere and produce secondary particle showers. These particles deposit dose in the

atmosphere and lead to the excitation of molecules. Aurora is a natural phenomenon observable by the naked eye caused by solar wind particles funneled by the earth's magnetic field to the poles of the earth. Concentrated radiation interacting with the atmosphere produces a spectrum of light. In addition to solar wind particles, cosmic rays from far-off astronomical processes interact with earth's atmosphere to produce fluorescence that has been observable on earth with the use of telescopes. In fact, this is one of the first uses of ODR in the scientific community and will be discussed in more detail later.

Nitrogen Florescence

Nitrogen, being very abundant in nature, is very well known in the molecular spectroscopy community. Its excited states have been heavily studied and are very well documented (G. Herzberg, 1950). In fact, the N_2 molecule is often used in undergraduate physical chemistry coursework to demonstrate the basic principles of molecular spectroscopy (Bayram & Freamat, 2012). While the molecular structure of nitrogen can quickly become complicated as shown by the several dozen systems of vibration states and transitions data there are two transitions that are the most observable in nitrogen as it exists in the atmosphere (see figure 1) (Lofthus & Krupenie, 1977). The excitation process can ionize the nitrogen molecule to yield an excited state of N_2^+ . The most relevant system of the ionized nitrogen molecule is called the first negative system of N_2^+ (1N) and involves the transitions from the $B^2\Sigma_u$ to the $X^2\Sigma_g$ state. Another system is the transition from the $C^3\Pi_u$ to the $B^3\Pi_g$ state, referred to as the second positive system (2P) of N_2 that yield the most abundant lines in the electromagnetic spectrum (Belz, 2005).

Spin transition selection rules forbid the transition of ground state nitrogen molecules into the $C^3\Pi_u$ state. However, electron exchange and recombination of ionized molecular nitrogen with electrons can bring the molecule into this state (Waldenmaier, April 2006).

The two systems together offer several promising lines in the UV band that can be detected. The transitions are described graphically in the figure below (figure 1).

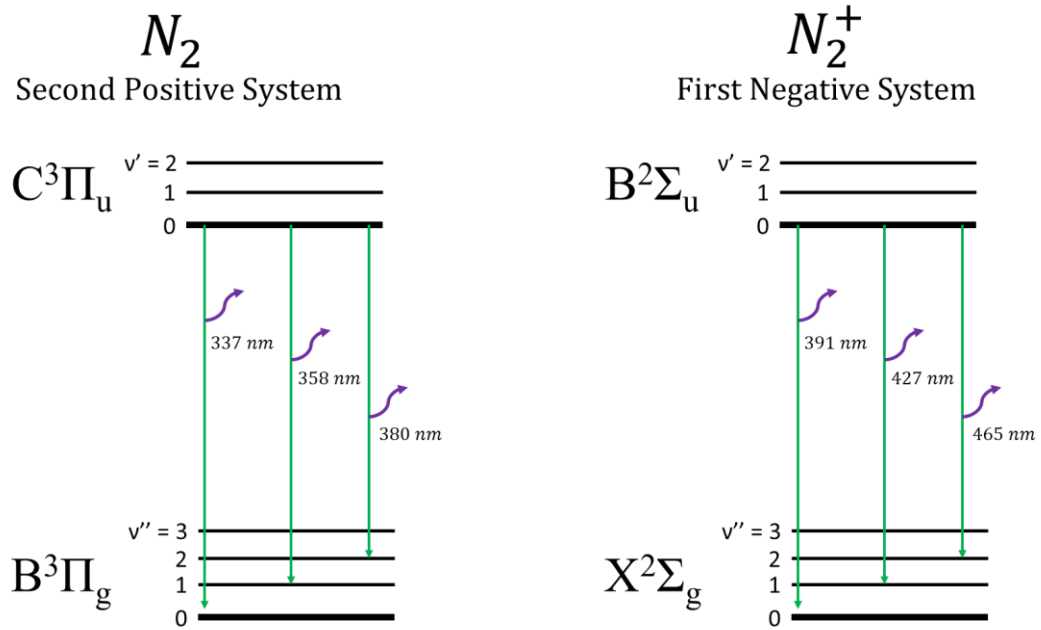


Figure 1: Dinitrogen Jablonski diagram of the second positive and first negative System. Based on a diagram by (Bayram & Freamat, 2012). The figure is simplified to show only the three most abundant fluorescence lines of each system.

The methods by which nitrogen can be excited vary from applying electric fields, or through interaction from ionizing radiation including bombardment by electron beams. Regardless of the means, the excitation of nitrogen molecules involves manipulation of the electrons through an external electric field or through collisions with other electrons. In the case of ionizing radiation, it is the secondary electrons produced from the primary radiation interaction that bring nitrogen molecules into these excited states.

For the second positive (2P) system of N_2 , at least 3.6 eV of energy must be added to the molecule to excite it from the ground level of the ground state to the ground level of the excited state (0-0). (Bayram & Freamat, 2012) Exciting the molecule to higher vibrational states in turn, requires slightly more energy (0-1, 0-2, 0-3, and so on). De-excitation through fluorescence will emit photons with energies equal to the potential energy difference of the states by the law of conservation of energy. Ionizing and exciting the nitrogen molecule into the excited state of the first negative system of N_2^+ requires at least 18.5 eV of energy.

Photon Yield of Nitrogen Florescence

The 2P system of N_2 and 1N system of N_2^+ have transitions that fluoresce photons in the UV region of the electromagnetic spectrum. Each of these transitions has a unique relative intensity that is described through detailed selection rules derived from the quantum mechanical models. Transition yields, or the measure of relative photon intensity for a state transition, are affected by the electronic structure of the molecule as well as the mechanism by which the molecule was excited. Transition yields are also altered by the environment through quenching from other molecules which will be explained later. These factors make it difficult to predict the true yields of the fluorescence lines but many years of experimentation and modeling have led to breakthroughs in the ability to model these phenomena (Belz, 2005) (Waldenmaier, April 2006) (Rosado, Blanco, & Arqueros, 2010) (Rosado, Blanco, & Arqueros, 2014) (Thompson, Barritt, & C., 2016).

Some modeling and experiments have shown that the relative intensities of the various spectral lines are a function of linear energy transfer of the particles exciting the nitrogen

(Thompson, Barritt, & C., 2016) (Sand & Ithantola, 2014) (Rosado, Blanco, & Arqueros, 2014). This means that alpha particles, beta particles, gamma rays, neutrons, and other energetic particles will likely show different fluorescence line yields. This is largely due to the differences in the way these particles produce secondary electrons in the slowing down process. It has been shown that the specific excitation and in turn, the fluorescence yield, is directly proportional to the specific ionization along the particle track (Tatischeff, 1970). In the same study, it was observed that beyond the particle track, a spike in the fluorescence yield indicated that lower-energy secondary electrons more readily recombine with ionized nitrogen molecules leaving them in the second positive system (Stolarski & Dulock, 1967). Due to this fact, radiation that produce lower-energy secondary electrons while slowing down more efficiently produces strong fluorescence. The presence of quenching agents in the air will also affect the overall fluorescence yield. If the transition that would normally spontaneously fluoresce carries an amount of energy that equals an allowable excitation in another molecule, the energy can be directly transferred to the other molecule, without emitting a photon and the fluorescence is said to be quenched. Quenching can be caused by other nitrogen molecules as well as other species in the mixture, most notably oxygen. Several carefully controlled studies have been carried out on the quenching of N₂ fluorescence and have shown that it is largely due to O₂ molecules and can vary with temperature and pressure (Belz, 2005) (Fraga, Onofre, & Pereira, 2008) (Rosado, Blanco, & Arqueros, 2010). Those same studies showed that quenching due to argon is negligible.

The differences in quenching within the range of normal atmospheric conditions is relatively small considering the compounding uncertainties of practical measurement of nitrogen fluorescence in the field. Changes in photonic yield of around 10% for the major lines have been predicted between sea level and 5000-foot elevation (Harrison, Martin, Wiemann, Choi, & Howell, 2015).

Researchers have been able to measure and predict the relative intensity and photonic yield of several lines of the excited nitrogen molecule. Observation of these spectra in field applications are extremely difficult due to high background, electronic noise, attenuation, etc. so only the four most intense spectral lines are considered here to be practically observable in most applications. Table 1 shows a compilation of data on these top fluorescence lines. Three lines of the second positive system of N_2 and the most abundant line from the first negative system of N_2^+ are considered. The relative intensity to the overall most abundant line, 337 nm was measured in air using alpha particles (Brett, et al., 2017). These values are in relatively good agreement with the model results of Thompson and Barritt (Thompson, Barritt, & C., 2016). These yield values are a first link in the chain from dose rate in air to measured light intensity by the ODR system.

Table 1: Nitrogen fluorescence lines observable in ODR

<i>Wavelength (nm)</i>	<i>Excited System</i>	<i>Transition $v' \rightarrow v''$</i>	<i>Relative Intensity[†]</i>	<i>Photons per Decay[‡]</i>	
				<i>Po-210</i>	<i>P-32</i>
316	2P	1 - 0	0.37	11.2 ± 1.6	1.78 ± 0.24
337	2P	0 - 0	1.00	25.2 ± 3.4	3.91 ± 0.45
358	2P	0 - 1	0.67	17.3 ± 2.2	2.58 ± 0.36
391	1N	0 - 0	0.35	4.6 ± 0.3	1.49 ± 0.05

[†] Measurement results from (Brett, et al., 2017) [‡] Model results from (Thompson, Barritt, & C., 2016)

Optical Detection of Radiation (ODR)

Radiation-induced nitrogen fluorescence can be used as a means of detecting the presence of ionizing radiation at distances much farther than conventional direct measurements.

The UV photons created during nitrogen fluorescence have an attenuation length in air of approximately 2500 meters. Gamma rays are the most penetrating form of ionizing radiation other than neutrinos, which are extremely hard to detect. Gamma rays have an attenuation length of only 150 meters. Thus, remotely sensing radioactive materials by direct measurement is impossible at distances farther than this. Using state-of-the-art optics to detect long-range UV photons shows promise in improving the capability of stand-off radiation detection, and has wide-reaching impacts to several health and safety and national security missions.

The purpose of the research presented here is to demonstrate the optical detection of radiation through the use of state of the art technology. This is accomplished by measuring some of the unique radiation sources at Sandia National Laboratories with the goal of advancing the capability to quantify radiation dose fields remotely. Several

challenges still remain in quantifying radiation dose and improving measurement sensitivity and accuracy. These include the presence of a large optical background in the region of interest, low signal-to-noise ratio, direct radiation strikes on the digital camera, and difficult optical paths to source material. The work done as part of this thesis attempts to mitigate these challenges through the use of state of the art technology, novel camera positioning techniques, and experimental design.

Overview of ODR

The practical application of ODR involves the careful collection of light through special UV transmissive optics to a detector system. Light is collected using a system that is either reflective (mirror-based) or refractive (lens-based). These can be engineered to collect light from a specific field-of-view, the frame of a scene for which light can reach the detector. Also, adjustments can be made to the depth-of-field, the standoff distance of a scene for which light will be collected.

Collected light must be filtered heavily to allow for the weak nitrogen fluorescence signals to be detected. Sunlight can easily flood the spectrum in the UV at levels that make localization of nitrogen fluorescence impossible. Manmade light from incandescent, fluorescent, and, to a lesser extent, LED bulbs can emit in the UV and further flood the signal out. Filters can be stand-alone optical components or built into existing mirrors and lenses as carefully engineered coatings. It is important to know how filtering affects the detection efficiency as each filter will add some losses to the overall optical transmission, that when compounded, can hide the signal. Filters can be placed before or after light collection optics depending on the configuration but must be done before the light reaches the detection system.

The collected, filtered, and focused light can be detected several ways. The detection of this light must be highly sensitive in the UV due to the low signal strength and be able to be controlled to adjust acquisition times. Traditional radiation detection equipment used in scintillation-type detectors can be used for counting the light collected by the optics. Photomultiplier tubes take light in, convert the photons to electrons on a photocathode, amplify the electronic signal through dynodes and collect the signal for processing by the signal-chain electronics (preamplification, amplification, analog to digital conversion, single or multi-channel analyzer, acquisition interface electronics). The benefits of using such an apparatus are that PMTs are very sensitive and can be custom-engineered for the light they are collecting. The data from PMTs produces a single measurement of light output which can be useful for careful quantification measurements but make imaging applications difficult. Furthermore, PMTs cannot be operated for long acquisition times due to the large amount of noise encountered in taking an individual measurement. PMTs are more ideal when fast measurements are needed. Imaging with PMTs can be done by employing a scanning method in which individual measurements are taken with careful adjustments to optics in between. The data from each measurement are laced together and overlaid on a visible light image of the scanned field of view. Alternatively, multianode PMTs can be used for imaging but offer much less resolution than solid-state solutions (Montgomery, Cowie, Hoek, Keri, & Seitz, 2012).

Recent advances in solid-state charged coupled device (CCD) light detectors have made them competitive with PMTs by way of overall quantum efficiency. In these types of devices, an array of photon-sensitive pixels is manufactured on a silicon chip. When a photon strikes a pixel, it can create an electron-hole pair that is collected during the

readout step of the acquisition process. Subsequent photons striking the pixel build charge in it until acquisition is complete and the chip is readout. The intensity of the charge built up on the chip correlates to the intensity of light incident on it and is processed to form images. Extremely sensitive cameras have become available in the past decade that are optimized for very low light detection, mostly for astronomy and microcopy applications. These cameras are electronically cooled to reduce the thermal noise in the CCD to a point where very low signals can be observed. Adapting these cameras for the ODR application has proven to be challenging but very rewarding in that highly-resolved images of nitrogen fluorescence can be obtained in a single measurement without careful optical adjustments during acquisition.

Depending on the method used to detect the light, signal processing and image analysis are important steps in the ODR process. Contrast enhancements are often needed due to the low signals observed. Background radiation can interact with the detection systems and produce “hot pixels” that can hide the signal. These outlying signals must be identified through statistical analysis and filtered out to improve image clarity. Signal detection and object identification algorithms can be employed to help the data reviewer detect signals in processed images that the naked eye cannot.

Prior Work

The optical detection of radiation may have been first proposed by Edward Teller during the Manhattan project (Parker, 1958). Light emitted from a nuclear weapon detonated in the atmosphere reaches brightness on the order of that of the sun. Energetic particles interacting with atmospheric molecules produce transient fluorescent effects including

those from nitrogen molecules. Light emitted within a microsecond of the explosion is called the “Teller light” (Glasstone & Dolan, 2006).

A review of the literature shows that ODR has been used for many years by the astronomy community for the detection of very high energy cosmic rays. Using this information, astronomers glean information of astronomical processes that improve our understanding of the universe. As early as 1958, telescopes have been designed to collect nitrogen fluorescence light from earth’s atmosphere in an effort to correlate signals to the incident particle energy (Kampert & Watson, 2012). A significant amount of work by Alan Bunner at Cornell University published in 1967 set the groundwork for the analysis of cosmic rays using the atmosphere as a scintillator (Bunner, 1967). Building upon this groundwork, large telescopes were constructed to improve the signal clarity and increase the chances of observing these events. Utah’s Fly’s Eye detector, first brought online in the early 1970s, was designed to track cosmic ray showers using arrays of PMTs illuminated by large spherical mirrors. This approach led to further breakthroughs in high-energy cosmic ray detection. Using this new approach, scientists could detect particles at energies higher than ever before. The lessons learned in the Fly’s Eye led to the improved detector arrays at the Pierre Auger Observatory in Argentina and the JEM-EUSO telescope that is scheduled to be deployed on the international space station (Abraham, Abreu, & Aglietta, 2010) (Casolino & Adam, 2011).

The applicability of this detection method to astronomy and astrophysics has led researchers to perform very detailed spectroscopic measurements of the phenomenon in

many environments. Building upon this fundamental research, several applications for ODR have been explored by researchers across the world.

Baschenko, with the National Academy of Sciences of Ukraine Institute of Physics, demonstrated ODR in 2004 with a reflective light collection, film-based detection system (Baschenko, 2004). The team was able to observe the signal from a 1 mCi Pu-239 source in the presence of a 5 mCi Co-60 source at a distance of 30 meters. This ODR configuration, while seemingly rudimentary compared to other configurations, showed that ODR is possible at very long distances when the proper collection optics are used. Furthermore, this research shows ODRs applicability to detecting alpha emitters in high dose fields, a common problem in radiation facility surveys.

In 2004-2005 the French showed alpha imaging could be a useful technique for characterizing contamination while decommissioning nuclear facilities (Lamadie & Delmas, 2005). The homemade camera system consisted of a fused silica lens for light collection and a liquid nitrogen cooled backlit CCD with a quantum efficiency of up to 60% in the region between 300 nm and 400 nm. Since no filtering of the signal prior to detection was made, measurements were taken in complete darkness. In one hour, a 3.9 kBq Pu-238 source was reasonably detected. Lamadie also proposed a method for determining an accurate signal-to-noise ratio (SNR) that will be discussed in a later section.

Images were captured of real-world nuclear facility operations to prove the ODR method's applicability. A hot-cell manipulator gripper contaminated by Cm-244 was imaged with Lamadie and Delmas' ODR configuration and clear, highly resolved

fluorescence signatures identified hotspots. Images taken through Plexiglass of a plutonium pelletizing press proved that the ODR technique is useful in scenarios where breaching containment for routine surveys can be hazardous. As long as there is a clear optical path for the UV photons to reach the camera system, ODR has been shown to be a viable hot-spot detection method. Finally, the group showed that decontamination agents such as tributyl phosphate (TBP) can shield alpha radiation enough to hide its fluorescence signal. This is an important consideration in any ODR application, the radiation must have open access to the air and not be shielded by coatings or containers. More recently, researchers at the National Research Center: Kurchatov Institute have demonstrated the ability to use off-the-shelf coronal discharge cameras to image luminescence due to alpha radiation (Ivanov, Stephanov, Danilovich, & Potapov, 2017). Using a 10,000 second exposure, the researchers were able to detect signals above background of 50kBq alpha sources. However, the researchers did not state if these images were taken outside during the daytime, so it is unknown if the increase in background would have changed their results significantly. What is interesting about these cameras is their ability to detect light in the solar-blind region of the spectrum (wavelengths less than 290 nm) during daytime operation (Lindner & Elstein, Daylight Corona Discharge Imager, 1999). Heavy light filtering for all light above 290 nm gives these cameras this ability. Apparently, these cameras use a solar-blind filter with a passband centered about 260 nm and a FWHM of ± 20 nm with a peak transmission of about 21% but the exact specifications and manufacturer do not seem to have been published probably due to proprietary information concerns (Lindner & Elstein, 1998).

Further work is needed in identifying this filter so it can be tested with the ODR configuration.

Johan Sand from the Tampere University of Technology has published several articles in the past few years on the detection of alpha radiation by the measurement of radioluminescence. Careful measurements of the nitrogen fluorescence yield, under indoor air conditions, were performed using a combination of optics attached to a PMT and a direct alpha particle detector (Sand & Ihantola, 2014). Sand showed that roughly 19 ± 3 photons per MeV of energy released were produced by alpha radiation. This data was a critical part of modeling efforts in the UK led by Thompson et. al. who showed that their method for modeling UV production due to ionizing radiation was in close correlation with the results published by Sand (Thompson, Barritt, & C., 2016)..

Sand followed up the yield measurements with a few publications on indoor measurements of alpha radioluminescence. The ODR technique was used to demonstrate the detection of MBq levels of alpha emitters in a glovebox (Sand, Ihantola, & Perajarvi, 2015). Sand evaluated the use of electron-multiplied and image intensified CCD camera technologies.

ODR has been shown to have potential in the medical physics area as well. Benjamin Fahimian at the Stanford University School of Medicine Department of Radiation Oncology has shown that ODR can be used to image, in real time, the dose from radiation beams used in the treatment of cancer (Fahimian & Ceballos, 2014). This approach may be useful for quality control measurements of treatment beams or real time incident

monitoring during treatment. Further work is needed to discover all the possible applications for ODR in the medical physics field.

Our Approach to ODR

The work conducted for this thesis was done as a progression of work carried out at Sandia National Laboratories between 2012 and 2015 summarized in a Sandia report. Harrison and Martin showed applicability of the ODR technique to outdoor measurements of high-intensity radiation fields at very long distances (Harrison, Martin, Wiemann, Choi, & Howell, 2015).

Po-210 sources were imaged outdoors at night using a telescope coupled to an electron-multiplied charged coupled device (EMCCD) camera at distances of up to 15 meters. Indoor measurements of intense gamma radiation fields were collected at the Sandia National Laboratories Gamma Irradiation Facility (GIF), a several thousand curie Co-60 source array. The measurements of these multi-million rad/hr fields led to some important considerations that were explored further in this work. Most notably, the deleterious effect of direct radiation strikes on the CCD was realized by the team, though significant precautions were made to minimize the dose to the chip. A major component of this thesis is to explore ways to mitigate this consequence to improve the overall ODR strategy for long exposures or exposures taken in higher than background fields.

The same GIF was used for a long-distance stand-off measurement of radiation through a port-hole at a distance of 75 meters using the same telescope system. The team was able to demonstrate the ODR technique for the detection of high gamma radiation fields well beyond the ability for conventional detection methods. The outdoor measurements

performed at Sandia demonstrated that background is the number one technical challenge to ODR. Much of the work performed for this thesis was aimed at lowering background through optical filtering, CCD cooling, and shielding. The research presented in this thesis was a progression of this previous work done at SNL and is described in the following chapters.

In chapter two of this work, a careful evaluation of our optical filters is made and a strategy for building filter combinations effective at reducing background as low as possible while maximizing transmission in the region of interest is described. Methods for evaluating the transmissivity of these filters are discussed. Results from filter optimization studies are presented that will help with future ODR configuration design considerations. Finally, transmission and out-of-band blocking data on Sandia's optimal filter combination is presented.

Chapter three presents a description of the image processing of ODR images that offers some suggestions to remedy common challenges encountered in our ODR experiments. Image conditioning techniques are discussed that improve the ability to convert raw ODR images into presentable data and provide qualitative results. Finally, a method for determining the contrast and signal-to-noise ratio (SNR) is proposed to help quantitatively evaluate image quality.

Chapter four describes an optimization study of camera settings that evaluates acquisition time, electronic binning, and chip temperature. A carefully controlled experiment was carried out using a Po-210 source, optical filters, a UV-transmissive lens, and a back-illuminated CCD camera with external liquid cooling. Strategies for automating data

collection were developed using the Andor Basic language which is a scripting language that can be used to control any Andor camera system. The results of this study are presented and will guide future decisions in analysis settings for various ODR applications.

Finally, in chapter five, this thesis concludes by presenting summaries of some real-world ODR measurements of various sources. A description of the challenges faced, and ways to avoid them in future measurements are presented. Also, a discussion of opportunities to improve the ODR technique is given. The thesis ends with some ideas for the application of ODR in the nuclear industry. The hopes of the researchers involved in this project are that this work can help lay the groundwork for a quantitative ODR method that can be used in any number of measurement scenarios.

II. OPTICAL FILTERING TECHNIQUES

Perhaps the most important component in the ODR system are the optical filtering devices. Several researchers have identified that background light is the number one challenge to overcome for an effective ODR configuration (Baschenko, 2004) (Lindner & Elstein, 1998) (Sand J. , et al., 2016). Since air is so sparse compared to solid scintillator materials, and the conversion of energy into photons is so inefficient in nitrogen, any amount of indoor or outdoor light can easily have an intensity several orders of magnitude above the light emitted in the radioluminescence of the air. While the challenge is great, there are methods to mitigate this background problem. First, the background light that can get in the way of ODR measurements must be characterized.

Sources of Optical Background

The cameras used for ODR in Sandia's laboratory are sensitive to light with wavelengths between 200 nm and 1000 nm which encompasses the UV, visible, and near IR regions of the electromagnetic spectrum. Any amount of ambient light reaching the CCD can completely overwhelm the sensor and make it impossible to see the faint nitrogen fluorescence signals. Heavy optical filtering is required to reduce this light as much as possible before reaching the camera's detector.

The sun emits light roughly in a continuum that spans the entire range of camera sensitivity. However, light from the sun is filtered by the ozone layer below about 280 nm which is often referred to as the "solar blind band" (Lindner & Elstein, 1999). The light from the sun in the region of the spectrum where the most intense nitrogen

fluorescence lines lie can be quite intense. Previous work done here at Sandia has shown that at the 360 nm band, sunlight increases nearly five orders of magnitude from that of night time (Harrison, Martin, Wiemann, Choi, & Howell, 2015). This forces outdoor ODR measurements to be done at night unless the nitrogen emissions within the solar blind band are being measured.

Perhaps more disrupting to most ODR applications, manmade light can also perturb the signal from nitrogen fluorescence. While most manmade light is constructed to specifically cut out the UV emission for public health reasons, the methods employed to do this are not totally effective (Elvidge, Keith, & Tuttle, 2010). Depending on the type of lighting, ODR measurements may need to be done in dark conditions if the UV emission is too great. In any case, the out-of-band region of the spectrum must be filtered as much as possible to correct for all manmade light, be it incandescent, fluorescent, or LED-based.

Filtering measurements based solely on wavelength may not be the only way to reduce background. The light from nitrogen fluorescence due to radiation interaction can be considered steady-state, or emitted at a constant rate from the source. Harrison et. al. described a method for temporally filtering image collection based on the sinusoidal nature of manmade electronic light due to the alternating current (Harrison, Martin, Wiemann, Choi, & Howell, 2015).. Their method relied on detecting the manmade light at a high framerate to determine the period of the fluctuation. A fitted curve to this pattern could potentially be used for the subtraction of light in an image with this pattern. While promising, the group showed that this type of analysis was not feasible for the

long-distance outdoor measurements they were performing at the time because of the low signal obtained from long distances to the manmade light. Furthermore, they found that averaging too many frames reduced the signal-to-noise ratio of the optical fluorescence signal.

This realization can possibly be leveraged to improve indoor ODR measurements where manmade light sources will be much closer to the detector. Temporal high-frame rate subtraction could be done when using an intensified CCD (iCCD) type camera using the techniques described by Harrison. Intensifiers built into intensified CCD (iCCD) cameras have very fast response that can be leveraged to temporally filter light in a different way. Consider a measurement scenario in which the intensifier, effectively acting like a very fast shutter for the camera, could be controlled by a gating signal that is queued to fire on when room lights are at a fraction of their most intense and switch off when the light builds up to that same fraction. This way the camera is only accepting light during periods of time when the room lights are their dimmest. The gating signal could be built from the fluctuations of the AC current in the light circuit. A consequence of this temporal gating would be the extension of acquisition time proportional to the duty cycle of the gate signal.

For any ODR application, the effective filtering of light reaching the sensor is a critical and necessary component of the detection configuration. Sunlight and manmade light can be several orders of magnitude above the signals produced in nitrogen fluorescence. With imaging cameras sensitive to the UV, visible, and near-infrared (NIR) regions of the spectrum, it is critical that out-of-band light be reduced as much as possible. A major

focus of the work done in this thesis was to evaluate methods for performing effective optical filtering for the ODR application.

Optical Filtering

Light can be filtered by physical means to specific wavelengths of the electromagnetic spectrum. There are two ways to filter light, through absorption or through interference. Filters are also characterized by what wavelengths are transmitted. Longpass filters transmit all light above a specified wavelength. Shortpass filters transmit light below a specified wavelength. Bandpass filters transmit light between two specified wavelengths. Absorption based filters include pigments, or chemicals that absorb light at a certain wavelength. The absorbed light stopped at the filter and the non-absorbed light passes through the filter. Interference filters are constructed by coating a transmissive glass with thin films of dielectric material at specified thicknesses that, when light passes through, cause interference in the light waves (Hecht, 2002). Reflections at each interface either selectively reflect some wavelengths or transmit others through the glass substrate. (Reichman, 1998) The thickness of the layers determines the properties of the filter. The thickness of the layers is on the order of one quarter the wavelength of light (tens to hundreds of nanometers).

State of the art sputtering technology has recently been improved to produce highly reliable, very thin dielectric coatings on optical components. Specific wavelengths, to a high precision, can be specified and very high transmissivity can be achieved by using this technique. This is a very advantageous development for ODR in that filters can be designed to only pass light at the specific wavelength of interest. Sandia has outfitted an

optical radiation detection lab with several unique, custom designed optical filters (Table 2). These filters were carefully evaluated in the lab to ensure the filter vendor specifications were accurate. Data from these evaluations were used to determine optimized filter stacks that would be the most useful for the ODR application.

Determination of Transmissivity

Optical filters purchased from vendors come with specification sheets that show the results of quality control measurements performed on the filters. This data is often geared toward the intended application of the filter (namely chemical fluoroscopy) and leaves out important information relevant to the ODR application. Thus, it was important to develop a procedure for determining the overall transmissivity of the filter across the entire spectrum that our cameras are sensitive to. Through the use of the optical bench, off-axis parabolic collimators, fiber optics, and a spectrometer, the whole transmissivity curve of the filters was obtained. This section describes the methods used to obtain these curves and what we learned in analyzing our filters.

The transmissivity of a filter can be described as the fraction of light that passes unblocked through the filter. Using a reference lamp, the % transmission can be calculated using the expression below.

$$T_i = \frac{I_{f_i}}{I_{r_i}} * 100\% \quad \text{Eq.1}$$

Where:

T_i is the transmission percentage at wavelength, i

I_{f_i} is the intensity of light measured through the filter in units of counts per second

I_{r_i} is the intensity of the unfiltered light from the same reference source in units of counts per second

Taking measurements of I_{f_i} and I_{r_i} requires the use of a reference lamp that emits light in the wavelengths of interest, a clear optical path through the filter, a spectrometer with a grating for wavelength selection, and a detector sensitive to the wavelengths of interest. Through trial and error, given the apparatus available in the lab, development of a standard method for taking these measurements was developed.

Light collimation and fiber coupling proved to be very important to this measurement. Early measurements were performed using lens-based optical-fiber couplers. We learned that the shift in collection wavelength with the lenses, while small, did skew the results appreciably. Also, the lens-based couplers did not allow for the light to be uni-directional when passing through the filter. Off-normal light causes a shift in the transmissivity curve as will be discussed later. To overcome these challenges, off-axis parabolic collimators were used.

The off-axis parabolic collimator allows multi-directional light to be collimated to a beam that is much more unidirectional. This proved to be very important when coupling to fiber optics which, through internal reflection, emit light in many directions at the end. The collimated or unidirectional light is then passed through the filter at normal incidence which allows for the true transmissivity curve to be evaluated. Beyond the filter, a second off-axis parabolic collimator is used to couple the light back to a fiber optic to send the signal to the fiber-coupled spectrometer.

Another lesson learned is that the optical distance for the filter measurement and the reference source must be identical such that any losses due to the measurement process are accounted for. Measurable differences in transmissivity were observed with optical paths of different lengths were used between the filter measurement and the reference lamp measurement indicating imperfect collimation. These differences are minimized if the same space is used between the source and detector collimators for blank, lamp, and sample spectra. A tube between the collimators was used for all the measurements, ensuring that the distance between the mirrors were the same between blank, lamp, and filter measurements. The optimized setup is described in figure 2.

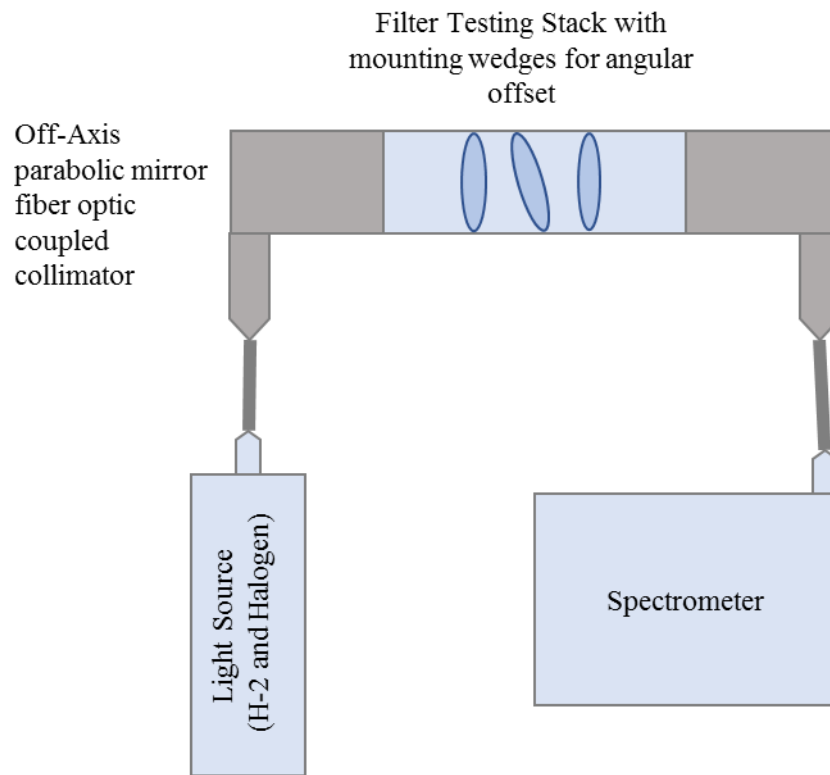


Figure 2: Filter transmission testing apparatus

Using this apparatus, a simple procedure for measuring transmissivity was developed.

1. Power on spectrometer, calibration lamp, and reference lamp. Wait 10-15 minutes for everything to come to temperature and for electronics to stabilize.
2. Use UV transmissive fiber optics for this application, many standard fiber optics will attenuate UV signals. Couple the fibers to the calibration lamp, the input off-axis parabolic collimator, the output mirror, and the spectrometer. If using linear fiber bundles, which is recommended to maximize signal, be sure to align the axis of the bundle with the slit on the spectrometer coupler. Having a misalignment here can reduce your signal by several times.
3. With the lamp sufficiently warmed, measure the calibration lamp such that the calibration lines in the region of interest (UV) show up with sufficient magnitude. Take care to not saturate the spectrometer, this can skew the results. A mercury/argon lamp works well for this purpose. Find the centroid of the relevant peaks, ensure that the spectrometer is calibrated well for wavelength. The peak centroid should not be more than a bandwidth or two (~ 0.5 nm for our spectrometer) of the reference wavelength. Adjust the wavelength calibration if necessary.
4. Couple the source fiber to the reference lamp (Deuterium and W-Halogen works well). Close the shutter to the reference lamp. Take the spectrum to obtain the dark noise signal (N_i). Note that this signal should not change with acquisition time, it is the readout noise for any single chip readout and is not a function of acquisition time.

5. Open the shutter of the lamp, acquire the lamp spectrum (L_i), with an acquisition time (t_L) such that the most intense region is near but does not exceed the saturation point of the spectrometer.
6. Remove the tube between the mirrors and mount the filter(s) you wish to test taking special care to orient the filters correctly according to the manufacturer certificate. The correct orientation should yield higher transmission than the incorrect orientation for most filters. Acquire the filter spectrum (S_i) with an acquisition time (t_S) such that the peak channel comes close to saturation but does not exceed it.
7. Between filter measurements, take another reference lamp spectrum. The lamp spectrum intensity may change between measurements. Use the lamp spectrum taken closes to the time the sample spectrum was taken in the calculation of transmission.
8. Export the spectral data and calculate the transmission curve using Eq. 2

$$T_i = \frac{t_L(S_i - N_i)}{t_S L_i} * 100\% \quad \text{Eq. 2}$$

Where, as mentioned:

T_i is the transmission percentage at wavelength, i

t_L is the acquisition time of the raw lamp spectrum

S_i is the count rate of the filtered spectrum at wavelength, i

N_i is the count rate of the dark noise spectrum at wavelength, i

t_s is the acquisition time of the filtered light spectrum

L_i is the count rate of the raw lamp spectrum at wavelength, i

The peak transmissivity of the filters that are most relevant to the ODR application are shown in table 2. The transmission curves themselves can be seen in appendix C. The transmission curves revealed that the band pass filters failed to block all light above 750nm. Therefore, an optimized filter stack must have a preconditioning filter in front to block this high-wavelength light. A short pass filter manufactured by Chroma Technology (Chroma Technology, 2018) with a cutoff at 650 nm (SP650) proved to be a very good preconditioning filter. This filter shows transmission in the passband of greater than 95% and an optical blocking fraction $\left(\frac{S_i}{L_i}\right)$ of 10^{-6} , or Optical Density (OD) 6, for wavelengths in the rejection band. Every optimized filter stack utilized this preconditioning filter in the front of the stack.

Table 2: Optical Filters at Sandia for the ODR application

Filter Name	Pass Bands	Notes	Peak Transmission (%)
SP650	<650nm	Very large off-band blocking fraction (Blocks OD6 675nm - 1070nm)	> 95% in ROI
ET360BP10	360nm +/- 10nm	Custom, first most abundant line	88%
ET360BP5.5	360nm +/- 5.5nm	Custom, Purchased after ET360BP10 proved to be effective, narrower band for reduced background	90%
ET340BP10	340nm +/- 10nm	Custom, 2nd most abundant line	95%
CT338-360DB	340nm +/- 9nm	Custom dual bandpass filter purchased to maximize signal for ODR	78%
	360nm +/- 9nm		93%

Determination Out-of-Band Blocking Fraction

The purpose of optical filtering, as it applies to ODR, is to remove as much manmade and natural background light from the light reaching the detector as possible. Since many of the imaging systems used in ODR are sensitive to light from near UV to far infrared, the whole spectrum must be blocked as much as possible. Many of the filters used in Sandia's ODR configurations were initially designed as fluoroscopy filters. In fluoroscopy the light source is carefully controlled and higher wavelength light is not present in the system. Thus, the specified out-of-band blocking fractions from the filter specification sheets often do not include the entire spectrum. Upon measurement of the whole spectrum transmission, light leakage in the higher wavelengths was apparent. To

mitigate this, we built stacks of many different filters so that the entire spectrum could be blocked as much as possible.

By combining several filters with different specifications, we found that we could optimize our signal while decreasing the background a great deal. Naturally, adding more filters in the optical path added to the drop in peak transmissivity. This drop is mitigated by choosing filters that block the regions of the spectrum that were not desired and pass the region of the spectrum that was desired with a high transmissivity. In this way, filters were arranged such that each subsequent filter narrowed in on the specific lines to be studied in the ODR configuration. The composite transmissivity can be estimated by the multiplication of the two individual transmissivities. Several factors may reduce this transmissivity and will be discussed later. Therefore, this should only be used as an estimate and filter stacks should be measured to determine the true composite transmissivity.

Sand et. al. has shown that stacking identical filters improved the overall off-band blocking fraction (Sand J. , et al., 2016). This concept was applied to a set of filters in our lab and we were able to confirm this effect. Using the transmissivity determination apparatus, we adjusted the collection time such that the spectrometer was saturated in the region of the spectrum with the passband. This allowed enough collection time to observe the bleed through in the out-of-band region of the spectrum. It is never a good idea to saturate a spectrometer, so the off-band blocking fraction was not quantified by this method. The effect was evaluated qualitatively.

The single filter stack showed some leakage in the visible wavelengths but this was reduced by adding a second filter. Bands that showed significant leakage with the single filter were smoothed out into the continuum of the spectrum when the second filter was placed in the stack. Given the sensitivity of equipment in the laboratory, we were not able to satisfactorily quantify the improvement in the out-of-band blocking fraction but we did confirm that the improvement was realized. Figure 3 shows the leaking bands of the single filter stack and how they are further reduced by adding a second filter in series.

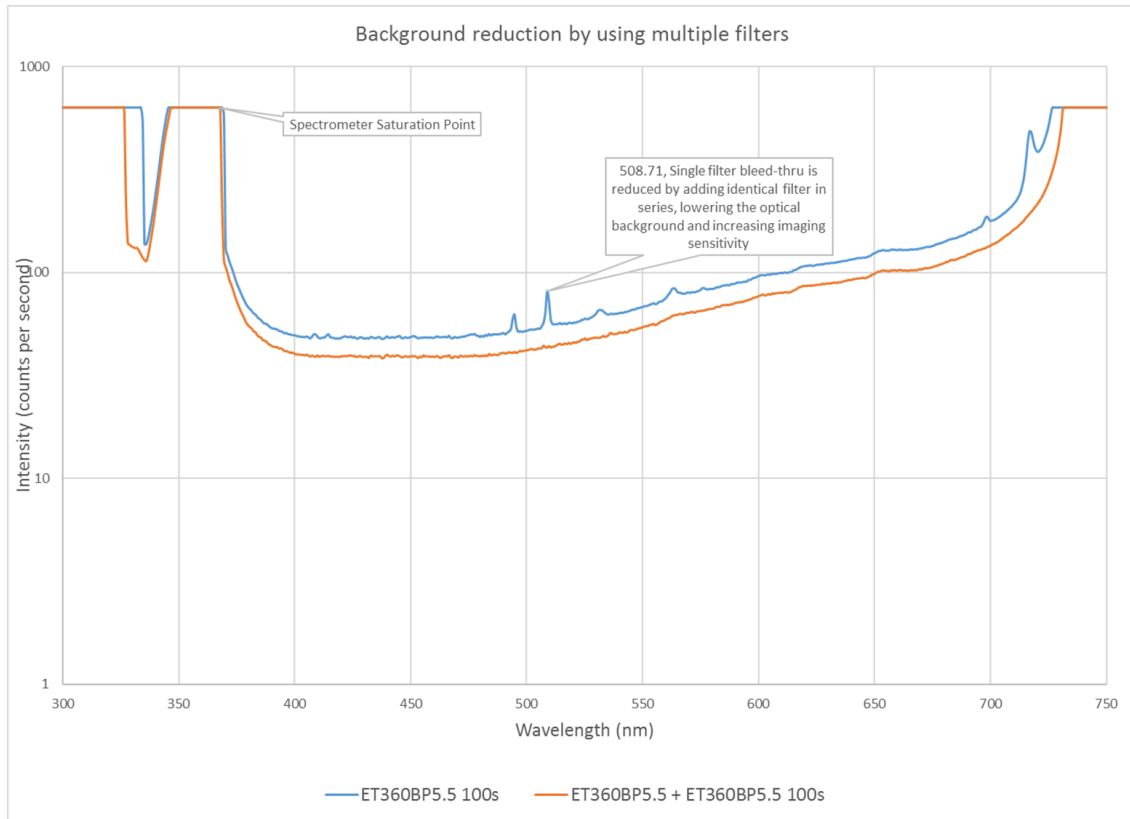


Figure 3: Transmissivity curve of a single and double-filter stack. These filters pass 360 nm with a FWHM of 5.5 nm. Out-of-band blocking is improved by using a second identical filter.

Originally, filters were stacked as close together as possible in assemblies to reduce the losses between filters through scattering off the walls of the tube. We discovered that these interference-based filters, when stacked parallel to one another can form a mirror

cavity in which light is reflected many times and trapped in between the two reflective surfaces. In optics, this is often referred to as a Fabry-Perot etalon which is the basis of an interferometer and lead to the development of the laser (Hecht, 2002). In this application, the etalon can cause the rejected light from the second filter to be passed in between the cavity several times, each time leaking more unwanted light through the second filter. Figure 4 describes this effect visually.

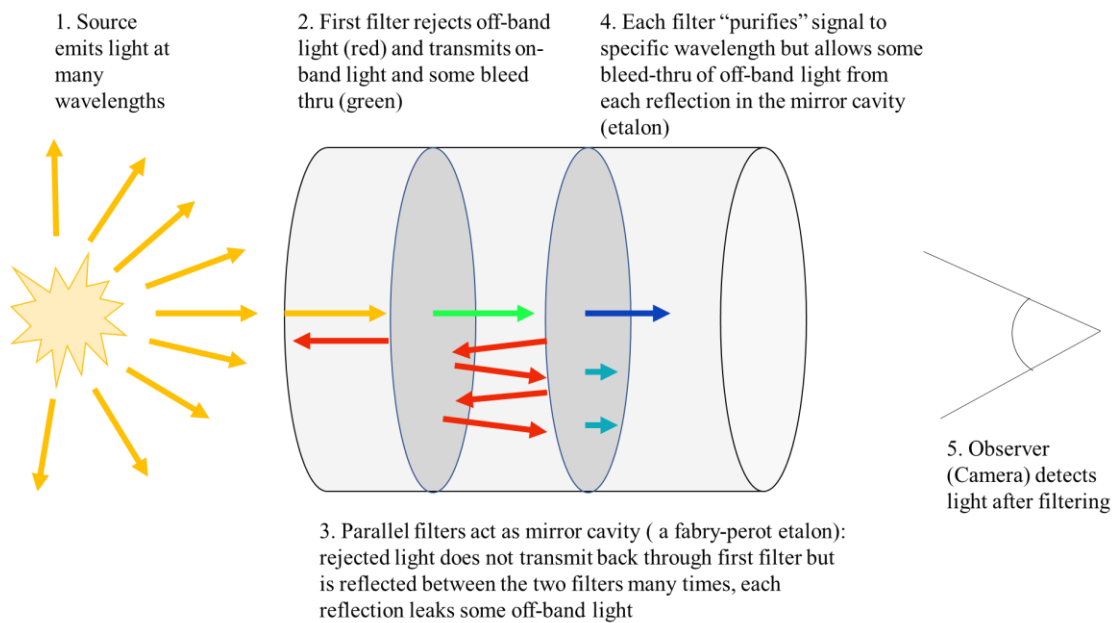


Figure 4: Parallel filter stack diagram. Two reflective filters placed parallel to one-another can form a Fabry-Perot etalon and lead to unsatisfactory results in the ODR configuration

By placing the subsequent filters at slightly off-normal angles from one another, the effect of this etalon is greatly reduced. This is primarily due to the fact that the reject light from the second filter cannot continuously reflect back and forth between the reflective surfaces, the rays eventually hit the wall of the filter housing and are absorbed.

Figure 5 shows how stacking filters in this way can improve the signal for the purpose of ODR.

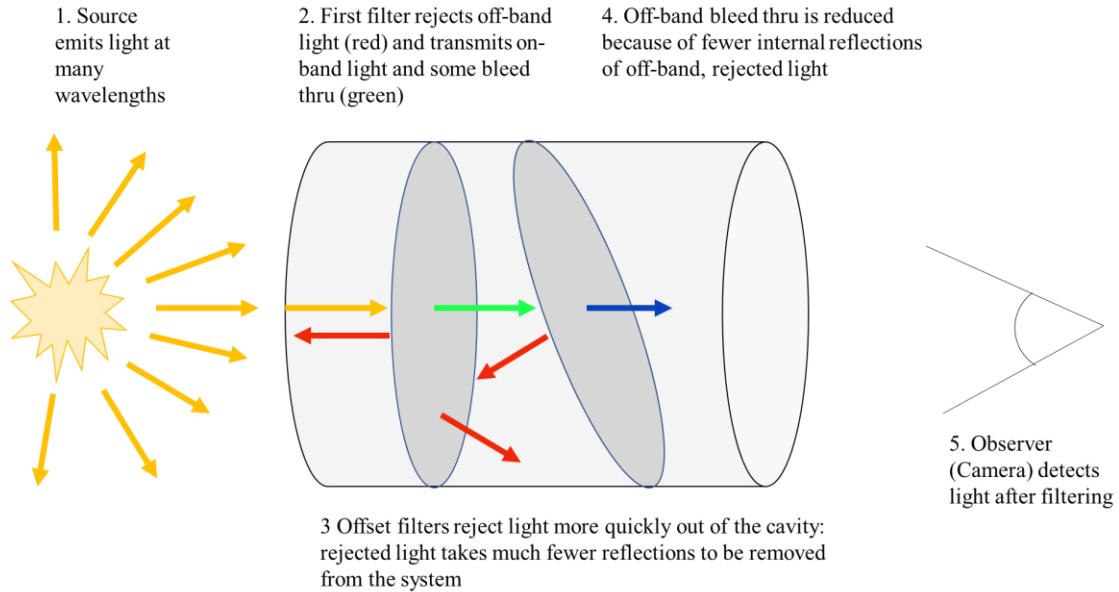


Figure 5: Off-parallel filter stack diagram. The Fabry-Perot etalon is removed by placing subsequent filters off-normal to one another which improves the signal for the ODR application

An attempt was made in the laboratory to qualitatively demonstrate the improvement to the blocking fraction by setting filters off-parallel. Measurements of two multi-filter stacks were made using the apparatus described in figure 2. The first stack contained two ET360BP5.5 filters stacked parallel with an SP650 filter in front. The next stack was built with the same two filters but with the second filter off-parallel by 3° using wedge prism mounting shims (Thorlabs part: SM1M353). First the peak transmission was measured using the methods described in the previous section. Second, an attempt was made to quantify the out-of-band blocking fraction of the configurations by taking the

spectrometer past saturation in the passband and looking at the light passing through at several orders of magnitude less than the passband.

No noticeable difference between the parallel and 3° offset stacks were observed. It could be that 3° was not a significant enough offset to reduce the etalon effects or that the filter substrate acts as a separator between the filters and provides enough of an offset to make the etalon inadequate. Another consideration is that taking the spectrometer to saturation in the channels encompassing the filters' passband could have unknown detrimental effects on the measurement. Further work is needed to attempt to show the difference in parallel and off-parallel filter stacking.

Effect of angle on transmissivity

Interference-based filters (and mirror coatings) are designed for light normal to the surface the thin film is placed on. This is because the material thickness itself determines how the light is changed. When off-normal light strikes the coating it effectively passes through more material, changing the properties of the transmission specifications the filter was designed to. In general, the passband of a filter shifts to lower wavelengths as the angle of incidence increases from normal (Lissberger & Wilcock, 1959).

Figure 6 below demonstrates this effect. When light strikes the filter off-normal, it must travel through more material to reach the glass substrate interface. The shift in light is proportional to the change in thickness of the film it must pass through.

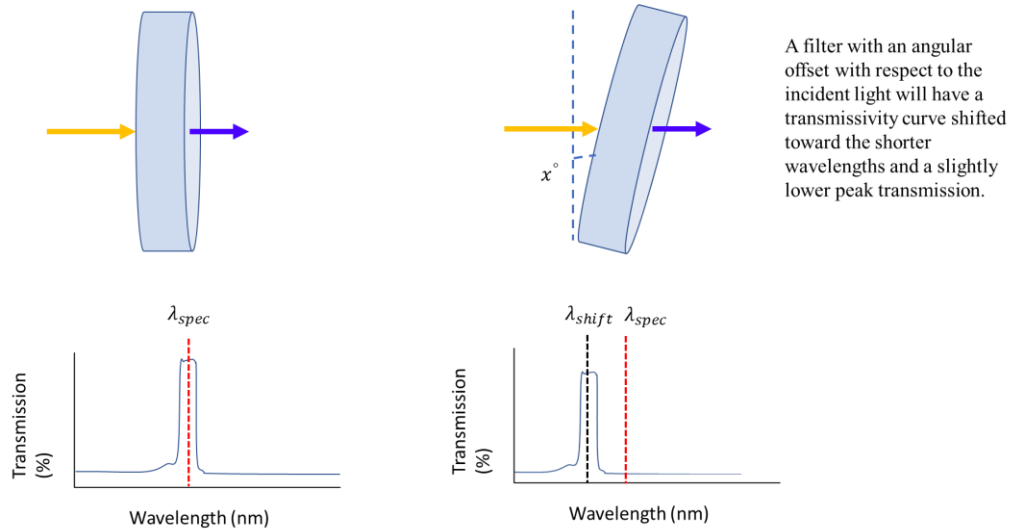
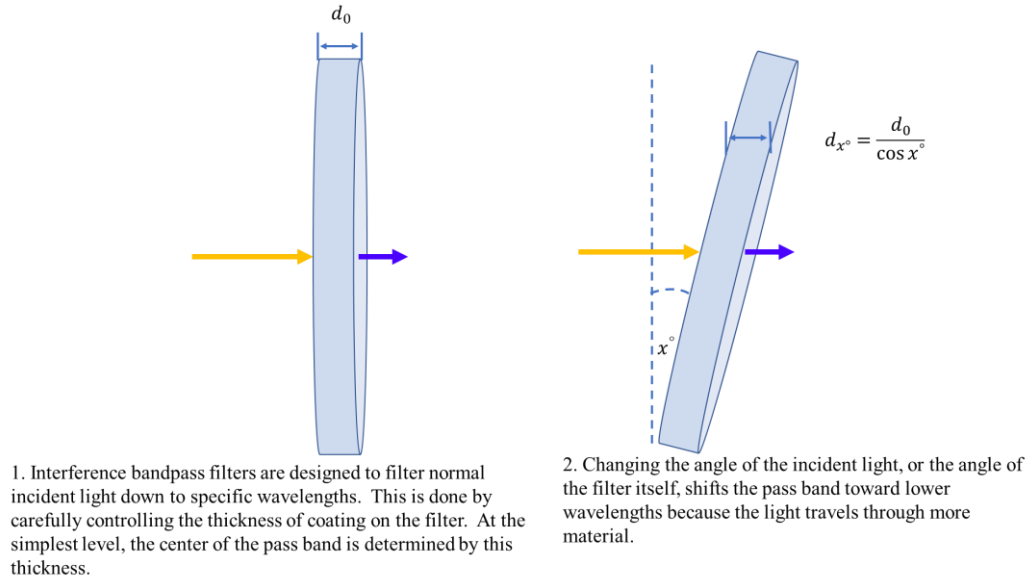


Figure 6: Effect of off-parallel filter stacking. Passband wavelength is shifted to smaller values for off-normal light

An experiment was carried out to determine the magnitude of the shift as a function of angle as well as the critical angle for which the line of interest is no longer transmitted by the filter. With an apparatus like that of figure 7, a single filter was placed in the

collimated beam of light from the lamp and rotated on a stand before the light was collected on the other side and sent to the spectrometer for analysis.

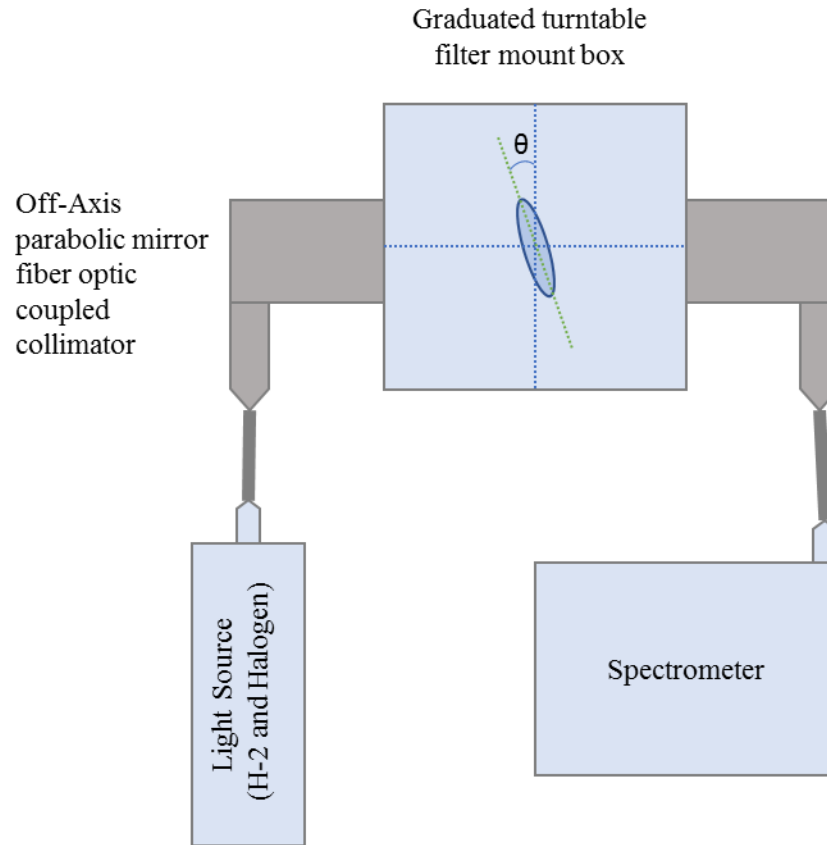


Figure 7: Modified apparatus to determine the effect of off-angle light on transmissivity

The ET358BP5.5 filter was used in this experiment as it had the narrowest passband of all of our filters in the lab. Initial readings of transmission were taken at 0° and then at every 3° until the filter was at an angle of 30° relative to the light. The table below shows the results from this experiment. For shallow angles up to 12° the decrease in transmission at the specified centerline are minimal, only a few percent. Beyond that, the transmission steadily drops until the line of interest is completely outside of the passband at an angle between 21° and 24° (see figure 8 and table 3).

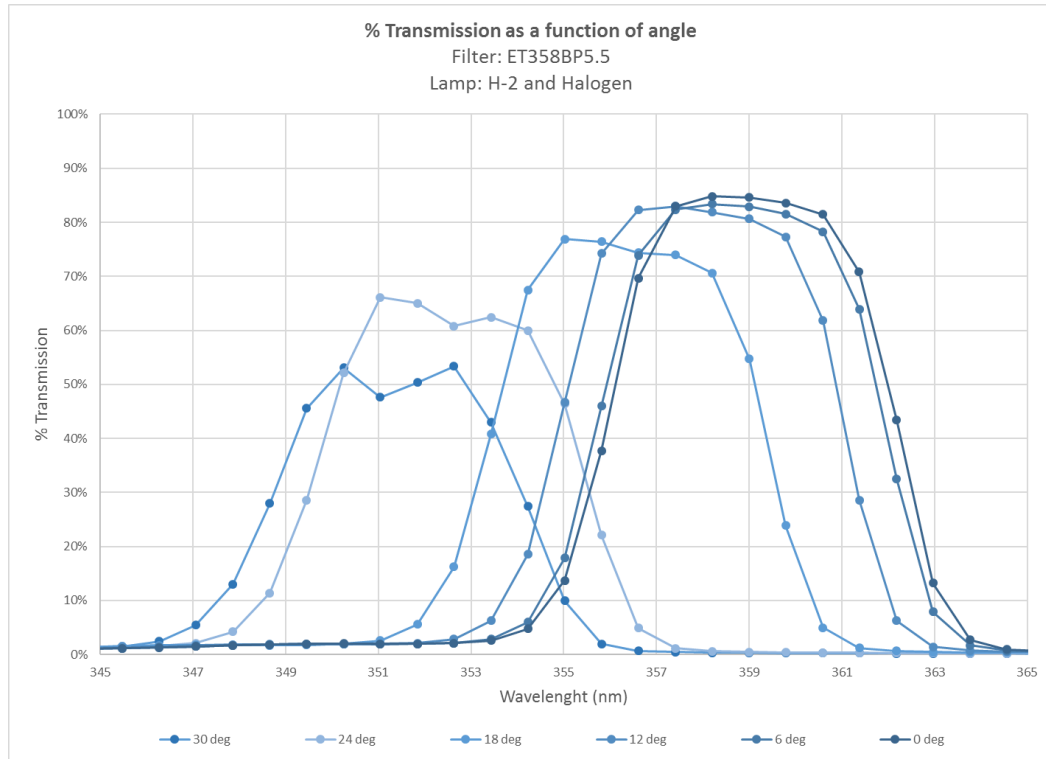


Figure 8: Transmission band as a function of angle for the off-axis light experiment

Table 3: Results from the off-axis light experiment

Filter Angle (Degrees)	Passband Centroid (nm)	Peak Transmission (%)	Transmission at 358 nm (%)
0	359	85%	85%
3	359	84%	84%
6	359	83%	83%
9	358.6	82%	82%
12	358.2	83%	82%
15	357.4	79%	77%
18	356.6	77%	71%
21	355.5	74%	41%
24	352.69	66%	1%
27	352.6	60%	1%
30	351	53%	0%

Another interesting observation is that not only does the passband shift toward shorter wavelengths, but the peak transmission of the passband decreases as well. This is because the effective thickness of film that the light is experiencing is greater which attenuates the light more. If the passband centroid is charted it fits nicely to a cosine curve as expected. Figure 9 shows this correlation agrees well with the data.

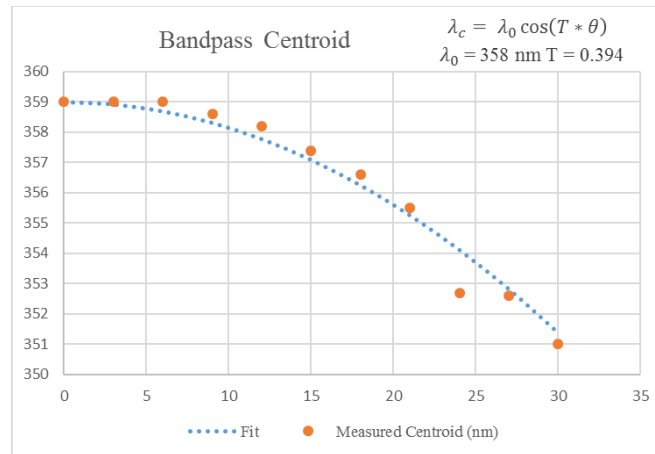


Figure 9: Passband centroid as a function of filter angle. Passband centroid fits well to a cosine function as expected

The 24-degree reading appears to be an outlier. This could be due to imprecise placement on the turntable box, a change in lamp performance, or a change in the fiber coupling. For quality control purposes, the filter was turned in the counter clockwise direction at the same gradations. All of the measurements in the clockwise direction agreed well with the counterclockwise measurements except for the 24-degree measurement.

Outlier notwithstanding, these results proved to be important in future optical designs.

Off-axis light can be a problem with close-up imaging in lens-based systems or standoff detection with telescope optics. This data helped drive the decision of how best to place

the filters in the demonstrator telescope. Light collected from the telescope was sent to the camera with several mirrors and lenses. The filters were placed such that the off-normal light incident on the filters were minimized. This ensured a consistent transmission of all the light in the image.

Summary of Optical Filtering Optimization

Overall, several important lessons were learned in our extensive testing of the optical filters.

1. Having a consistent rig to test filters against manufacturer specifications is very important. Specification sheets will often not mention out-of-band pass through as it is often ignored for the intended application of the off-the-shelf filter. Off-axis parabolic collimator fiber couplers are essential to the transmittance apparatus.
2. Stacking identical filters in series improves the out-of-band blocking while reducing the overall transmittance by a small amount if the individual transmittance of the filters is large. This method is not recommended for filters with a peak transmittance below 80% as the compound effect will provide a greatly reduced transmittance. While the overall transmittance can be estimated by the multiplication of the individual transmittances, the stack should be independently measured to confirm as scattering within the stack can unpredictably reduce the overall transmittance.

3. Off-axis light is transmitted with a passband that is shifted to the shorter wavelengths. Light with an angle of incidence greater than 20° may fall within the passband at all for the narrow type filters used in the ODR application. Optics should be designed to minimize the angle of incidence if possible.
4. When testing identical filters at different off-parallel angles we noticed an interesting “sharpening” effect on the passband. Because the second filter is shifted to lower wavelengths it essentially reduces the composite passband to a narrower range. This is illustrated in figure 10. When attempting to narrow the passband of a set of filters, this has proven to be an effective method. However, care should be taken as to not reduce the overall transmittance to an unacceptable level.

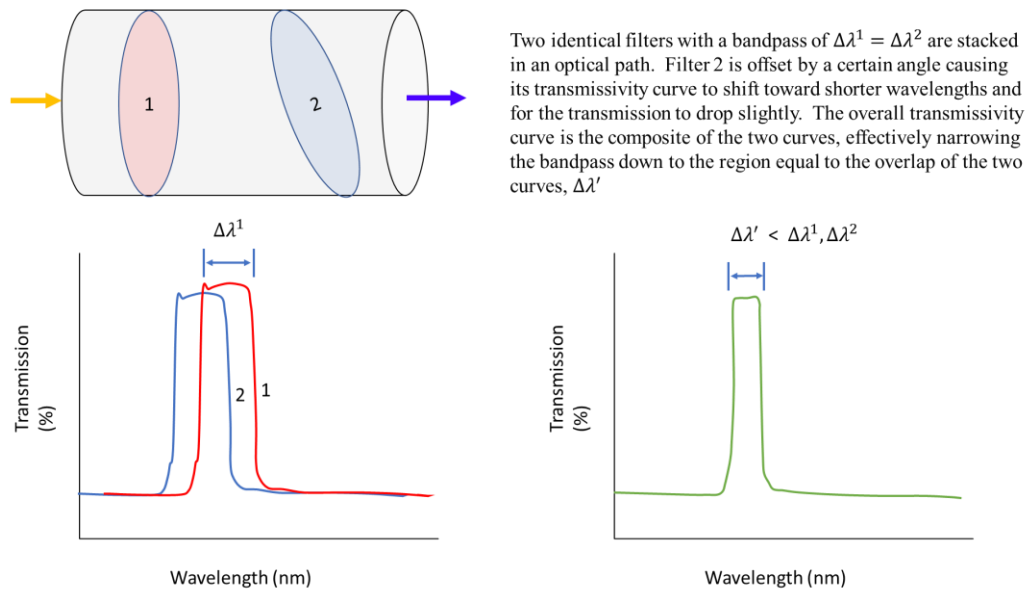


Figure 10: Passband sharpening effect. Filter passband is sharpened by offsetting identical filters

5. Combining filters with desirable and complimentary properties can be stacked for improved results that greatly improve the quality and capability of ODR

measurements. Optimized stacks were created for our ODR configurations and the peak transmission and overall spectral performance were measured with our spectrometer apparatus. The results are summarized in table 4. The full transmission curves are pictured in appendix C.

Table 4: Optimized filter stacks constructed at Sandia for the ODR application

Stack	Filters	Pass Bands	Peak Transmission (%)
1	SP650 ET340BP10 ET340BP10	340nm +/- 10nm	76%
3	SP650 ET360BP5.5 ET360BP5.5	360nm +/- 5.5nm	81%
4	SP650 CT338-360DB CT338-360DB	340nm +/- 9nm 360nm +/- 9nm	75% 88%

III. IMAGE PROCESSING

Low light imaging presents many challenges that can be overcome by careful image processing post-acquisition. Long acquisitions of very dark scenes lend themselves to noisy images that are often difficult to interpret with the naked eye. Through image processing, seemingly hidden sources can be revealed. This qualitative approach is important to using this technology to locate the dose in air in real time. After conditioning, quantitative calculations can be made of the images to determine the contrast and the signal-to-noise ratio.

Mathematical binning is similar to electronic binning with the exception that the full resolution image is processed through an algorithm that sums neighbor pixels into super pixels artificially. This can improve the perception of contrast and sensitivity but has the detrimental effect of increasing the image noise in low background images as the readout noise is compounded with each additional pixel. Because of this, mathematical binning does not have much use in most ODR applications. Electronic binning described previously is much more beneficial to image sensitivity when some spatial resolution can be spared for improvements to SNR and contrast.

Post image contrast enhancements, while not able to enhance the true contrast, are able to bring signal out in an image so that the human eye can perceive the difference. Simple contrast enhancement involves taking all the pixels in an image and rescaling the pure white and pure black pixel values such that they represent a small percentage (<1%) of the pixel intensity range. For most of our measurements, scaling contrast to below 1%

(in most cases 0.4%) worked very well. This processing does not change the numerical pixel values whatsoever, it simply adjusts the way the computer presents the image.

Post image mathematical filtering is very important to processing ODR data. While there are several dozen types of filters that can be used in most image processing software, the most useful filter we found was the median filter. The median filter will reduce the speckle in an image due to direct radiation strikes on the sensor (henceforth referred to as hot pixels) in an image by reducing their value to match their neighbor pixels. This type of filter will blur images, but because the low-level signals being observed with ODR generally do not produce sharp images, this blurring is usually acceptable. A pixel radius of 1-2 pixels proved to be a good setting for most images. Many of the outlier pixels are smeared away while much of the spatial sharpness is still maintained.

Perhaps a more effective image filter that was used involved taking several shorter acquisitions in time, then summing them up to form a composite image, all while altering the outlier pixels. This can be done in ODR applications where there is no movement of the camera or scene and when source strength is not appreciably changing during the duration of the measurement. This approach has two benefits. The first of which is that for shorter acquisition times, as discussed previously, the chance for direct chip strikes on the CCD is reduced, leading to fewer hot pixels. The second benefit is that while summing pixels a temporal image filter can be applied in which the frame-to-frame pixel values are compared to each other to detect outliers. Should an outlier be detected, it is removed from the total, taking on the median value of all the pixels in the series.

For example, if five images are taken and the five pixel values are 5, 8, 6, 1, 30, the last pixel with a value of thirty is well above the median of the other pixels and can be reassigned the median value (in this case, 6). For sets where more than one pixel may be an outlier, this method can be applied iteratively until all pixels fall within a set statistical window of one another. This proved to be a very effective approach in reducing the hot-pixels in images with long exposures or when the camera was in a higher-than-background radiation field. This approach must be balanced with the need for individual pixel sensitivity because as the number of frames increases, so too does the compounded readout noise. Of course, for iCCD type imaging configurations, this approach does not suffer from the compounded readout noise.

After image filtering, background subtraction can take place to remove the dark pixel values from the image which will improve the relative signal intensity in weak images. A direct pixel-to-pixel subtraction can be done in situations where a source-free scene is available to take background measurements with the same acquisition settings as the sample image. When this is not the case, as will be experienced in an application of this technology, the background can be estimated by probing a region of the image where it is known there is no contribution from the nitrogen fluorescence. This representative dark region can then be subtracted from all the pixels in the image. This approach of course relies on knowledge of where the source is which is not always the case. Concentrated dose fields, such as those encountered with alpha radiation, naturally produce regions with high contrast. Therefore, background subtraction may not be necessary to successfully detect these types of sources. Background subtraction is an important

consideration when deciding how to photograph a scene. Knowledge of where the source is expected in the scene is very useful.

After background subtraction, the image can be run through a signal identification algorithm. This can be as simple as a statistical threshold approach where the displayed color of the pixels above a certain number of standard deviations are set to white while all others are set to black. Large regions of signal would then show up together as long as the signal is well enough above the background. Another approach involves Gaussian filtering and line detection algorithms to define the shape of the signal.

Finally, the processed image can be mapped to a false-color scale or “heatmap” and overlaid on a visible image of the scene. Once the visible image is processed, the raw signal can be analyzed mathematically to yield some quantitative data on the measurement. The contrast and signal-to-noise ratio are important quantitative parameters that can be used to compare images.

Contrast and Signal-to-noise Ratio (SNR)

The contrast is a simple measure of the difference in signal to the background that make it distinguishable. In ODR this is an important parameter in comparing two images. The larger the contrast, the more distinguishable the source is from the background within the field of view. The contrast is calculated simply by taking the absolute value of the difference between the signal and the background divided by the background. Equation 3 shows this relationship.

$$C = \frac{|S - \bar{N}|}{\bar{N}} \quad \text{Eq. 3}$$

where C is the contrast, S is the net signal and \bar{N} is the mean background value. Methods for determine S and \bar{N} can vary from application to application. In our experiments S is determined as the mean pixel value in the region of the image defined as the source. \bar{N} is defined as the average pixel value of a region in the image where it is known there is no source. It is important to ensure S and \bar{N} are free of statistical anomalies through filtering as many of our early results were skewed by these values and lost meaning when comparing images.

Another parameter used to quantify image quality is the signal-to-noise ratio. (See Eqn. 4) This is simply the signal divided by the standard deviation of the background. Once again, methods for determining S and $\bar{\sigma}_N$ can vary but in their simplest form S is the mean pixel value in the source region and $\bar{\sigma}_N$ is the standard deviation of the pixel values in the background region. This simplistic approach lends itself to skewing by the presence of pixels struck by ionizing radiation directly, i.e. hot pixels, and statistical anomalies. The image region chosen to determine signal and background clearly affects the contrast and signal-to-noise ratio. The signal-to-noise ratio is defined as

$$SNR = \frac{S}{\bar{\sigma}_N} \quad \text{Eq. 4}$$

where S is the signal and $\bar{\sigma}_N$ is the standard deviation of the background.

Lamadie proposed a delicate method for determining the signal-to-noise ratio (Lamadie & Delmas, 2005). The signal value was taken as the average net signal in the source region of the image. The noise was determined by subtracting the raw image from a smoothed version of the same image that had been processed through a gaussian filter.

This difference image was said to contain only the high frequency pixel variations sans the outliers. The standard deviation of the smoothed pixels within the dark region are then taken to be representative of the overall noise in the image. This approach seems promising and plans are in place to investigate this further in future image processing work.

A simple code written for the freeware ImageJ was composed to process images taken with the SNL ODR configuration (Fig. 11) (Rashband, 1997-2006). This algorithm was used to process the images in the acquisition optimization experiments discussed earlier. While no median image filtering was applied in this algorithm, it is wise to inject this step after contrast enhancement, and before any calculations are made. The code itself can be found in appendix B.

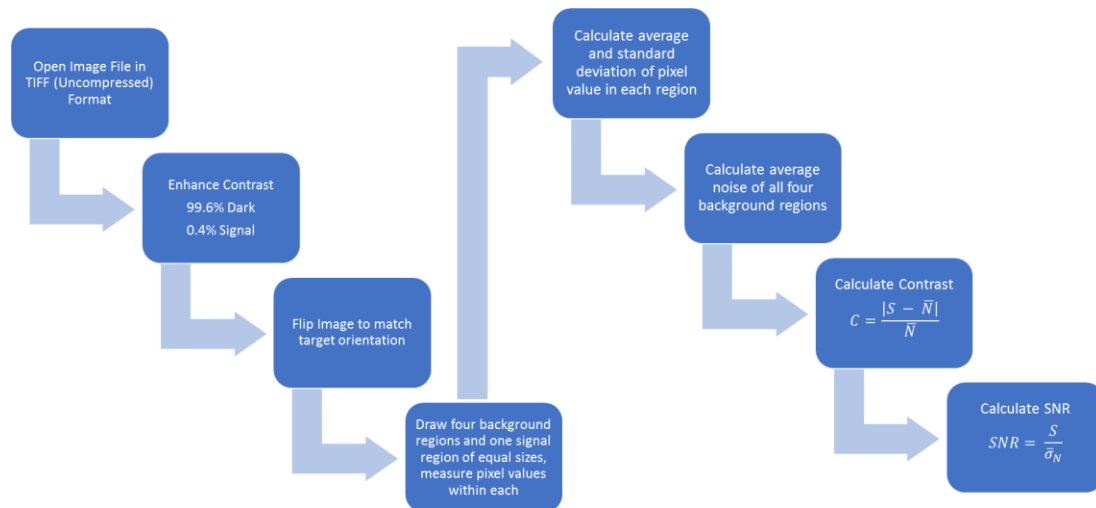


Figure 11: ImageJ image processing algorithm flowchart

The simplistic approach to the determination of contrast and SNR proved to be problematic in ODR due to the variation in pixel values caused by direct radiation strikes. Further work is needed to investigate methods for improving this important quantifiable metric.

IV. LIGHT DETECTION FOR IMAGING

Light Collection Techniques

Light collection is a very important component of the ODR system. It is the light collection that defines the depth-of-field and field-of-view of any complete imaging system. The collection optic must be able to focus on the target at the anticipated distance for the application. The depth-of-field must be deep enough to optimize the collection of all the fluorescence photons emitted from the dose cloud. The field-of-view must be wide enough to encompass the search area for a single image. It should be noted that small field-of-view limitations can be overcome by employing careful scanning of a scene with opto-mechanical components. This approach however, can increase the acquisition time a great deal which may not be feasible in some applications.

The optics can be refractive (lens-based), reflective (mirror-based) or a combination of the two. The optical surfaces and substrates for which the light is intended to travel through must be as transmissive in the bands of interest as possible. Lenses made of fused silica glass have been conservatively shown to be up to 99.5% transmissive in the region of the spectrum we are interested in (UQG Optics, 2018). Many off-the-shelf lenses may be made of fused silica but are in fact coated to block UV as this has a detrimental effect on traditional photography. It is important to know the transmittance of the lenses being used in ODR and, when possible, lenses designed to image UV should be used.

Sandia owns a special Nikon lens that is no longer manufactured. The Nikon UV-105 F/4.5 lens was made popular in the 1980s as a very useful lens for UV photography by

enthusiasts and forensic scientists. (Company Seven, 2018) This lens is constructed of fused silica and has a transmittance of $> 70\%$ in the band from 220 nm to 900 nm. The aperture is about 1 inch which limits the total light collection but aligns well with the 1-inch diameter optical filters traditionally used in fluorescence microscopy that have found a use in Sandia's ODR configurations. This lens was used in many of the experiments conducted as part of this thesis.

Other custom collection optics were acquired by Sandia for the purpose of ODR. Custom coated mirrors and lenses were designed and built for the purpose of building the demonstrator telescope (that will be described later). The coatings on the custom mirrors were specifically engineered to preferentially reflect light between 320 nm and 400 nm while allowing the rest of the spectrum to pass through thorough and be removed from the optical path. The reflectance at 340 and 360 nm for this coating was 99.8%. This approach to reflecting light can improve ODR sensitivity by pre-filtering the light reaching the filter stack. Paying careful attention to the collection optics design is a key factor in any ODR configuration. A single misplaced or mismatched component can completely hide the signal.

Charge Coupled Device (CCD) Cameras

The charge coupled device (CCD) is a semiconductor component that has the special property of being able to convert photons to measurable electronic signal. While CCDs can take many geometries, the 2-dimensional array is the most useful to imaging. A CCD array is composed of several pixels. Each pixel has a capacity to collect light and build charge up to a saturation point. The pixels are biased such that they can accept charge up

to 10^5 electrons per pixel. (Sze & Kwok, 2007) The magnitude of the charge is proportional to the flux of light it receives. Using CCDs is analogous to film in that the image is “burned” into the chip by the building up charge in the pixels. When the chip is read out by the camera electronics the raw data can be analyzed mathematically to produce a readable image.

The physics of CCDs and their associated electronics are beyond the scope of this thesis but several groundbreaking improvements to this technology have been realized in the past decade which make ODR even more applicable. The most notable improvement made to CCDs in the last decade is the ability to build back-illuminated sensors that increase the sensitivity to short-wavelength light (USA Patent No. 7521335, 2009).

These sensors are not as effective at detecting longer wavelengths in the near-infrared region due to their longer absorption depth. Unlike conventional CCDs, back-illuminated sensors are flipped and thinned so that the readout electronics do not get in the way of light reaching the sensor.

The quantum efficiency (QE) is defined as the efficiency in converting photons to stored electrons. A QE of 100% would mean that every single photon reaching the active area of the sensor will create a signal in a pixel. With back-illuminated, thinned sensors, QE of above 90% can be achieved which is a very significant improvement from the 60% that was achievable from the most sensitive conventional CCDs. QE drops off as wavelength shortens but special coatings can be applied to CCD chips to make them more sensitive to light in the UV (Princeton Instruments, 2012). QE of up to up to 70% in the deep UV can be achieved in modern scientific cameras (Andor Technology, 2008).

CCDs most applicable to ODR come in three configurations. The standard back-illuminated, deep-cooled, UV coated CCD chip is useful for most general applications. The intensified CCD (iCCD) uses an image intensifier in front of the CCD to amplify the light reaching the detector. An image intensifier is a photocathode, a multi-channel plate (MCP), and a phosphor screen in series to magnify the light being imaged. Light enters the photocathode producing photoelectrons. These photoelectrons are multiplied in the MCP and then reconverted to photons in the phosphor screen. The iCCD is used in low-light situations and is the principal component in night-vision goggles. The iCCD has the advantage of being able to be shuttered non-mechanically. By reducing the voltage between the MCP and the photocathode, electrons do not make it to the phosphor screen and subsequently no light reaches the CCD. Carefully controlling this voltage can manipulate the image intensifier like a shutter achieving gate windows as short as 200 picoseconds. In general, iCCDs are most useful when fast gating is needed for low light signal imaging.

The Electron-Multiplied CCD (EMCCD) uses a gain register between the shift register and output amplifier. These electronics magnify the electrons read from the CCD with gains up to several thousand. The EMCCD has the advantage of having nearly negligible readout noise and very low dark current when cooled to -90°C and below. EMCCDs are typically enclosed in high vacuum which improves cooling performance and sensor lifetime. In general, EMCCDs are more useful when long exposures are needed to capture signal in very low light environments, but are more challenging to use in high background situations.

Optimization of Acquisition Settings for the ODR Application

Standard Acquisition Settings for the ODR application

The cameras used in our ODR configurations have several customizable settings that can be optimized for various measurement scenarios. While available settings differ from camera to camera a few basic acquisition setting decisions must be made prior to any measurement. The acquisition mode is how images are captured during operation. The triggering setting specifies how the camera will be signaled to start and end acquisition. Readout mode is how the charges on the CCD will be read out into the signal processing circuits. Vertical pixel shift speed is the time it takes to shift charge from a row on the CCD chip to the next row of pixels. Readout rate is the speed at which individual pixel charge is measured from the chip.

Single scan is the simplest mode available on most cameras. The aperture shutter of the camera is open for a preset amount of time and charge is collected on the chip until the shutter closes. This acquisition mode is the most frequently used in our ODR systems because it yields images with the lowest read noise and allows the camera to take very long exposures. The available acquisition times are limited by the chip readout settings. The accumulate mode allows the camera to take several frames and add them in memory. In this mode the user specifies an exposure time, a cycle time, and the number of accumulations. This mode can improve the signal-to-noise ratio because the standard deviation of the accumulated pixel value will always be less than the individual standard deviation of a single measurement pixel value for equal exposure times. This approach is more useful when using iCCD than EMCCD sensors. iCCD sensors intensify the light incident on the sensor whereas EMCCD technology amplifies signal post-detection.

Running accumulate mode with EMCCD technology will intensify readout noise and signal which counteracts the gain in sensitivity from electron multiplication. (Andor Technology, 2008) Incident light from the intensifier in iCCD cameras greatly exceeds the readout noise so compounding it through accumulate mode will have little impact to the sensitivity (Andor Technology, 2012).

Kinetics mode allows the user to take several snapshots in a series and is typically used in observing the evolution of a fast-evolving system. This mode is not applicable to long exposure ODR measurements but may be useful in measuring pulsed radiation events. An even more rapid kinetics acquisition mode is Fast Kinetics which allows individual exposure times to be as low as microseconds. This mode is typically used when the camera is configured for use as a spectrometer.

Triggering is used to specify how measurements will begin and end. Triggering can happen internally by user entry in the camera control software, or externally by use of a triggering signal. The most commonly used triggering mode is internal when performing long exposures. For kinetic or fast measurements, an external signal that is synced in time with the triggering of an experiment can be used. This triggering mode could prove to be useful in applications involving pulsed radiation imaging.

Readout modes are set based on the application for which the camera is being used. In Image mode, the entire 2D map of the CCD chip is read out in individual pixels. This is the most common mode that is used in our ODR configurations. In full vertical binning mode, the charge from each column of pixels is added together to give a single charge per

column. This application is used when the camera is attached to a spectrograph where a certain tight range of wavelengths of light are aimed at a column of pixels.

Finally, Multi-track mode is used to build customized “superpixels” (summed from many pixels) on the CCD based on the pattern of light that is falling on the chip. This mode is useful when fiber optics are coupled to the camera. Customizable on-chip binning can be used to avoid read-noise penalties realized in post-process binning.

Vertical pixel shift speed can be adjusted for slight improvements to the charge capacity of the chip, but will increase the minimum exposure time achievable. The manufacturer typically recommends the fastest possible shift speed be used to reduce the clock induced charge noise (Andor, 2018). Clock induced charge (CIC) noise is the effect of spurious electrons being generated during readout that are amplified above the noise floor by the electron multiplication electronics. CIC noise leads to speckled images in the low-light, long exposure measurements taken in ODR. The more important setting is the pixel shift readout rate. This is the rate at which pixels can be read out from the shift register. This rate directly impacts the measurement sensitivity. In most of our ODR measurements with long exposure times, the lowest readout rate available is used such that the dark noise is minimized. This increases the amount of time for the acquisition but greatly improves the ability to observe faint signals. Some cameras are outfitted with a preamplifier that can be used to apply gain to the signal from the CCD chip. In general, a higher gain allows for sensitivity improvements but can also lead to saturating the sensor more quickly. Depending on the measurement scenario, care must be taken to not over saturate the sensitive CCD which could cause degradation in performance over time.

For cameras outfitted with an electron multiplying intensifier in front of the CCD, additional settings are available that can be chosen prior to acquisition. Most importantly are the gate mode and the electron multiplier gain. The gate mode can be set to trigger the intensifier on an external signal or keep the multiplier on during the acquisition. Most long-exposure type measurements will keep the gate open for the duration of the measurement. The electron multiplier gain increases the sensitivity but can lead to sensor “bleaching” if set too high for too many measurements. Sensor bleaching is over-saturation of the sensor leading to decreased pixel sensitivity and should be avoided by careful use of the gain settings on the electron multiplier.

Determining the best acquisition parameters for the ODR technique was a focus of this thesis research. In summary, most measurements were taken in single scan mode, with internal triggering and a readout mode of image. The vertical pixel shift speed is set as fast as the camera will allow, and the horizontal pixel shift as slow as possible.

Preamplifier gain is set to the highest settings in most low-signal scenarios but is adjusted to be lower when saturation is expected to occur. In addition to the settings discussed above, the CCD chip temperature, the electronic binning, and the acquisition time can be adjusted to suit the application of ODR. The following sections will discuss the results we obtained in evaluating electronic binning settings, CCD chip temperature, and acquisition time.

Laboratory Setup for Acquisition Optimization

Laboratory experiments were conducted in a controlled setting to optimize camera settings for the ODR application. The camera system including lens, filter, and mounting hardware were placed in an optically tight dark box attached to an optical bench. The

optics were focused to a small area on the other side of the box where a target was placed and a pedestal directly in front of the bullseye. On top of the pedestal a Po-210 source with a strength of approximately 200 uCi was placed. The camera was cooled via a liquid heat exchanger so that the lowest possible temperatures could be realized while maintaining a closed box.

The camera used was the Andor Technology iKON-M 934 Series with the BU2 CCD sensor (Andor Technology, 2008). The BU2 sensor is back-illuminated and coated for optimal performance in the UV region of the spectrum but it is not an EMCCD. A camera's sensitivity to light as a function of wavelength is referred to as the quantum efficiency (QE). This is a measure of how well a CCD can convert incident photons to measurable electronic signal. Figure 12 below is the quantum efficiency curve for the Andor iKON-M 934 camera. Note that the BU2 sensor has QE between 55% and 65% in the region of 250 nm to 400 nm. Compared to other sensors available on the market, this QE is quite large. The camera was cooled with a chilled propylene glycol re-circulator so that CCD chip temperatures down to -100 °C could be achieved.

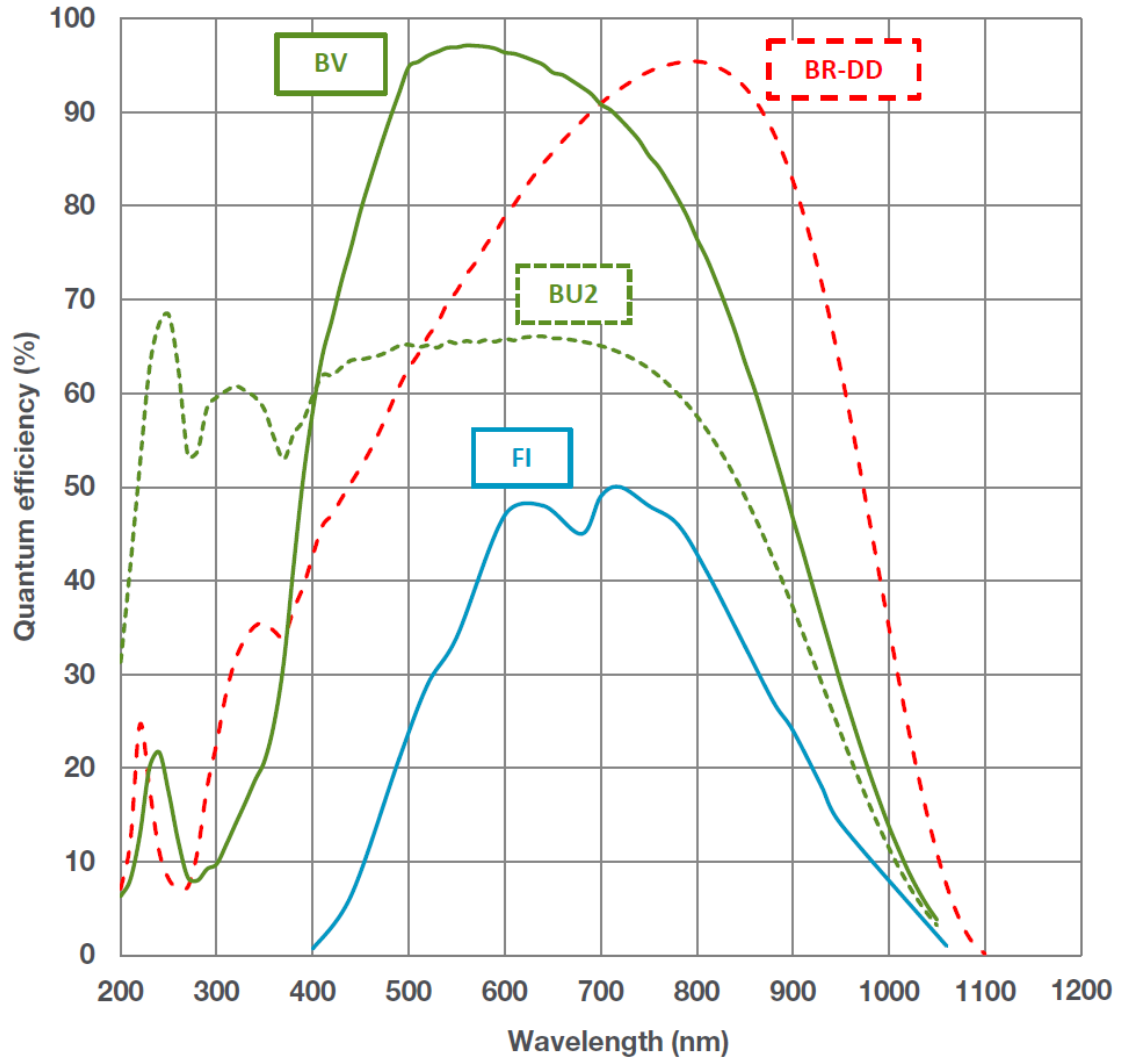


Figure 12: Quantum Efficiency (QE) curves for the Andor iKon-M 934 Series camera. (Andor Technology, 2008)

Attached to the front of the camera was a Nikon UV-105, 105mm f/4.5 Multispectral Imaging lens. This lens, specifically engineered for UV imaging, has a superior transmission in the UV and little to no distortion. The minimum distance that focus can be achieved is 18.8 inches (Nikon, 1984). The focus of visible light is directly coincident with the UV focus so there is no need for focus shifts from imaging visible light to UV.

Consequently, this makes alignment and focusing very easy in the ODR application. Visible light can be used to focus optics instead of expensive UV LEDs. The optics in this lens are made of high quality fused silica which has been shown to have nearly 100% transmission at the wavelengths of interest to ODR (UQG Optics, 2018).

In front of the Nikon lens were two 25 mm identical custom optical filters designed to pass 340 nm with a full-width at half maximum of 10 nm. This filter, while specifically engineered to pass only the region of interest about 340 nm, passes some light centered around 322 nm and light above 700nm. The light above 700 nm is filtered out by placing a short-pass filter with a cut-off wavelength of 650 nm. Combined, the light reaching the camera is effectively reduced to the narrow band about 340 nm which effectively captures the second most abundant line at 337 nm. The transmission curve for this filter stack can be seen in figures 13 and 14. This filter stack passes light with a transmission of above 75% at 340 nm and a blocking fraction down to 10^{-5} in the out-of-band regions of the spectrum.

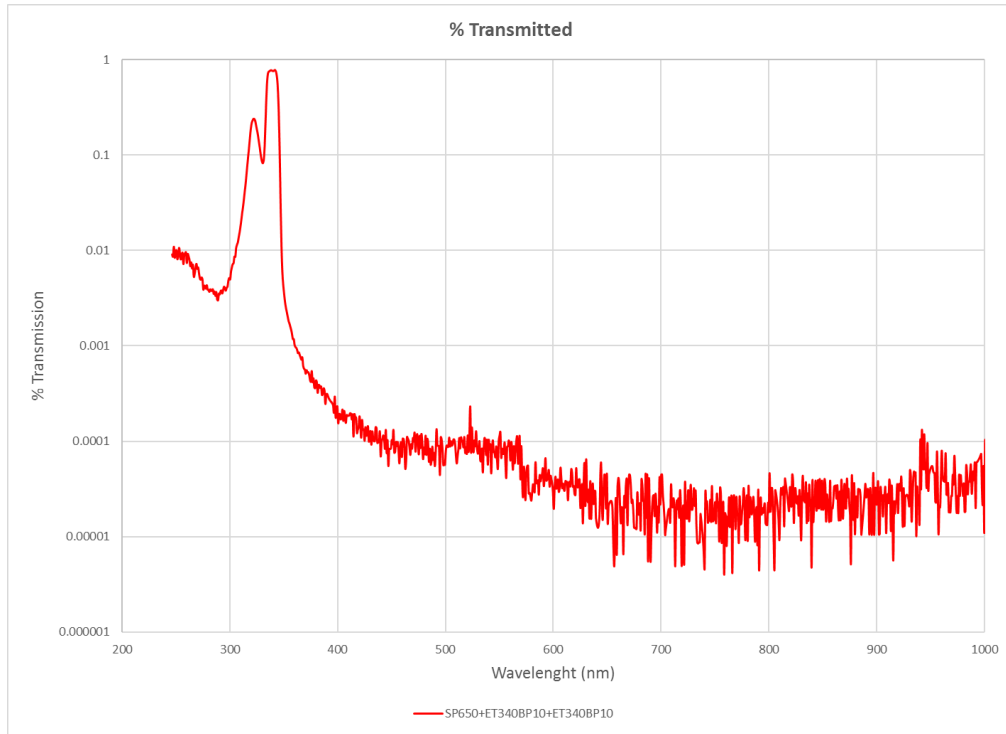


Figure 13: ET340BP10 stack transmission curve. Full-Spectrum transmission curve of the ET340BP10+ET340BP10+SP650 filter stack used in the assessment of acquisition settings

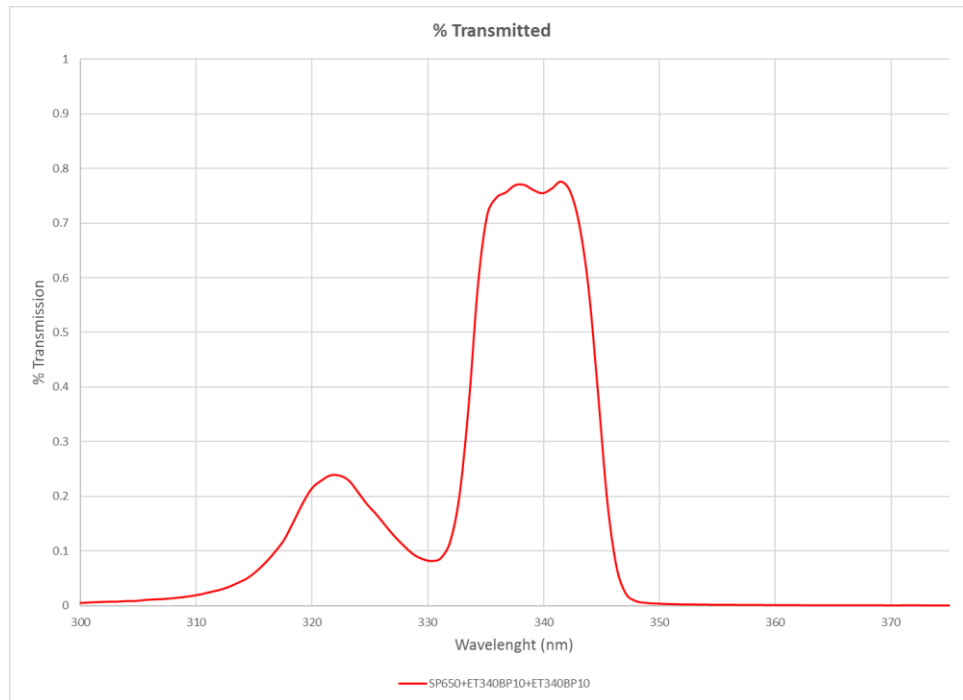


Figure 14: ET340BP10 stack transmission curve in UV. UV-portion transmission curve of the ET340BP10+ET340BP10+SP650 filter stack used in the assessment of acquisition settings

The target was designed with 1 cm graduations so that the range could be determined from the image and that focusing could be confirmed with the text on the target. The source placed on the pedestal was a Po-210 source (model 1U400) from NRD Static Control. It is estimated that at the time of measurement the activity of the source was approximately 200 uCi. Po-210 emits a 5.3 MeV alpha particle and decays with a half-life of 138.4 days (ENSDF, 2018). There is gamma emitted at 803 keV that is emitted 0.001% of the time. Even with very active sources, this does not contribute to the dose in air appreciably. Figure 15 shows a visible light image of the target setup with the source placed on the pedestal.



Light-Tight Box

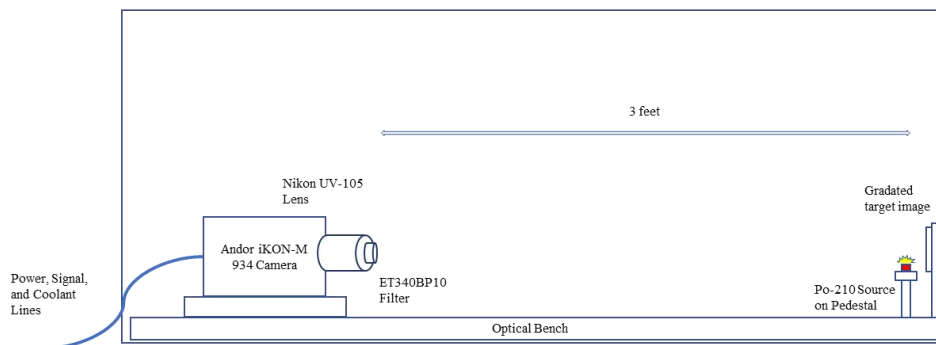


Figure 15: Acquisition setting optimization experiment target image and apparatus

The entire apparatus was set up in a light-tight box fixed to an optical bench and penetrations to the box were sealed with optical tape. Using the liquid cooling heat exchanger made it possible to disable the cameras cooling fans so air circulation was unnecessary for operation. The dark box made it possible for very long exposures to take place without interference from room lights. This apparatus was used to evaluate the range of settings possible with the camera. Measurements were taken for every combination of the settings in table 5 (288 individual measurements).

Table 5: Acquisition settings evaluated for ODR application

Acquisition Times (seconds)	Chip Temperatures (°C)	Readout Binnings
10	-30	1x1
30	-40	2x2
100	-50	4x4
300	-60	8x8
1000	-70	16x16
3000	-80	32x32
	-90	
	-100	

Due to the large number of images needed to cover the range of analysis settings, automation of the acquisition was necessary to perform the measurements. The camera used was the Andor Technology iKON-M 934 Series with the BU2 CCD sensor (Andor Technology, 2008). Andor cameras come with a built-in control language called Andor Basic. Using this scripting language, the camera and acquisition settings can be controlled so that subsequent measurements and file storage operations can be carried out automatically. An automation code was composed to perform the experiment. A copy of the code and the functions it calls to carry out this experiment are described in detail in appendix A.

The Effect of Electronic Superpixel Binning on Detection Sensitivity

The readout of a CCD can be conceptualized as an array of individual photon detectors that are each read to yield a matrix of individual pixel values. Each detector (pixel) has an inherent detection efficiency and background. To improve measurement sensitivity, one may consider adding the signals of neighboring pixels together to form a composite pixel or “superpixel”. In effect, this increases the detector volume by a factor of the

number of pixels summed which will increase detection sensitivity. However, with each pixel added to the superpixel, its background comes along with it.

Each pixel has an inherent background value for a given measurement, this is referred to as dark noise, the pixel value when no photons interact with it. In addition to dark noise there is readout noise, extra uncertainty added to the measurement by the process of electronically reading out the individual pixel value. Compared to dark noise, readout noise has a much stronger impact on overall background of an individual pixel. If a CCD is read out and then summed, the increased detection efficiency will be realized along with an increase in the background. Thus, the superpixel array pays a compounded readout noise penalty equal to the number of pixels summed.

Alternatively, the pixels can be summed together prior to readout to avoid paying the readout noise penalty. This process is referred to as electronic binning and is shown graphically in figure 16. During the chip readout, individual pixels can be summed to form superpixels and the readout background penalty is paid only once since it is a result of the readout process alone. Binning the chip into superpixels in this way greatly improves measurement sensitivity by increasing the detection efficiency but with only a slight background increase due to the individual pixel dark noise. Of course, the spatial resolution is degraded proportionally since there are fewer pixels to form an image.

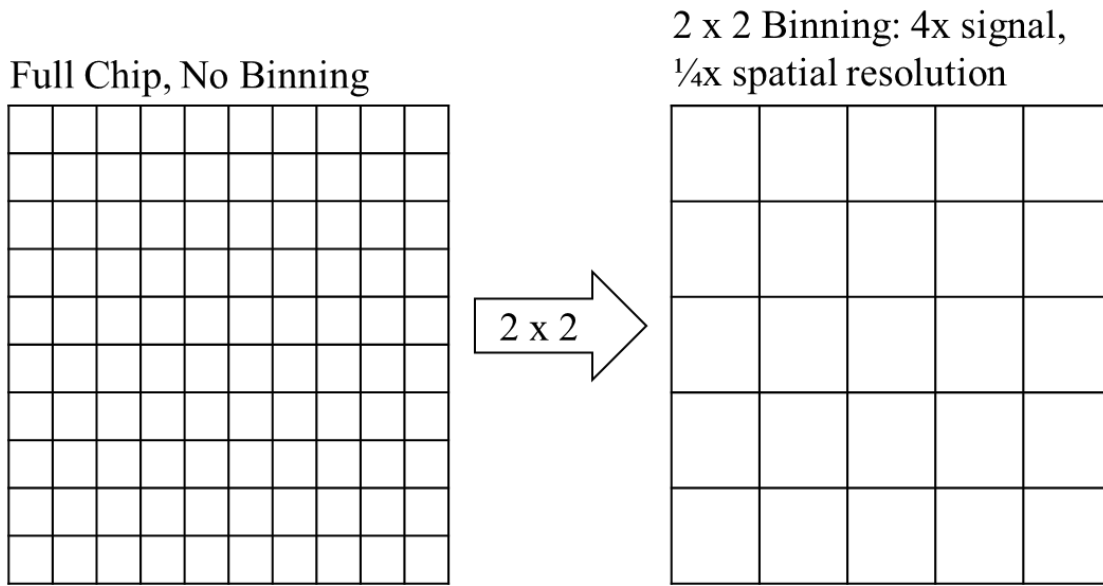


Figure 16: A visual description of electronic binning

Laboratory measurements were performed to confirm the improvements that could be realized by electronic binning as well as to determine any practical limits to electronic binning settings. Images from each binning setting for the $-90\text{ }^{\circ}\text{C}$, 1000 second acquisitions were analyzed to demonstrate the effect binning has on measurement sensitivity. Figure 17 shows these images in sequence. The images reveal that increasing electronic binning increases the contrast of the source region against the background. Spatial resolution is lost as binning size increases, as expected. The images also reveal that as binning size increases, the impact of direct CCD strikes by ionizing radiation on the image is magnified.

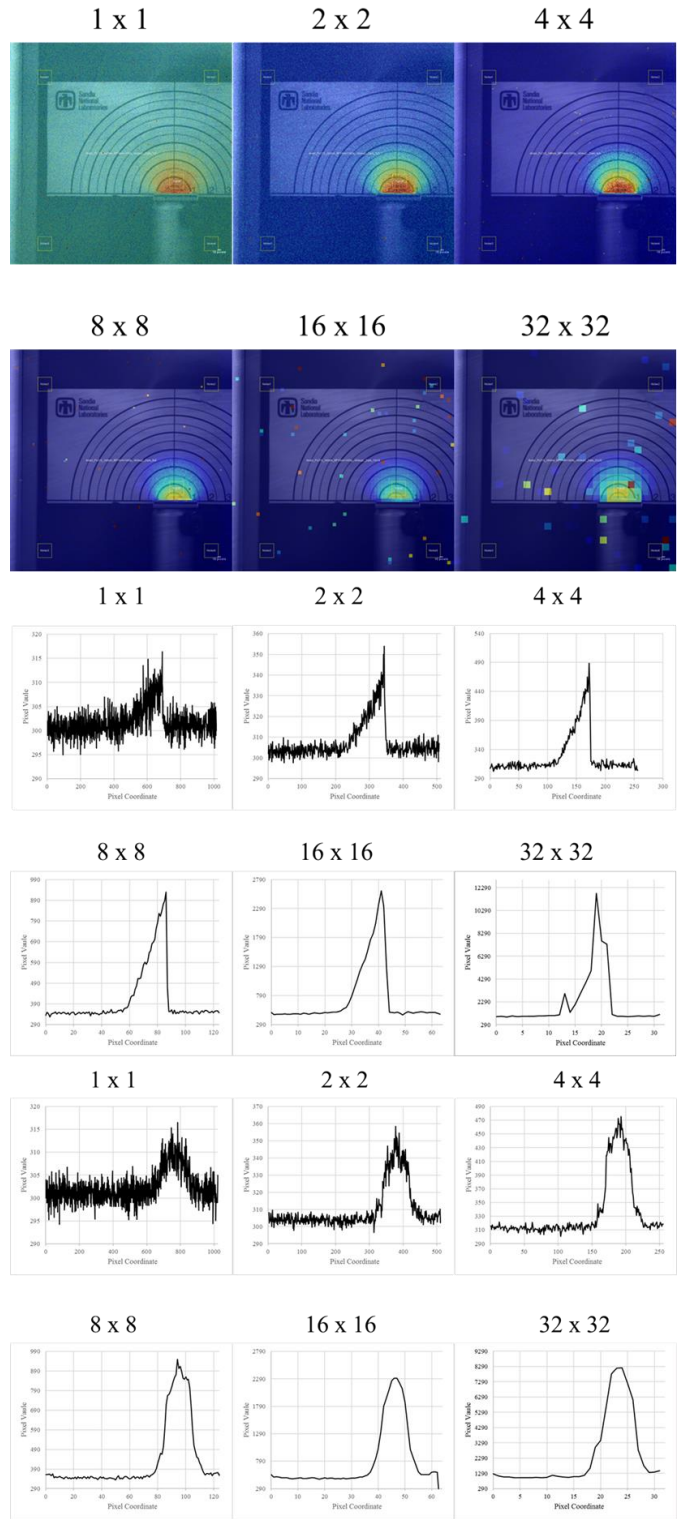


Figure 17: Results from the binning evaluation experiment. Each pane is the overlaid 1000 second acquisition at -90 °C chip temperature on a visible image of the target. Horizontal and vertical slices are taken that visually demonstrate the improvement to the signal to noise ratio.

A quantitative analysis of the images from the binning evaluation experiment reveals the true impact of the direct radiation strikes. Table 6 shows the mean pixel values for the four background regions and the source region, the contrast (from Eq. 3), and the signal-to-noise ratio (SNR from Eq. 4) along with their 1-sigma uncertainties. The uncertainty in the average background appears to be the culprit in skewing the uncertainties in the contrast and SNR. For measurements where the background regions were consistent, the contrast and SNR are more reasonable. Measurements having background regions that contained one or more hot-pixels led to unreliable contrast and SNR values.

Table 6: Quantitative image results of the binning evaluation experiment

Bin Setting	Average Background (Counts per second)		Average Signal (Counts per second)		Contrast (C)	Signal to Noise Ratio (SNR)
1x1	0.12	± 0.1	0.18	± 0.04	0.5 ± 0.4	1.8 ± 2
2x2	0.08	± 0.02	0.25	± 0.05	2.1 ± 0.7	13 ± 4
4x4	0.09	± 0.09	0.61	± 0.1	5.8 ± 5.9	6.8 ± 7
8x8	0.24	± 0.9	2.3	± 0.4	8.6 ± 32	2.6 ± 10
16x16	0.75	± 2.1	7.4	± 1.2	8.9 ± 25	3.5 ± 10
32x32	0.5	± 0.08	32	± 5	63 ± 14	400 ± 89

These results make it clear that there is a need to minimize the impact of these direct CCD strikes on the results. Reducing the overall number of direct strikes will reduce the chance that they skew the results as seen above. More intelligent algorithms to remove outlier background regions may help improve results as well. Regardless of the somewhat inconsistent results due to artificial uncertainties, the contrast and SNR clearly improves with binning size. In practical ODR applications, the required spatial resolution

needed and the probability of direct radiation strikes on the CCD must be weighed against the improvement possible by increasing electronic binning size.

The Effect of CCD Temperature on Noise Reduction

Thermoelectric (TE) cooling of CCD chips is essential in reducing the dark current of the semiconductor for low-light imaging applications. While this is important in both types of CCDs (iCCD and EMCCD), it is absolutely critical to cool the EMCCD because signal multiplication happens to the signal during readout. Alternatively, the amplification of the signal for iCCD design is done by intensifying the light itself which produces on-chip signals that are much larger than the dark noise so cooling is less important.

TE cooling is achieved with high efficiency using vacuum insulated sensors and liquid heat transfer circuits. The cameras used at Sandia can achieve temperatures as low as -100 °C. To determine the effect of deep TE cooling on image quality in ODR, several measurements were taken of the Po-210 source at different chip temperatures while holding other acquisition parameters constant. The results of this test are shown in Figure 18. It is clear that holding the chip at a temperature as low as possible has a drastic impact on reducing the noise floor and subsequently increasing the sensitivity and contrast of ODR images.

The lowest temperature achieved in this study was -100 °C in a climate controlled laboratory while using chilled liquid coolant heat exchangers. Since the ambient environment is a major factor in cooling, field use of the equipment will limit temperatures to between -80 °C and -90 °C depending on the ambient temperature. The

images here show that as long as temperatures are -80°C and below the minimum noise floor is achieved.

Another important lesson learned was that while operating the cameras with chilled liquid heat exchangers, careful attention must be paid to the dew point of the environment.

Chiller temperatures must be kept above the dew point to avoid producing condensation inside the camera which can cause catastrophic damage to the equipment. A simple digital hydro thermograph used in the field allows you to set the chiller temperature to an appropriate level. Even in humid and higher than room temperature environments, the chilled liquid coolers are efficient enough to remove heat from the TE cooler such that the chip temperature can remain at the optimum level. While experiments were not conducted with non-chilled liquid heat exchangers, it is not clear if these would be able to achieve the appropriate cooling efficiency in these extreme conditions.

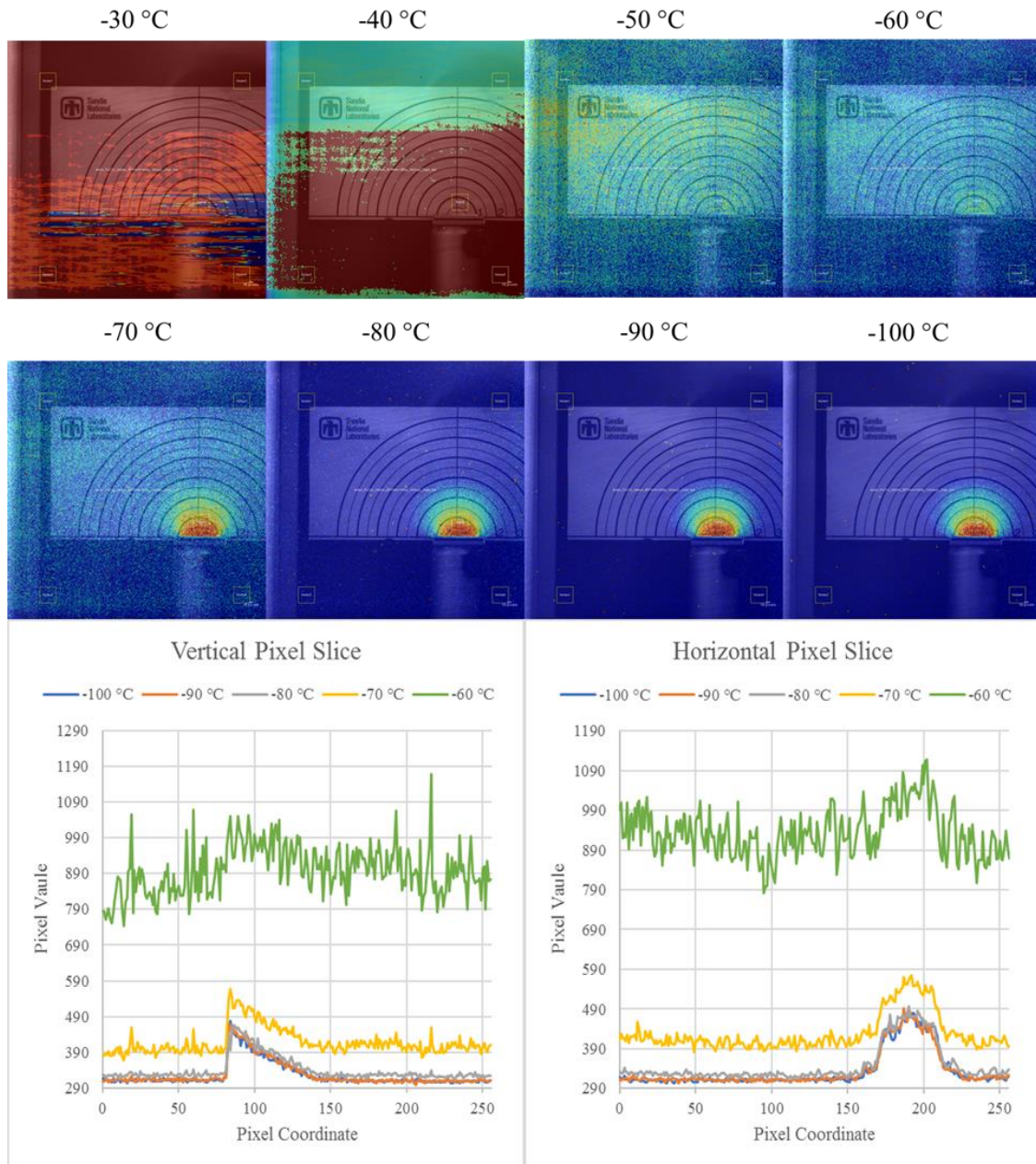


Figure 18: Effect of deep thermoelectric (TE) cooling on CCD image noise. Each pane is a 1000 second exposure binned at 4x4. A vertical and horizontal pixel slice is taken from each image. The noise floor is reduced as the temperature decreases. Results show diminishing returns as temperature goes below -80 °C.

It is also important to note that these cameras can cool themselves down to -80° C with fan-based heat removal alone in laboratory environments. Outside of carefully controlled climates, we observed that fan cooling was not adequate. Another advantage to liquid

heat exchangers is that while coolant is circulating, the fans are not needed and the camera can be placed in an environment where air flow is limited such as a light-tight box or even in a close-fitting radiation shield. In situations where the cameras are to be placed in shielding or telescope configurations, liquid cooling is key.

The Effect of Acquisition Time on Detection Sensitivity and Background

In situations where the signal is very faint, such as is the case in ODR, longer than normal exposure times are needed to obtain an observable signal. Such long exposure times present several challenges in CCD imaging. Images can be blurred if there is any motion during the acquisition time. Background light must be absolutely minimized through control of the environment and/or optical filtering to avoid saturation of the sensor. Long acquisition times increase the probability of detecting direct radiation strikes on the sensor that can saturate pixels. Direct radiation strikes are due to natural background radiation, cosmic rays, and perhaps even the longer-range gamma radiation from the imaged material itself.

To observe the effect of increased acquisition times, several images were taken of the Po-210 source while holding other analysis parameters constant. Figure 19 shows the effect of count time on image quality. Clearly, longer acquisition times allowed for stronger more statistically significant signals to be observed. However, with longer acquisition times came more observable direct radiation events on the sensor which make image processing more difficult. In environments with increased radiation background, this phenomenon limits the practical maximum acquisition time which can limit the achievable detection level to a point where the signal is no longer observable.

The images in figure 19 are not median filtered, only contrast enhancements are made to the images. It is clear that without filtering, the direct strikes on the chip can impede the ability for false-color mapping to identify the source region. In the 3000 second exposure, the source region appears more faint than the 1000 second exposure, this is because the several direct strikes observed in 3000 seconds skew the false-color mapping scale. The stripe to the left of the images is an artifact of chip readout noise. As the chip reads out horizontally, the noise is compounded and shows up as a vertical stripe on the edge of the chip. This is most apparent in the very-near-background images and can easily be cropped or filtered out of the image.

There are several ways to reduce the number of direct camera strikes from ionizing radiation. The same principles of radiation safety apply of time, distance and shielding. If acquisition time is kept to a minimum to observe the signal, the direct strikes will be minimized. If the camera is placed far enough away from the source of ionizing radiation, the number of direct strikes will be minimized. If the chip is shielded from the ionizing radiation, the number of direct strikes will be minimized.

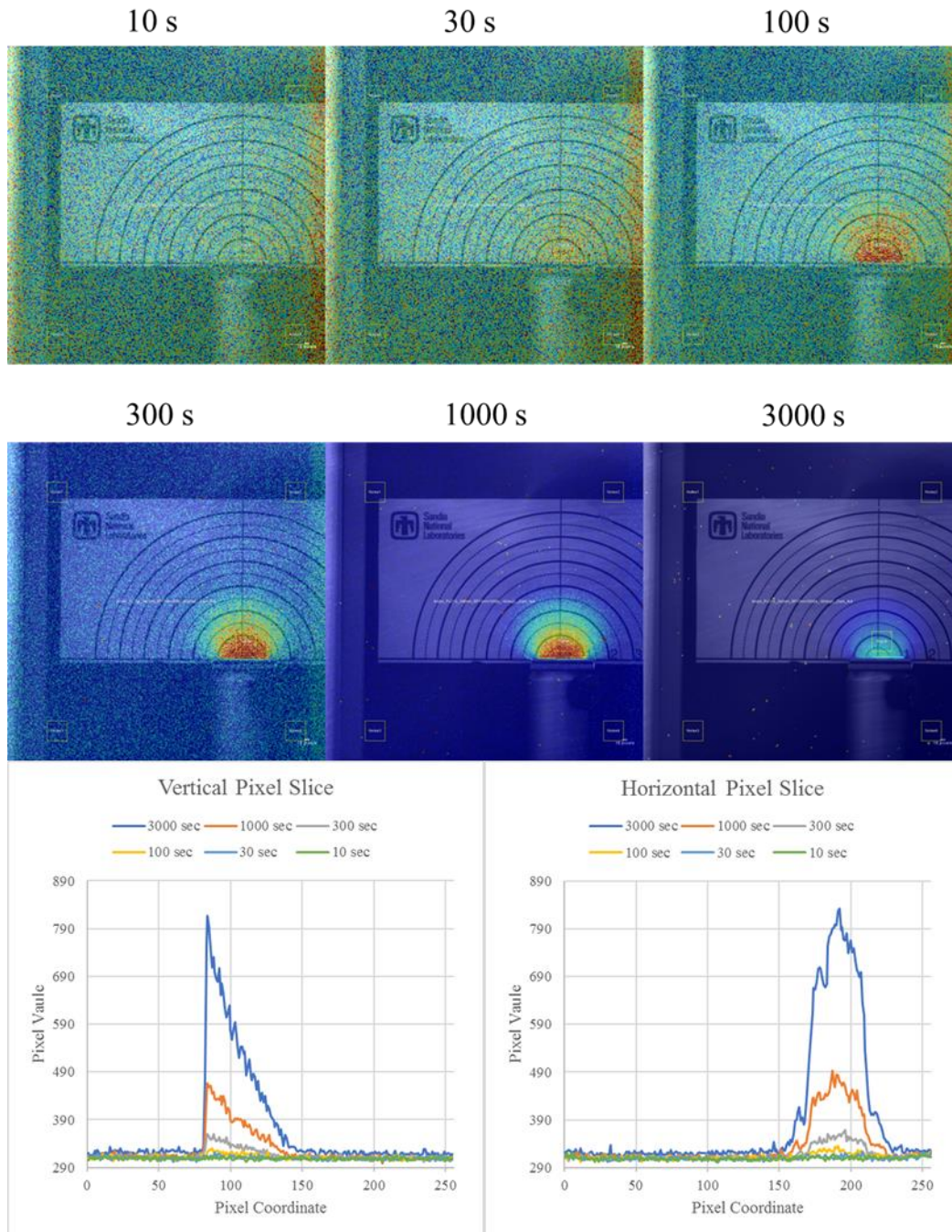


Figure 19: The effect of acquisition time on ODR measurements. Each pane is an exposure at $-90\text{ }^{\circ}\text{C}$ with a binning of 4×4 . A vertical and horizontal slice is taken from each image showing the improvement to the signal to noise ratio with increased acquisition time.

In many situations, long exposure times are required to observe the signal above the noise floor. A method for obtaining the acquisition time while minimizing the direct strikes is

to take a series of shorter exposures back-to-back and sum them up in post-image processing. During summation, a temporal median image filter can be applied to remove the saturated pixels. This method will be described in a latter chapter.

In environments with higher than background radiation fields, it is important to keep the camera as far away from the source as possible through the use of telescoping collection optics. Of course, a farther optical path leads to losses in signal. The decrease in saturated pixels achieved by distance must be weighed against the decrease in detection efficiency for imaging from farther away.

Reducing the cross section of the sensor to the radiation field is a high-impact, low cost method for reducing direct strikes. Using a simple UV reflective turning mirror in the optical path from the camera to the source, the sensor face can be placed parallel to the radiation flux. By doing this, the number of direct strikes on the chip is greatly reduced simply because the surface area available for the flux of radiation is reduced to essentially the thickness of the sensor. In field tests discussed later in this report, this approach has proven to be a very valuable method to reduce direct strikes.

Finally, shielding the chip from ionizing radiation has proven to be an effective method for reducing the number of saturated pixels in an image due to direct radiation strikes. A custom-made tungsten polymer (density of 6.92 g/cc) shield was designed to closely cover our cameras in situations where higher than background radiation is present or very long exposures are needed. Tungsten has a mass attenuation coefficient of $0.1378 \frac{cm^2}{g}$ for 500 keV photons (National Institute of Standards and Technology, 2018). Using a simple exponential attenuation model, the tenth-thickness of this material for 500 keV photons

was found to be about 1 inch. The shield was evaluated at 500 keV because this energy is near the center of the range of energy that natural gamma rays take. The shield surrounds the entire camera with heavier shielding (1 inch) around the location where the sensor is placed in the camera housing. Thinner shielding (1/2 inch) is placed around the rear of the camera to reduce the overall weight of the shield. An opening in the shield is drilled out for the lens and a small gap in the back is built in for running coolant lines, power, and signal cables. The lens opening allows for an unshielded path for radiation to strike the chip. To mitigate this shortfall, a simple turning mirror can be used to orient the camera sensor parallel with the radiation flux to reduce the cross section to the sensor. A drawing of the shield can be seen in figure 20.

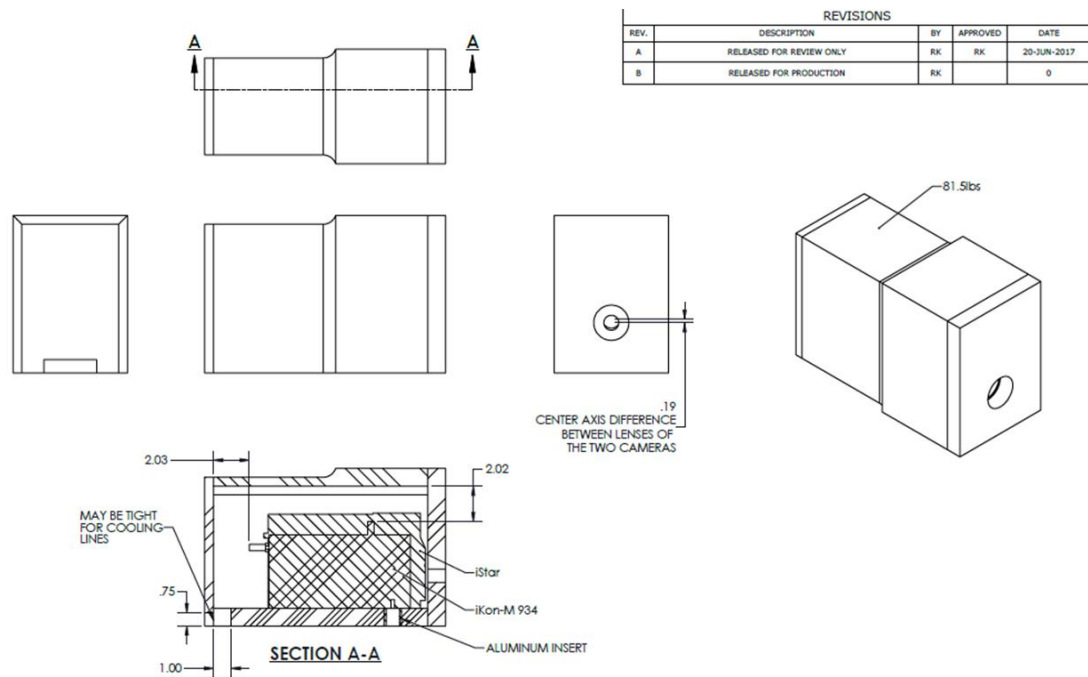


Figure 20: Drawing of tungsten polymer camera shield

When designing shielding for these types of cameras we found that it is important to consider the cooling requirements of the camera. A tight-fitting shield does not allow for enough air flow for the on-board air cooling mechanism to effectively cool the CCD.

Thus, forced liquid cooling is necessary to achieve the optimum temperatures.

Furthermore, the added weight to the equipment (80 pounds) can limit the cameras use in telescope systems where carefully counter balanced weights are needed to stabilize the tripod. Ideally, a camera specifically engineered for ODR would have shielding built into the sensor housing itself which will minimize the mass of the system.

This shielding, in theory, reduces the flux of incident radiation to the sensor by a factor of ten. This means exposures of up to ten times longer can be taken at the same level of radiation-induced image distortion. This feature of the ODR system proved to be critical in environments where higher-than-background radiation fields were present or when exposures of longer than 10 minutes were taken.

Summary of Lessons Learned in Evaluating Acquisition Settings

Several important lessons were learned in optimizing the acquisition settings for the ODR configuration. Measurement sensitivity increases with acquisition time as expected.

Electronic binning enhances sensitivity and contrast by increasing the signal while maintaining the same background. Chip temperature reduces noise greatly but has diminishing returns between -80 °C and -100 °C. All of these settings however must be balanced against the probability of direct CCD strikes by cosmic rays, natural radiation background, and even the source field itself.

Direct strikes happen randomly and skew the contrast of the measurement images. These hot pixels have values orders of magnitude larger than even the largest pixel values in the signal region. Shorter acquisition times reduce the probability of direct strikes distorting the radioluminescence image. However, this must be balanced against the need for measurement sensitivity. Cosmic ray veto may be a viable option for long acquisitions but has yet to be investigated as a method for reducing this effect.

Electronic binning can magnify the effect of direct strikes. Every superpixel that contains a hot-pixel will dilute the overall value but will still skew contrast and SNR because direct strikes are so much larger than the signal pixels. As binning size increases, the chance for capturing more than one direct strike increases and more greatly skews the measurement. While binning has a dramatic effect on measurement sensitivity, it must be weighed against the probability of direct strikes skewing results. Chip temperature did not show an appreciable effect on the sensitivity to random direct strikes. However, with lower background signal that comes with a colder chip, the impact of a direct strike is magnified.

Methods to mitigate the distortion from direct strikes have been identified. Decreasing the dose rate to the CCD is the simplest approach. ODR equipment has the advantage of being able to be placed far away from the radiation source while using collection optics to gather the light from a distance. While standoff detection can reduce the dose to the CCD from the source being measured, it will not help with the natural background radiation or cosmic ray flux seen by the chip.

Radiation shielding has proven to be effective in reducing the effect of direct strikes. A custom shield made of polymerized tungsten (density of 6.92 g/cc) was fabricated to fit over the Andor iKON and Andor iSTAR cameras. The shield was designed to provide a 1/10 reduction in dose rate for 500 keV gamma rays. Laboratory and field tests have shown that this reduces the number of direct strikes. When working in environments where background radiation is elevated, it is very important to design shielding into the ODR configuration.

Radiation fields normal to a CCD will produce the most direct strikes because the effective fluence on the chip is maximized. Furthermore, looking directly at the source with the camera provides an unshielded path for radiation to enter the camera through the lens. Thus, when working in environments where a radiation field incident on the chip is expected, placing the CCD chip face parallel to the radiation field greatly reduces the effect of direct strikes. Placing the chip parallel to the field reduces the cross-section by several orders of magnitude. Pixels on the edge of the image on the side closest to the source will show more direct strikes than those on the other side. This will have less of an impact on the overall measurement as they are more easily cropped from the region of interest on the chip than randomly placed hot pixels.

Using a turning mirror in the light collection optics allows for this orientation and can in fact, improve the signal by adding more filtering to the collection chain when a UV coated mirror is used. Light in the visible band and above is passed through the mirror while UV is reflected preferentially toward the camera. This reduces the overall amount of out-of-band light reaching the filter in a closed system and in turn will reduce the

amount of leakage through the filters. Thus, it is recommended that in most ODR measurements, the camera be oriented such that the chip face is parallel to the incident radiation field.

Finally, image processing prior to the identification of a source and contrast/SNR calculations can be used to reduce the impact of direct chip strikes by ionizing radiation.

A median image filter has shown to be effective in reducing and removing these hot-pixels. The filter can be applied to a single image (mathematical filter) or be applied using a sequence of back-to-back acquisitions (temporal filter). The details of these filtering approaches will be described in a later chapter. It is recommended that all images obtained in ODR be corrected for the remaining direct strikes using these types of filters prior to other image processing activities.

Sandia's ODR Configurations

Through extensive testing and field experience Sandia has developed three unique ODR configurations. The Pathfinder system, the first of the three designs, utilizes conventional astronomy telescope optics modified for use with optical filters and an EMCCD camera (See Figure 21). The Demonstrator system is an updated version of the Pathfinder with custom coated optics that allow it a wider range of detectable wavelengths. Finally, the compact system is designed for closer-range measurements in tighter quarters and utilizes a lens-based collection optic.

The Pathfinder was designed for long-range ODR detection and was used for outdoor measurements at the Sandia Gamma Irradiation Facility (GIF). The GIF is a 1000+ Ci Co-60 source at Sandia National Laboratories used to perform irradiation experiments.

The Pathfinder demonstrated ODR was possible at very long ranges. (Harrison, Martin, Wiemann, Choi, & Howell, 2015) Utilizing largely COTS optics, the Pathfinder was only sensitive to the weaker 390 nm line of nitrogen fluorescence. The shorter, more abundant wavelengths were not reflected by the primary mirror of the telescope. Table 7 below tabulates the optical efficiency of each component yielding an overall detection efficiency of 14.3%.

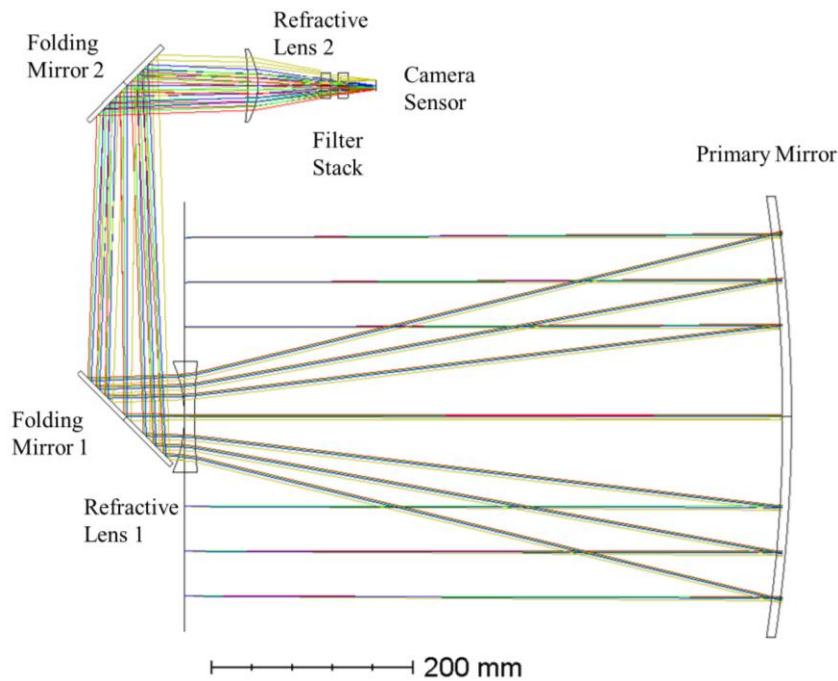


Figure 21: Optical Design of the Pathfinder and Demonstrator Systems

Table 7: Detection Efficiency of the Pathfinder ODR System

Optical Component	Make/Model	Notes	Optical Efficiency
Celestron CGE Pro 1400 Primary			55%*
Refractive Lens 1	Newport 60D20AL.2		92%
Fold Mirror	Edmund Optics 84427		80%
Fold Mirror 2			80%
Refractive Lens 2	Custom	Fused Silica	92%
Filters	SP650+ET390BP10	10 nm bandpass at 390nm	80%
Camera	Princeton Instruments 512B Excelon Coating	EMCCD with UV Coating	60%
Total Detection Efficiency:			14.30%

*Estimated, extrapolated from performance above 400nm

The demonstrator, also designed for long-range use, was built in the same geometry as the Pathfinder (figure 21) but with custom optics specifically designed to optimize light collection for ODR. As seen in table 8, the overall detection efficiency of the Demonstrator comes in at 37.3% at 340 nm and 43.8% at 360 nm. This is not only a vast improvement to the Pathfinder, it is designed to detect the much more abundant lines of nitrogen. Nearly 90% more signal is captured by this system because it is collecting both the 340 nm and 360 nm lines. Not only does this configuration have a much larger collection efficiency, the noise and background levels are much lower due to improved TE cooling, lower natural background at the shorter wavelengths, and optics that reject more out-of-band light.

Table 8: Detection Efficiency of the Demonstrator ODR System

Optical Component	Make/Model	Notes	Optical Efficiency
Celestron CGE Pro with custom Primary	Custom Coating optimized for UV		90%
Refractive Lens 1	Custom Coated for UV	Fused Silica	99%
Fold Mirror 1	Custom Coated Edmunds $\lambda/10$ 6" dia.	Dichroic coating passes off-band light	98%
Fold Mirror 2	Custom Coated Edmunds $\lambda/10$ 4" dia.	Dichroic coating passes off-band light	96%
Refractive Lens 2	Custom Coated for UV	Fused Silica	99%
Filters	Chroma SP650+ CT338-360DB(X2)	2X Dual Band filter for improved signal and off-band blocking	75% @ 340nm 88% @ 360nm
Camera	Andor iKON-M 394	Back-illuminated CCD with UV Coating	60%
Total Detection Efficiency:			37.3% @ 340nm 43.8% @ 360 nm

The compact system was designed to be used in situations where long-range detection was not a concern, such as indoor measurements. With only an optional turning mirror, filter, lens, camera, and cooler, this system lends itself to situations in tight quarters where a telescope is not feasible or unnecessary. This system also allows for the use of the custom shielding to reduce radiation dose to the sensor which make it ideal for situations where radiation fields above background may be present. The iCCD camera, while optimized for UV light collection, has a much lower quantum efficiency due to the

intensifier. This system utilizes an 80mm version of the Chroma custom dual band filter with a SP650 filter placed behind the lens. This way, the aperture of the lens is not further reduced by the filter in front. The focal plane shift due to mounting a filter between the lens and camera is compensated for by a slight change in the focus setting on the lens. This system has an appreciably lower detection efficiency (table 9), largely due to the lower QE of the iSTAR camera system. However, for what this system lacks in efficiency it gains in background reduction and capability for tight measurements in extreme environments.

Table 9: Detection Efficiency of the Compact ODR System

Optical Component	Make/Model	Notes	Optical Efficiency
Turning Mirror (optional)	Custom Coated Edmunds $\lambda/10$ 4" dia.	Optional turning mirror for off-axis viewing	96%
Filters	Chroma CT338-360DB	80mm diameter filter on front of lens	85% @340nm 94% @360nm
Lens	Nikon UV-105	Fused Silica Lens designed for UV photography	60%*
Filters	SP650	Filter only available in 1" diameter so it is placed behind the lens	<i>included in filter transmission above</i>
Camera	Andor iSTAR DH334T-18U-E3	Gen 2 WE-AGT photocathode	22%
Total Detection Efficiency:			11% @ 340nm 12% @ 360nm

* Estimated from best available literature

V. OPTICAL DETECTION OF IONIZING RADIATION TESTS

Over the past 3 years several tests were conducted at Sandia National Laboratories to optimize our ODR configurations and demonstrate the technology for several applications. This section will briefly describe the experiments and present the results from the ODR measurements.

Po-210 Source in a Dark Box

Easily acquirable Po-210 sources proved to be great source material for evaluating this detection technique due to several of its characteristics. Polonium-210 is one of only a few alpha emitting radionuclides that occur in nature with a negligible gamma emission and without a beta emission in the decay chain. It is part of the uranium series decay chain. The pure emission of alpha radiation eliminates the need to consider the excitation produced by the interaction of gamma rays or beta particles in the images captured of these sources. Compared with other alpha-emitters with half-lives on the order of millions to billions of years, Po-210 has a high specific activity due to its half-life of 138 days. This means that the radiation produced per gram of material is quite large. The commercially available sources are very economical and commonplace. These sources are ideal for performing quick measurements to optimize the ODR equipment and settings prior to a larger-scale test.

A common 200 μCi Po-210 source clearly demonstrates the optical features that alpha radiation produces in air (See Figure 22). The image shows that the radiation only travels 2-3 cm in air. The concentration of the dose drops off exponentially across this distance.

The speckles in the image are due to direct strikes on the CCD from cosmic rays and other terrestrial background radiation during the 1000 second acquisition. Because the dose is so concentrated, alpha radiation is expected to be the most easily detectable form of radiation for the ODR technique. These sources proved to be useful in optimizing ODR configurations and performing focusing and quality control measurements in the field.

A continuous slowing down approximation (CSDA) model was run to estimate the vertical projection of the dose to air from the same source. The simplified CSDA model was based on NIST ASTAR stopping power data (Berger, Coursey, Zucker, & Chang, 2017). The model did not include scattering of alpha particles which explains some of the discrepancies between the modeled and the observed results. However, the range of the dose is well predicted by the model and nearly matches the observed value from the ODR measurement. It is believed that alpha scattering and secondary electron production, which were not considered in the model, account for the steadier dose drop-off than the model predicts. More robust models, such as MCNP, that include the second order interaction physics are necessary for improved model comparisons with ODR measurements.

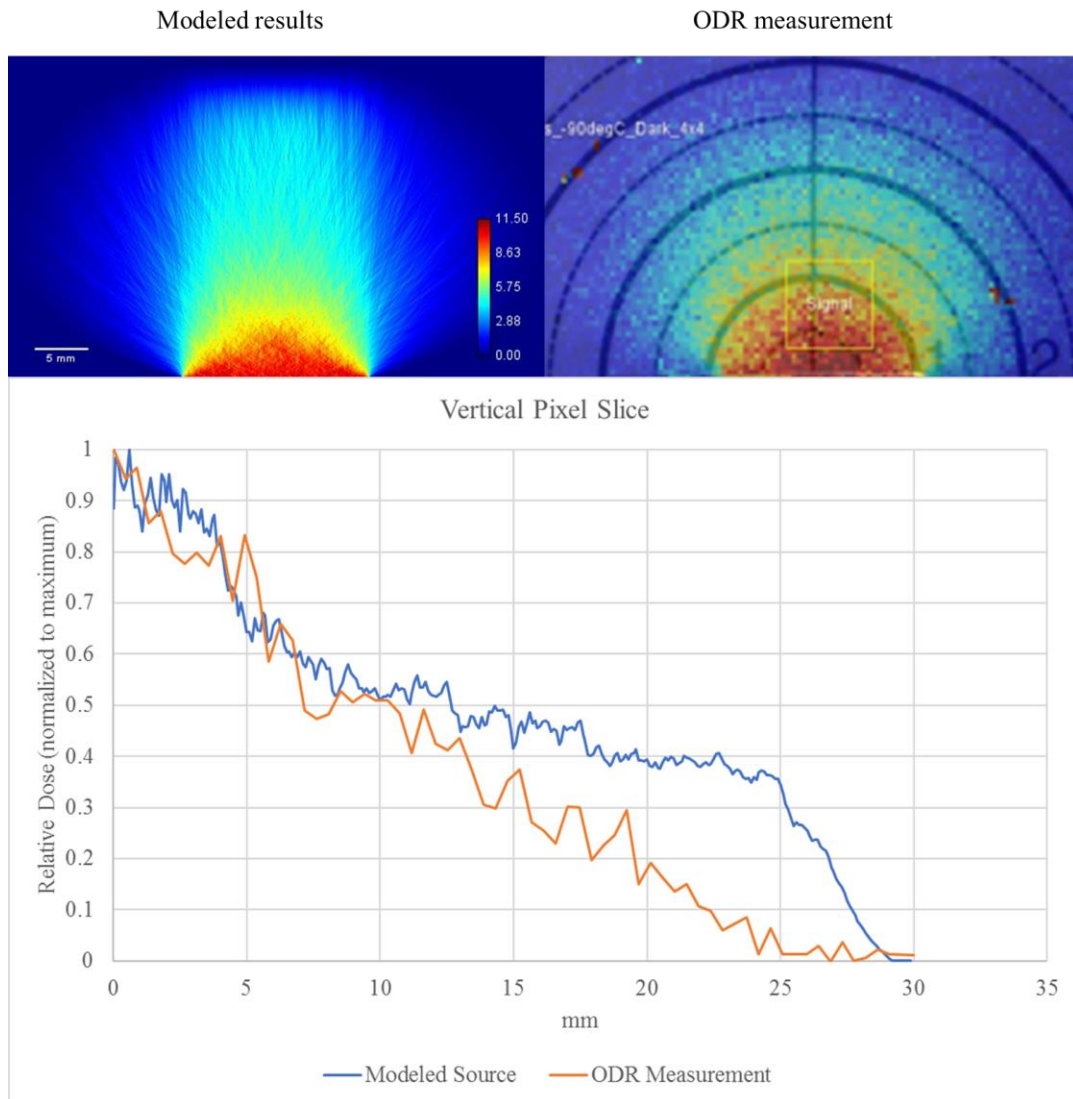


Figure 22: An image of a common 200 μCi Po-210 source compared with modeling results. Equipment: Andor iKon camera, UV lens, ET340BP10 filter; Settings: 1000 sec exposure, -90°C cooling, 4x4 binning

Po-210 Source in a Dark Room

A much more radioactive (40 mCi) source that is used for the same purpose of static elimination was acquired to perform quick measurements with the ODR configurations. This source is constructed in a cylindrical geometry with two source plates glued on the inside of an aluminum pipe of approximately two inches in diameter. A grating is placed

on each end of the tube to prevent tampering with the source. This much Po-210 exceeds the threshold for accountable nuclear material and came with more safety and security controls than the other sources. Regardless of the increased complexity of handling the source, it proved to be a very good source with which to perform ODR measurements.

This source was used for a side-by-side comparison of the Andor iKON and iSTAR cameras. A source this radioactive proved to be easily detected within 10 seconds using the optimized compact system from several meters away. The iKON cameras showed improved contrast likely due to the much lower dark noise of the deep-cooled CCD. The iSTAR camera showed improved resolution, as it is possible to see the grating in front of the source material in those images (see Figure 23). However, this may be due to differences in focus between the two tests, as it was difficult to maintain focus because the same lens was used on both cameras.

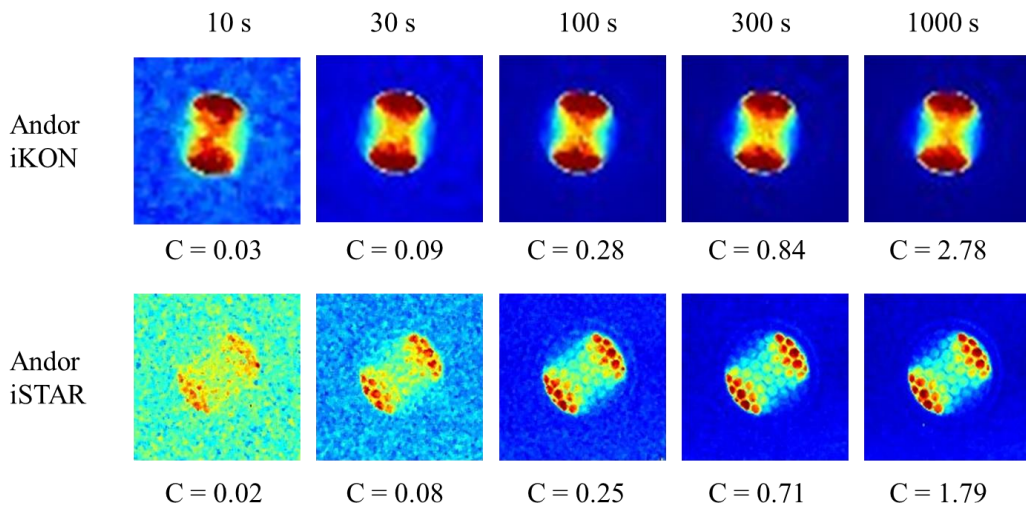


Figure 23: Camera comparison using the 40 mCi Po-210 source in a dark room

Cs-137 Shepherd Irradiator



Figure 24: The Shepherd Irradiator Model 89-400 at Sandia National Laboratories

The Shepherd irradiator model 89-400 is typically used to produce a self-contained calibrated dose field for the purpose of calibrating health physics instrumentation. The irradiator has a range of 100 $\mu\text{R/hr}$ to up to 1,500 R/hr exposure rates. The system utilizes two Cs-137 sources that can be toggled individually behind several collimated shields to produce the desired exposure rate in the chamber. The Shepherd Irradiator has two port holes into the dose chamber (opposite side than the one shown in figure 24). The port holes provide a clear path into the irradiator for telescoping-type probes.

Since the port holes offer an unobstructed optical path to the dosed region of air, the shepherd provides a great opportunity to utilize ODR on a calibrated dose region across several orders of magnitude. While only preliminary scoping measurements of the Shepherd have been made to date, the team plans on utilizing this equipment to study the important factors in correlating image strength of an unknown source to the actual dose rate. Having a calibrated and adjustable source will be critical in determining the best approach to calibrating the ODR equipment.

Shepherd Irradiator port ~15 ft.
away



10 min 4x4 binned exposure
609 R/hr

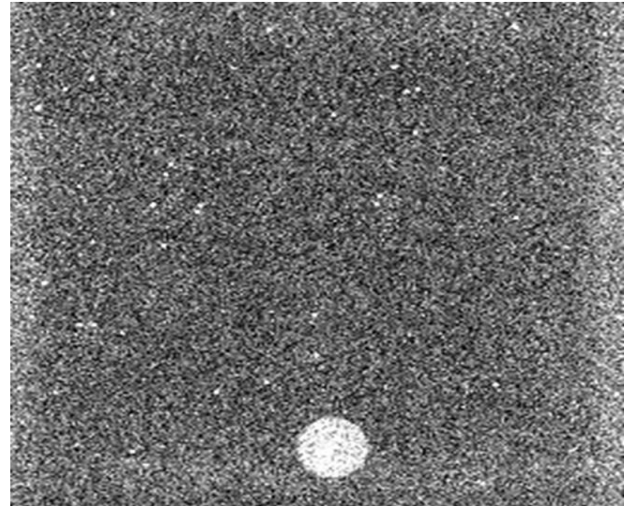


Figure 25: ODR measurement of the Shepherd port . Alignment/Focus image of Shepherd Irradiator telescoping detector port open. (right) 10 min exposure of open port at 609 R/hr inside the chamber.

To determine the feasibility of using this equipment, a measurement was made at the maximum achievable dose rate for the instrument. Given the current radioactivity of the sources inside the Shepherd, the maximum dose rate achievable at the center of the chamber is 609 R/hr. The camera was set up approximately 15 feet away and focused straight on with the port. The Andor iKon camera with Nikkor lens and SP650 and ET360BP5.5 filters were used. A 10-minute exposure with 4x4 binning was captured

with room lights off and the chip at -90°C . Figure 25 shows the alignment/focus image (left) and the filtered image (right). The ODR setup was very easily able to contrast the port hole against the background which shows that this equipment will be very useful in correlating image to calibrated dose rate in future measurements.

Irradiated Yttrium-90 at the Annular Core Research Reactor at Sandia National Laboratories

Beta radiation is a major contributor to the localized dose for many of the common source terms that may be encountered in the environment. Thus, it is important to study how ODR can be used to observe beta dose. To perform these measurements in a controlled environment, highly purified yttrium foils were irradiated with thermalized neutrons at the Sandia National Laboratories Annular Core Research Reactor (ACRR). This reactor, designed for these such irradiations, was able to transmute stable Y-89 into radioactive Y-90 at a relatively fast pace that yielded enough material to be observed by the ODR equipment.

Y-90 is a pure beta emitter with a half-life of 64.1 hours. It decays to stable Zr-90 by emitting a beta particle with a maximum energy of 2.28 MeV. It can be produced by the bombardment of stable Y-89 with neutrons. Yttrium-89 was chosen for a target due its relatively low cost, low impurity content, stability, and affinity for neutron absorption. Preliminary calculations showed that with a 15-minute irradiation the foils could be activated to a total of 0.033 Ci. The predicted radioactivity of the activated foils would yield a dose rate in the thousands of R/hr which would be easily detected using the ODR equipment.

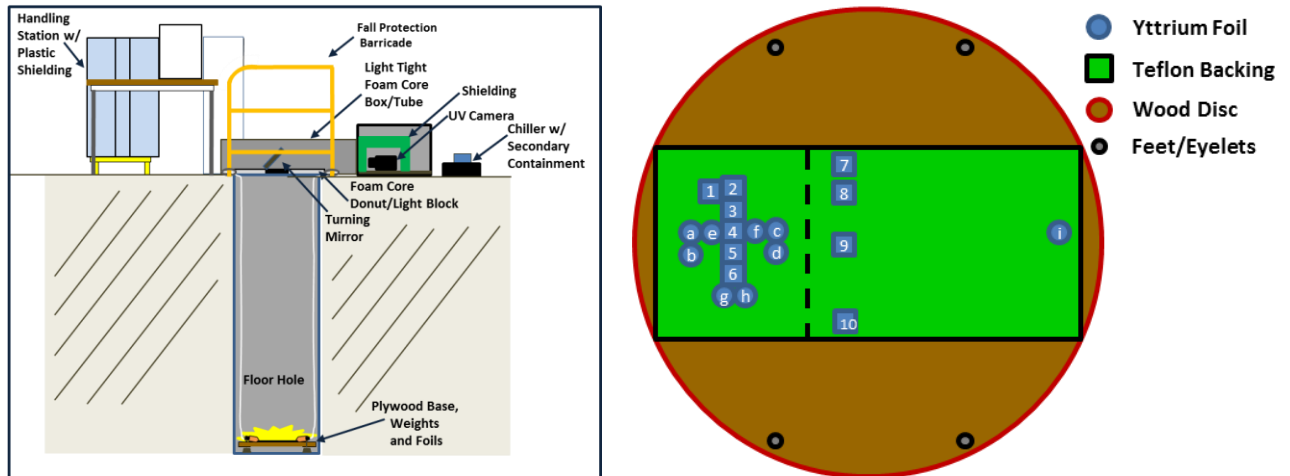


Figure 26: ACRR foil experiment test configuration. (left) Y-90 irradiation experimental layout (right) Y-90 foil layout on source platform

Nineteen one-inch diameter foils were arranged on a Teflon backing, rolled into a cylindrical shape, and placed into an aluminum irradiation can. The neutron flux was determined to be uniform across the region of space the filters occupied in the core. The foils were irradiated for 15 min at a low power in the core and transferred from the core to a holding area where short-lived byproducts in the materials were allowed to decay for 30 min. At a handling station with appropriate personal protective equipment and radiation controls, the foils were then removed from the can, rolled out onto a plywood base and lowered into a floor well. The ODR camera, lens, and filter array were placed in a shielded, light-tight box on the floor above the well and aligned with a UV-coated turning mirror to image the foils at the bottom of the well. The standoff distance from the camera to the sources was approximately 9 feet. Figure 26 is a drawing of the experimental layout and the foil pattern on the source platform. Images of the foils were captured over several days as the material decayed to levels undetectable by the ODR configuration (see figure 27).

Several interesting features in the images of the irradiated foils were observed. First, the alignment with the mirror was not perfect and a portion in the corner of the image was actually looking away from the source beyond the turning mirror. This feature in fact proved to be very beneficial in determining the contrast of the image. Having a known background region in an image helps scale the image to determine the contrast to noise ratio of the actual source material. There was some edge blurring due to defects in the mirror coating. The nylon cord used to position the source platform at the bottom of the well appears to have either been excited by the radiation field, scintillating like the air around it, or simply reflecting the UV light into the camera as it clearly shows up in the images of the activated sources. This demonstrates the important fact that when using the ODR approach to detect ionizing radiation, the environment in which the source material rests can contribute to the image in unexpected ways. It is important to understand how the radiation interacts in the environment and to know as much as possible about the scene being imaged.

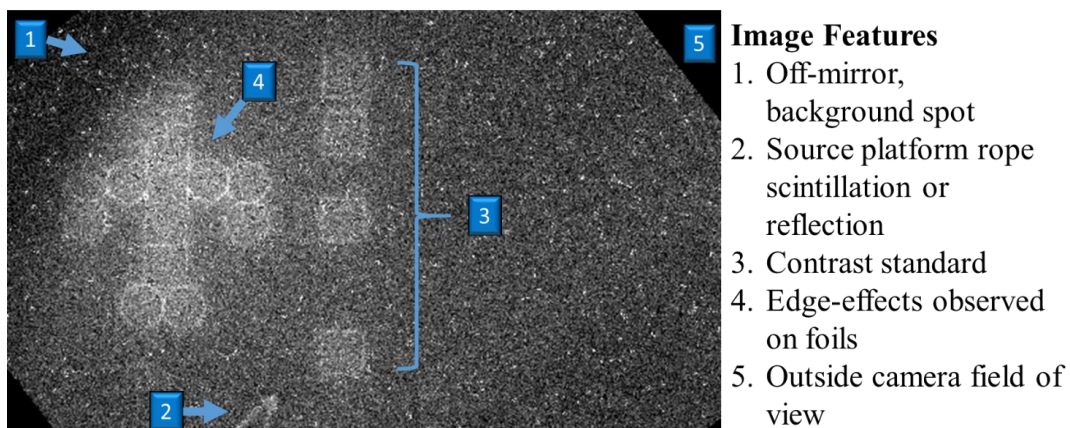


Figure 27: Results from the Y-90 foil irradiation experiment. Equipment: Andor iKon Camera, UV lens, ET360BP5.5 filter, UV turning mirror. Settings: 30ksec exposure, -90 °C cooling, 2x2 binning

Most notably, the dose from the foils does not appear to be uniform as it does for alpha sources. It appears that the dose is much more concentrated on the edge of the foils. We postulate that the edges are brighter in the UV because the dose is more concentrated from low energy beta radiation leaving perpendicular to the foils edge. Low energy betas are stopped in only a few millimeters of air before interacting as opposed to the high energy betas that can travel several inches before ionizing a molecule. Furthermore, they are only emitted in the upward direction on the face of the foil. On the edge of the foil, these low energy betas are emitted in nearly all directions which explains why we observe a brighter ring around the foil. The air around the edge of the foil receives more dose because of the low energy betas are making it out of the foil itself. Figure 27 above shows these features in an early image of the irradiated foils.

This phenomenon may be a very important, and in fact, useful feature of the ODR method. Edge effects causing bright features in the images may make hot-particle detection in elevated fields more achievable. In many real-world source terms, the radiation will likely be a mix of alpha, beta, and gamma radiation. Being able to detect small hot-particles containing alpha and beta emitters in a large background of gamma dose will be very beneficial to several applications of ODR.

VI. CONCLUSIONS

Summary

Over the past three years, several experiments were carried out to optimize Sandia's optical detection of radiation (ODR) configurations and to gather data to advance the technology toward quantitative evaluation. As a result of these experiments, several important overarching lessons were realized.

- The single-most important consideration to make in any ODR application is the background ambient light in the scene. Signals from nitrogen fluorescence due to ionizing radiation are so weak, typical environmental backgrounds reaching the sensor threaten to completely hide them. Mitigation techniques involve controlling the lighting of the scene by performing measurements in the dark, picking appropriate man-made light and the use of heavy optical filtering.
- When designing optical filtering stacks, it is important to consider the entirety of the light spectrum. Manufacturers often do not provide information on the transmissivity of filters beyond a narrow range most important to the intended application of the filter. Thus, equipment and techniques must be developed to measure the full-spectrum transmissivity of any deployed filter stack.
- The angular response of filters is an important factor in the optical design of any ODR system. Off-normal light passing through the filter has different transmissivity characteristics that must be accounted for. Transmission passbands shift toward lower wavelengths as the angle of incidence increases. This

phenomenon can be used to narrow composite passbands when multiples of identical filters are used.

- Contrast enhancement, median image filtering, and careful source identification algorithms are needed to process these low-light, high-noise images.
- Long exposures or operations in higher-than-background radiation fields lead to direct radiation strikes on the sensor which distort the radioluminescence signal. Mitigation techniques involve shielding the sensor, reducing the cross-section of the sensor relative to the radiation by using turning mirrors, and single or multi-image median filtering of images to remove speckle. In most ionizing radiation detection applications for ODR these mitigation techniques are necessary to yield high-quality images.
- Deep thermoelectric cooling enhanced by liquid heat exchangers help reduce thermal noise in the sensors in many harsher-than-laboratory environments and allow for the camera systems to be operated in closed systems such as shields or dark optics boxes.
- Electronic binning has a significant impact to image sensitivity when balanced with the need for resolution in the application. However, direct strikes on the CCD can be magnified by utilizing this technique increasing need for shielding.
- It is important to consider every optical component used in the ODR configuration. Losses occur with every part and compound to decrease the signal. This is not as important in traditional optical systems due to the pretense of significant signal and can often be overlooked. In ODR, signal is so limited that every bit of transmissivity counts.

- Finally, a fully quantitative ODR configuration will rely on a combination of robust dose modeling, fluorescence predictions, light transmission modeling, and careful measurement of overall system detection efficiency in the passbands of interest. This work and a review of the literature revealed that the community is very close to this goal and through further research and development an ODR system capable of this is possible in the near future.

Potential Future Applications for ODR

The research conducted for this thesis has made it clear that this technology is indeed a viable method for detecting the presence of, and in some cases localizing, the source of ionizing radiation. While there are still some practical limitations, namely background and source strength that limit the potential uses of this technology, there are still several applications for which this application can be optimized. If the background can be controlled to a reasonable level and the source strength large enough this technique can yield low-cost, rapid, and reasonably quantified results.

In the sterilization industry, high-strength radiation generation devices (RGDs) require routine inspection and evaluation to maintain compliance with regulations. To date, facility surveys are performed by technicians through direct measurement with probes or by expensive dosimeters. Leveraging the ODR technology here could provide near real-time results without dose consequence to the radiological worker or extraneous costs to the facility budget in analyzing dosimetry. Placing a few strategic dosimeters in the radiation field and benchmarking ODR imaging to them could yield quantitative maps of the dose and satisfy regulatory requirements.

Pulsed power and radiography facilities produce very large dose fields albeit for very short periods of time. Very little has been done in evaluating how ODR can be used to observe these types of radiological events. Accurate dosimetry in these types of facilities is key in understanding the environments they produce for the experiments taking place. Thousands of dollars are spent per experiment evaluating the dose field alone so that researchers have a clear understanding of what dose their experiments receive. Sandia National Laboratories is in a very unique position to investigate this application of the ODR technique.

While dose-planning in radiation therapy is always carefully done to minimize the dose to healthy tissue in a patient, there is often no way of knowing the true dose consequence that does not rely on preliminary quality control measurements of the equipment or mathematical models. Applying ODR to the medical physics industry could help in observing beam dose during treatment to confirm beam shapes and patient dose. Little is known on the fluorescence of skin under intense radiation but this could in-fact be a promising way to image beam shape and dose patterns during radiation therapy.

Cherenkov cameras currently utilized for this purpose have a lower energy beta threshold of around 250 keV below which they are not useful. (Ciarrocchi & Belcari, 2017) ODR does not have a lower threshold and in fact, is arguably more effective for lower energy particles due to the nature by which nitrogen is excited.

Bench-scale all the way up to factory scale radiochemical processing can lead to very costly cleanup efforts during routine housekeeping procedures or decommissioning. A major component of the overall cost is that of measurement and sample campaigns with

the goal of localizing and quantifying the contamination. Using ODR to image an area can help not only localize the contamination but can provide a way to verify that decontamination efforts have been successful. These types of decontamination efforts are often most difficult for pure or majority-alpha emitting radionuclides. This is because of the very short range of these particles in air making them hard to detect in-situ or even in the laboratory. As seen in this work, of all the radiation types, this type is the most easily observed using ODR for the very same reasons.

ODR being non-destructive and non-invasive make way for it to be applied to routine facility monitoring to ensure operations remain clean and compliant with regulations. An ODR observation camera could potentially be used to monitor operations to potentially detect leakage of radioactive materials from plant components or perhaps even intentional diversion of special nuclear material. ODR could also be used as a method for stand-off detection of diverted source material.

Future Considerations for ODR Optimization

Over the past several years, Sandia National Laboratories has outfitted a laboratory with all the important components of an ODR system and successfully demonstrated three ODR configurations. Several types of cameras, dozens of filters and lenses, source material, and general optics equipment outfit the laboratory so that systems can be built for any number of measurement scenarios. These assets place the laboratory in a very good position to experiment with this technology and find more areas for which it can be used. As indicated in this research, there are still several areas with room for optimization.

One such gap is the ability to accurately model light output for a given source geometry. While others have shown this to be possible, SNL has not acquired that capability to this date. Another major gap that seems to be a challenge for most of the community is the ability to filter signals to the point where daytime measurements are possible while maintaining practical applicability. The research done here has shown the promise of customized optical filtering and presented methods for evaluating the effectiveness of such filters. Custom engineered filters may be the answer to daytime ODR measurements. Previous work done in this area should be updated with more modern filter manufacturing technology. (Lindner & Elstein, 1998)

There has been little work done in optical detection of gamma and neutron radiation. While these types of radiation will have much weaker signals than alpha and beta radiation, a strong enough source will produce a signature that is visible to the ODR configuration. More research is needed into the feasibility of detecting these types of radiation so that practical applications to the industry can be identified.

While spectroscopic measurements have been made of nitrogen fluorescence in pure gases and in air (Brett, et al., 2017) (Waldenmaier, April 2006) there has been little research done on how the spectra change for various types of radiation and intensities. A field-deployable spectroscopy instrument could allow for spectroscopic measurements of nitrogen fluorescence in-situ. Individual line yields might provide information to the identity of radionuclides for cases where this is unknown. Careful measurement of spectra can lead to more optimized filter design for several potential ODR.

VII. REFERENCES

- Abraham, J., Abreu, P., & Aglietta, M. (2010). The Fluorescence Detector of the Pierre Auger Observatory. *Nuclear Instruments and Methods in Physics Research*, 227 - 251.
- Andor. (2018, 02 03). *Deep Vacuum TE Cooling and EMCCDs*. Retrieved from Andor: <http://www.andor.com/learning-academy/deep-vacuum-te-cooling-and-emccds-te-cooling-and-darkcurrent-elimination>
- Andor. (2018, 02 03). *Minimizing Clock Induced Charge*. Retrieved from Andor Learning: <http://www.andor.com/learning-academy/minimizing-clock-induced-charge-finesse-charge-clocking>
- Andor Technology. (2008). *Andor iKON-M Users Guide*. Concord, MA: Andor Technology.
- Andor Technology. (2012). *New iSTAR ICCD User's Guide*. Concord, MA: Andor Technology.
- Atkins, P. (1990). *Physical Chemistry, 4th. Ed.* New York: W. H. Freeman and Company.
- Baillard, X., Gauguier, A., & Bize, S. (2008). Interference-filter-stabilized external-cavity diode lasers. *Optics Communications*.
- Baschenko, S. M. (2004). Remote optical detection of alpha particle sources. *Institute of Physics Publishing; Journal of Radiological Protection*, 75-82.
- Bayram, S. B., & Freamat, M. V. (2012). Vibrational Spectra of N₂: An advanced undergraduate laboratory in atomic molecular spectroscopy. *American Journal of Physics*, 664 - 669.
- Belz, J. (2005). Measurement of Pressure Dependent Fluorescence Yield of Air: Calibration Factor for UHECR Detectors.
- Berger, M., Coursey, J., Zucker, M., & Chang, J. (2017). *Stopping-Power and Range Tables for Electrons, Protons, and Helium Ions*. Retrieved April 3rd, 2018, from <https://www.nist.gov/pml/stopping-power-and-range-tables-electrons-protons-and-helium-ions-version-history>
- Brett, J., Koehler, K., Bischak, M., Famiano, M., Jenkins, J., Klankowski, L., . . . Lakis, R. (2017). Spectral measurements of alpha-induced radioluminescence in various gases. *Nuclear Inst. and Methods in Physics Research, A*, 88-93.
- Bunner, A. (1967). *Cosmic Ray Detection By Atmospheric Fluorescence, A PhD Thesis*. Ithaca, NY: Cornell University.
- Casolino, M., & Adam, J. H. (2011). Detecting ultra-high energy cosmic rays from space with unprecedented acceptance: objectives and design of the JEM-EUSO mission. *Astrophysics and Space Sciences Transactions*, 477-482.

- Chichester, D., & Pozzi, S. A. (2009). *FY09 Advanced Instrumentation and Active Interrogation Research for Safeguards*. Idaho Falls, ID: Idaho National Laboratory.
- Chroma Technology. (2018, 02 19). *Chroma*. Retrieved from Chroma: <https://www.chroma.com/>
- Ciarrocchi, E., & Belcari, N. (2017). Cerenkov luminescence imaging: physics principles and potential applications in biomedical sciences. *EJNMMI Physics*.
- Company Seven. (2018, January 16th). *Nikon UV-105, 105mm f/4.5 Multispectral Imaging Lens*. Retrieved from Company Seven Astro-Optics Division: <http://www.company7.com/nikon/lens/0105f4.5uv.html>
- Elvidge, C., Keith, D. M., & Tuttle, B. (2010). Spectral Identification of Lighting Type and Character. *Sensors*, 3961 - 3988.
- ENSDF. (2018, 01 16). *LiveChart of Nuclides*. Retrieved from IAEA Nuclear Data Services: <https://www-nds.iaea.org/>
- Fahimian, B., & Ceballos, A. (2014). Seeing the invisible: Direct visualization of therapeutic radiation beams using air scintillation. *Medical Physics v.41*, 010702-1 - 010702-6.
- Fraga, M., Onofre, A., & Pereira, L. (2008). Temperature-dependent quenching of UV fluorescence of N₂. *Nuclear Inst. and Methods in Physics Research A*, 75-82.
- G. Herzberg, K. H. (1950). *Spectra of diatomic molecules*,. New York: Van Nostrand.
- Glasstone, S., & Dolan, P. (2006). *The Effects of Nuclear Weapons*. Knowledge Publications.
- Harrison, R. K., Martin, J. B., Wiemann, D., Choi, J., & Howell, S. (2015). *New Radiological Material Detection Technologies for Nuclear Forensics: Remote Optical Imaging and Graphene-Based Sensors*. Sandia National Laboratories. Albuquerque, NM: Sandia National Laboratories.
- Hecht, E. (2002). *Optics*. Reading, Massachusetts, USA: Addison-Wesley Publishing Company.
- HIDEO, Y. (2009). *USA Patent No. 7521335*.
- Ivanov, O., Stephanov, V., Danilovich, A., & Potapov, V. (2017). The Remote Methods for Radwaste and SNF Control. *IOP Conf. Series: Journal of Physics*(781).
- Kampert, K., & Watson, A. (2012). Extensive air showers and ultra high-energy cosmic rays: a historical review. *The European Physical Journal H*, 37, 359 - 412. doi:10.1140/epjh/e2012-30013-x
- Lamadie, F., & Delmas, F. (2005, December). Remote Alpha Imaging in Nuclear Installations: New Results and Prospects. *IEEE Transactions in Nuclear Science*, 52(6), 3035 - 3039.

- Lindner, M., & Elstein, S. (1998). Solar Blind and Bispectral Imaging with ICCD, BCCD and EBCCD Cameras. *Proceedings of SPIE Conference on Imag Intensifiers and Applications*, 22 - 31.
- Lindner, M., & Elstein, S. (1999). *Daylight Corona Discharge Imager*. Lenox, MA: EPRI Energy Delivery and Utilization Center.
- Lissberger, P., & Wilcock, W. (1959). Properties of All-Dielectric Interference Filters. II. Filters in Parallel Beams of Light Incident Obliquely and in Convergent Beams. *Journal of the Optical Society of America V. 49 No. 2*, 126 - 130.
- Lofthus, A., & Krupenie, P. (1977). The Spectrum of Molecular Nitrogen. *Journal of Physics and Chemical Reference Data*, 6, 113.
- Montgomery, R., Cowie, E., Hoek, M., Keri, T., & Seitz, B. (2012). Multianode photomultiplier tube studies for imaging applications. *Nuclear Instruments and Methods in Physics Research*, 326 - 329.
- National Institute of Standards and Technology. (2018, 02 20). *NIST: X-Ray Mass Attenuation Coefficients - Tungsten*. Retrieved from NIST: X-Ray Mass Attenuation Coefficients: <https://physics.nist.gov/PhysRefData/XrayMassCoef/ElemTab/z74.html>
- Nikon. (1984). *UV-Nikkor 105 mm f/4.5 Instruction Manual*. Tokyo, Japan: Nikon.
- Parker, L. (1958). *The Sources of Early Teller Light*. Lawrence Radiation Laboratory. Livermore, California: University of California.
- Princeton Instruments. (2012). *ProEM+ System Manual*. Trenton, NJ: Princeton Instruments.
- Rashband, W. (1997-2006). U.S. National Institutes of Health: ImageJ. *ImageJ*. Bethesda, Maryland, USA. Retrieved from <https://imagej.nih.gov/ij/>
- Reichman, J. (1998). *Handbook of Optical Filters for Fluorescence Microscopy*. Brattleboro, VT: Chroma Technology Corp.
- Rosado, J., Blanco, F., & Arqueros, F. (2010). Comparison of available measurements of the absolute air-flourescence yield. *Journal of Astroparticle Physics* 34, 164-172.
- Rosado, J., Blanco, F., & Arqueros, F. (2014). On the absolute value of the air-fluorescence yield. *Astroparticle Physics* 55, 51-62.
- Sand, J. (2016). *Alpha Radiation Detection via Radioluminescence of Air*. Tampere University of Technology. Tampere, Finland: Tampere University of Technology. Vol. 1449.
- Sand, J., & Ihantola, S. (2014). Radioluminescence yield of alpha particles in air. *New Journal of Physics* 16.
- Sand, J., Ihantola, S., & Perajarvi, K. (2015). Imaging of alpha emitters in a field environment. *Nuclear Instruments and Methods in Physics Research A*, 13-19. doi:10.1016/j.nima.2015.01.087

- Sand, J., Nicholl, A., & Hrncsek, E. (2016). Stand-off Radioluminescence Mapping of Alpha Emitters Under Bright Lighting. *IEEE Transactions on Nuclear Science*, Vol 63, No 3, 1777 - 1783.
- Sand, J., Nicholl, A., Hrncsek, E., Toivonen, H., Toivonen, J., & Perajarvi, K. (2016). Stand-Off Radioluminescence Mapping of Alpha Emitters Under Bright Lighting. *IEEE Transactions on Nuclear Science*, 63(3), 1777 -1783.
- Stolarski, R., & Dulock, V. (1967). Electron impact cross sections for atmospheric species: 2 molecular nitrogen. *Journal of Geophysical Research*, 3953 - 3960.
- Sze, S., & Kwok, K. (2007). *Physics of Semiconductor Devices 3rd Ed.* Hoboken, NJ: John Wiley & Sons.
- Tatischeff, I. (1970). Specific excitation of N₂ and specific ionization by 4.3 MeV alpha particles. *The Journal of Chemical Physics*, 503 - 508.
- Thompson, C., Barritt, E., & C., S.-T. (2016). Predicting the air fluorescence yield of radioactive sources. *Radiation Measurements*, 88, 48 - 54.
- UQG Optics. (2018, 01 29). *UV Fused Silica Windows*. Retrieved from UQG Optics: UQG Optics, UV Fused Silica—Spectrosil—Data Sheet. Available online: <http://www.uqgoptics.com/pdf/>
- Valk, F. (2010). Measurement of collisional quenching rate of nitrogen states. *Journal of Physics D: Applied Physics*.
- Waldenmaier, T. (April 2006). *Spectral resolved Measurement of the Nitrogen Fluorescence Yield in Air induced by Electrons*, PhD Dissertaiton. Karlsruhe Research Center, Institute for Nuclear Physics.

VIII. APPENDICES

Appendix A: Andor camera automation code

rem This script runs every permutation of time, temperature and binning settings defined below

```
rem TEST CONFIGURATIONS
rem Must have at least two entries in each file
rem ACQ time settings (10,30,100,300,1000,3000)
rem Temperature Settings (-100,-90,-80,-70,-60,-50,-40,-30)
rem Horizontal binning settings (1,2,4,8,16,32)
rem Vertical binning settings (1,2,4,8,16,32)

rem LOAD FILES
ACQ$="\\sn1\collaborative\NFRadOpt\ODR\Orion-DC\Lab Testing\Bintesting\Script\ACQ.txt"
Temp$="\\sn1\collaborative\NFRadOpt\ODR\Orion-DC\Lab Testing\Bintesting\Script\Temp.txt"
HBin$="\\sn1\collaborative\NFRadOpt\ODR\Orion-DC\Lab Testing\Bintesting\Script\HBin.txt"
VBin$="\\sn1\collaborative\NFRadOpt\ODR\Orion-DC\Lab Testing\Bintesting\Script\Vbin.txt"

rem IMPORT DATA to DATASET
loadasciixY(#111,ACQ$)
loadasciixY(#222,Temp$)
loadasciixY(#333,HBin$)
loadasciixY(#444,VBin$)

rem CLOSE WINDOWS FOR STORED SETTINGS
rem CloseWindow(#111)
rem CloseWindow(#222)
rem CloseWindow(#333)
rem CloseWindow(#444)
```

```

rem INITIATE saving director
dirname$= "\\sn1\collaborative\NFRadOpt\ODR\Orion-DC\Lab Testing\Bintesting\RawData\"

rem DEFINE Camera Name
cameraname$="Andor"

rem DEFINE Source Name
sourcename$="LensCapped"

rem DEFINE Filter Name
filtername$ = "340nm_BP10nm"

rem DEFINE Light Configuration
lightconfig$="Dark"

rem INITIATE COUNTERS
acqstep= 1
tempstep= 1
Hbinstep= 1
Vbinstep= 1

rem Set camera up for single scan
SetAcquisitionMode(1)
rem Set up acquisition for signal
SetAcquisitionType(0)
rem Start cooler
cooler(1)

rem BEGIN RUN LOOP
rem VERSION3 (3-layer Temp - Time - Bin) This run takes approx 60 hours to complete
While tempstep<=4
    rem Setting temperature

```



```

setTemperature(#222(tempstep))
rem 15 min temperature stabalization time
delay(900000)
rem Restart the ACQ counter for the next temperature
acqstep = 1
While acqstep<=6
    rem set count time, one collection, 5 second pause between acquisitions
    setAccumulate(#111(acqstep),1,5)
    rem Restart binning counters for the next count time
    Hbinstep =1
    Vbinstep=1
    While Hbinstep<=6
        rem Set Hbin and Vbin values
        SetHBin(#333(Hbinstep))
        setVBin(#444(Vbinstep))
        rem Run Acquisition
        run()
        rem FILENAMING
        fname$=dirname$+cameraname$+"_"+sourcename$+"_"+filtername$+str$(#111(acqstep))+
            "s"+"_"+str$(#222(tempstep))+"degC_"+lightconfig$+"_"+str$(#333(Hbinstep))+
            "x"+str$(#444(Vbinstep))+".sif"
        print(date$()+" "+time$())
        print(fname$)
        save(#0,fname$)
        closeWindow(#0)
        closewindow(#1)
        Hbinstep = Hbinstep+1 rem Advance to the next bin settings
        Vbinstep = Vbinstep+1
    wend
    acqstep = acqstep + 1 rem Advance to the next count time
wend
tempstep = tempstep +1 rem Advance to the next temperature
wend

```

Appendix B: ImageJ Image processing code

```
run("Enhance Contrast...", "saturated=0.4");
run("Flip Vertically");
run("Jet");
run("Set Measurements...", "area mean standard min bounding
redirect=None decimal=3");
makeRectangle(625, 480, 16, 16);
roiManager("Add");
roiManager("Select", 0);
roiManager("Rename", "Signal");
makeRectangle(100, 100, 16, 16);
roiManager("Add");
roiManager("Select", 1);
roiManager("Rename", "Noise1");
makeRectangle(908, 100, 16, 16);
roiManager("Add");
roiManager("Select", 2);
roiManager("Rename", "Noise2");
makeRectangle(100, 908, 16, 16);
roiManager("Add");
roiManager("Select", 3);
roiManager("Rename", "Noise3");
makeRectangle(908, 908, 16, 16);
roiManager("Add");
roiManager("Select", 4);
roiManager("Rename", "Noise4");
roiManager("Select", 0);
roiManager("Measure");
roiManager("Select", 1);
roiManager("Measure");
roiManager("Select", 2);
roiManager("Measure");
roiManager("Select", 3);
roiManager("Measure");
roiManager("Select", 4);
roiManager("Measure");
roiManager("Show All");

filepath="O:\\ODR\\Orion-DC\\Lab Testing\\Andor Temperature
Measurements\\CoolerTest\\ScriptTest\\Output\\";
filename=getTitle();
fileext=".xls";
savename=filepath+filename+fileext;
savepicname = filepath+filename+"Processed";

Signal=getResult("Mean",0);
Noise1=getResult("Mean",1);
Noise2=getResult("Mean",2);
Noise3=getResult("Mean",3);
Noise4=getResult("Mean",4);
AvgNoise=(Noise1+Noise2+Noise3+Noise4)/4;
```

```

AvgStdevNoise=(getResult("StdDev",1)+getResult("StdDev",2)+getResult("StdDev",3)+getResult("StdDev",4))/4;
Contrast=abs(Signal - AvgNoise)/AvgNoise;
SNR = Signal/AvgStdevNoise;
Header = "Filename,Contrast,SNR";
Data=filename+", "+Contrast+" "+SNR+";
print(Data);
saveAs("Results",savename);
roiManager("reset")

open("O:\ODR\Orion-DC\Lab Testing\Andor Temperature
Measurements\CoolerTest\ScriptTest\target.tif");
selectWindow("target.tif");
run("Enhance Contrast...", "saturated=0.4");
run("Add Image...", "image=filename x=0 y=0 opacity=50");
makeRectangle(625, 480, 16, 16);
roiManager("Add");
roiManager("Select", 0);
roiManager("Rename", "Signal");
makeRectangle(100, 100, 16, 16);
roiManager("Add");
roiManager("Select", 1);
roiManager("Rename", "Noise1");
makeRectangle(908, 100, 16, 16);
roiManager("Add");
roiManager("Select", 2);
roiManager("Rename", "Noise2");
makeRectangle(100, 908, 16, 16);
roiManager("Add");
roiManager("Select", 3);
roiManager("Rename", "Noise3");
makeRectangle(908, 908, 16, 16);
roiManager("Add");
roiManager("Select", 4);
roiManager("Rename", "Noise4");
roiManager("Show All");
roiManager("UseNames", "true");
roiManager("Show All with labels");
selectWindow("target.tif");
run("Scale Bar...", "width=16 height=4 font=14 color=White
background=None location=[Lower Right] bold");
run("Labels...", "color=white font=12 show use");
run("From ROI Manager");
run("Labels...", "color=white font=12 show use");
saveAs("Jpeg", savepicname);

roiManager("reset")
IJ.deleteRows(0, 4);

```

Appendix C: Transmissivity Curves of Single Filters

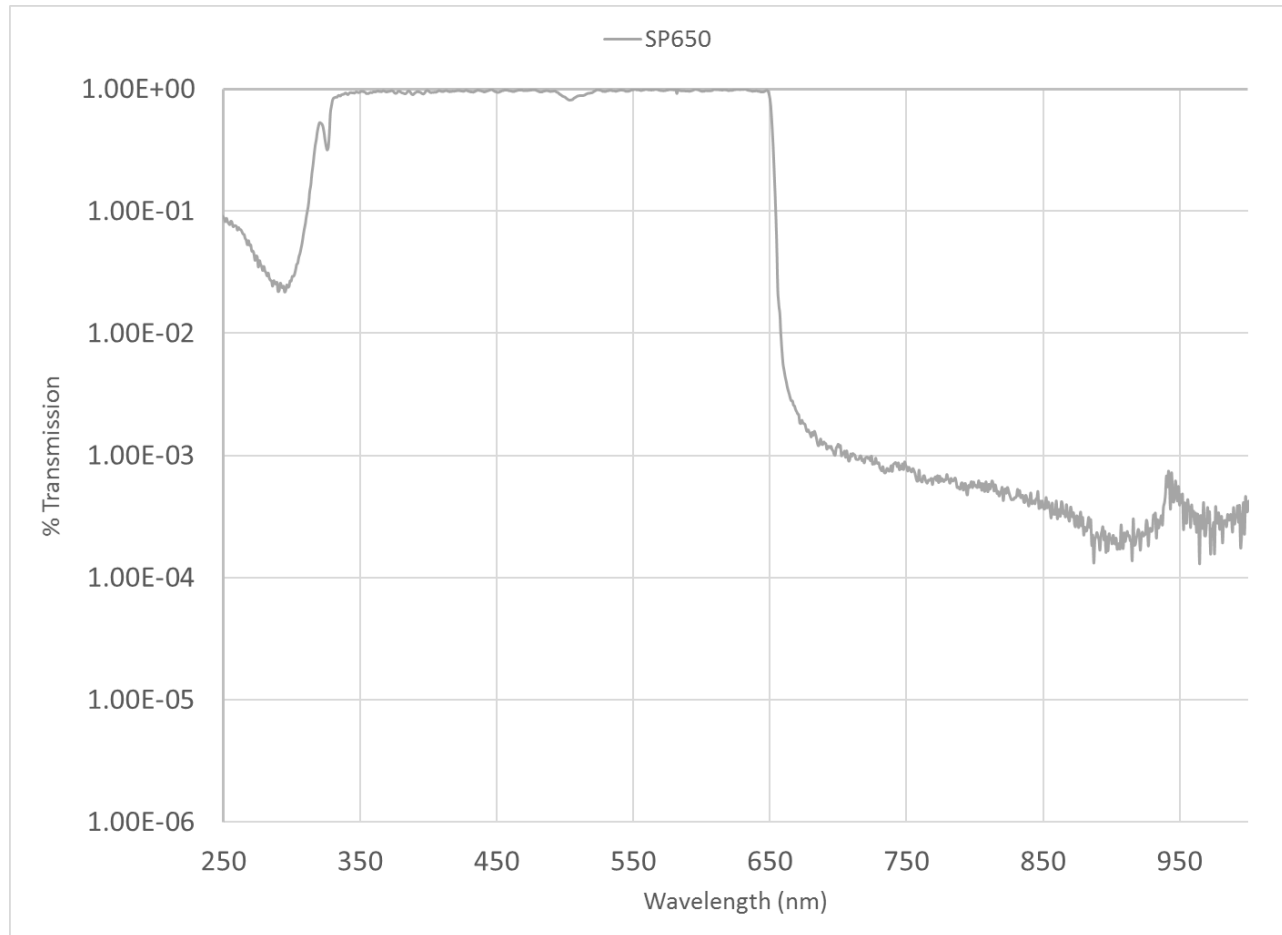


Figure 28: SP650 Transmission

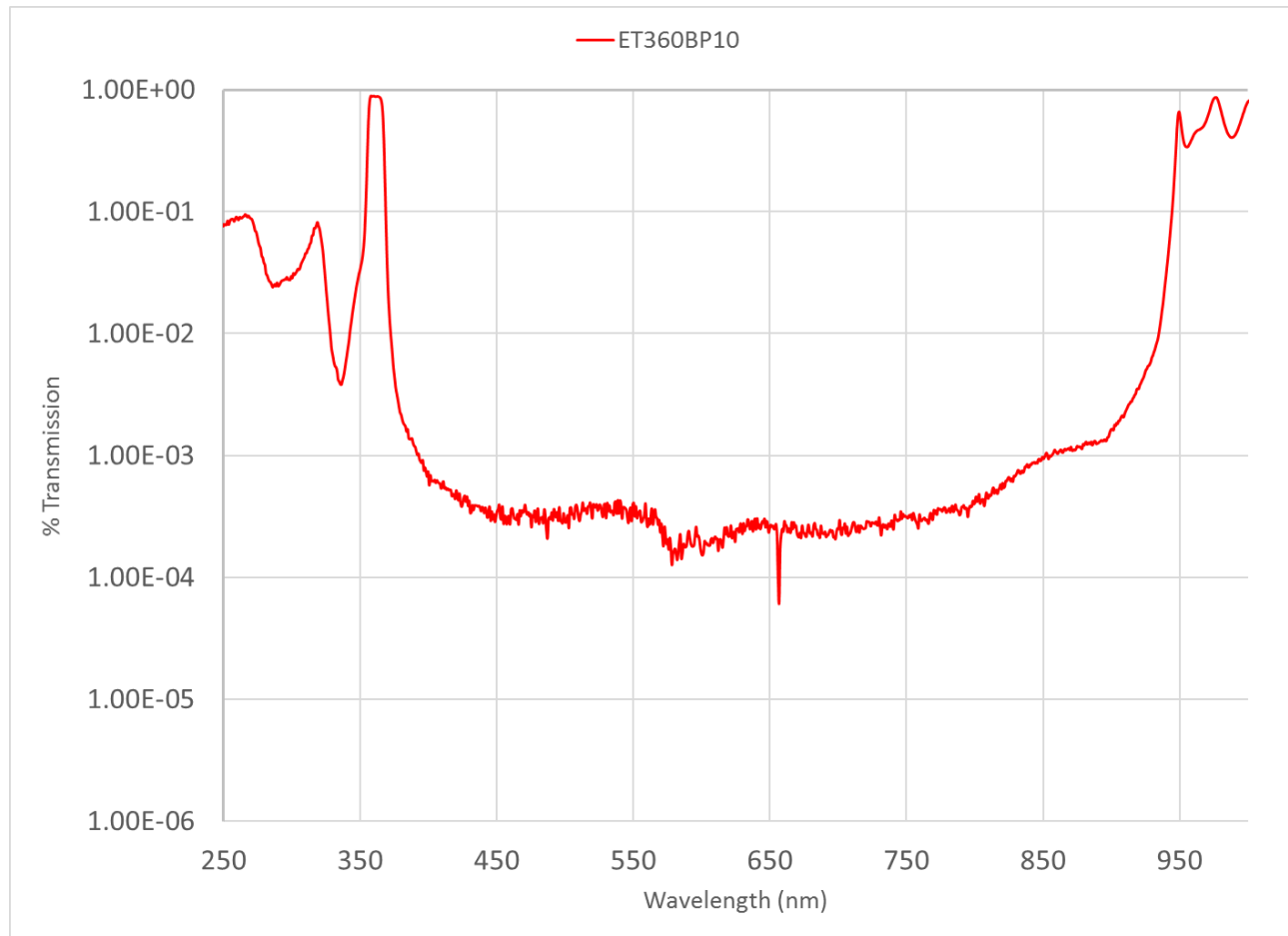


Figure 29: ET360BP10 Transmission

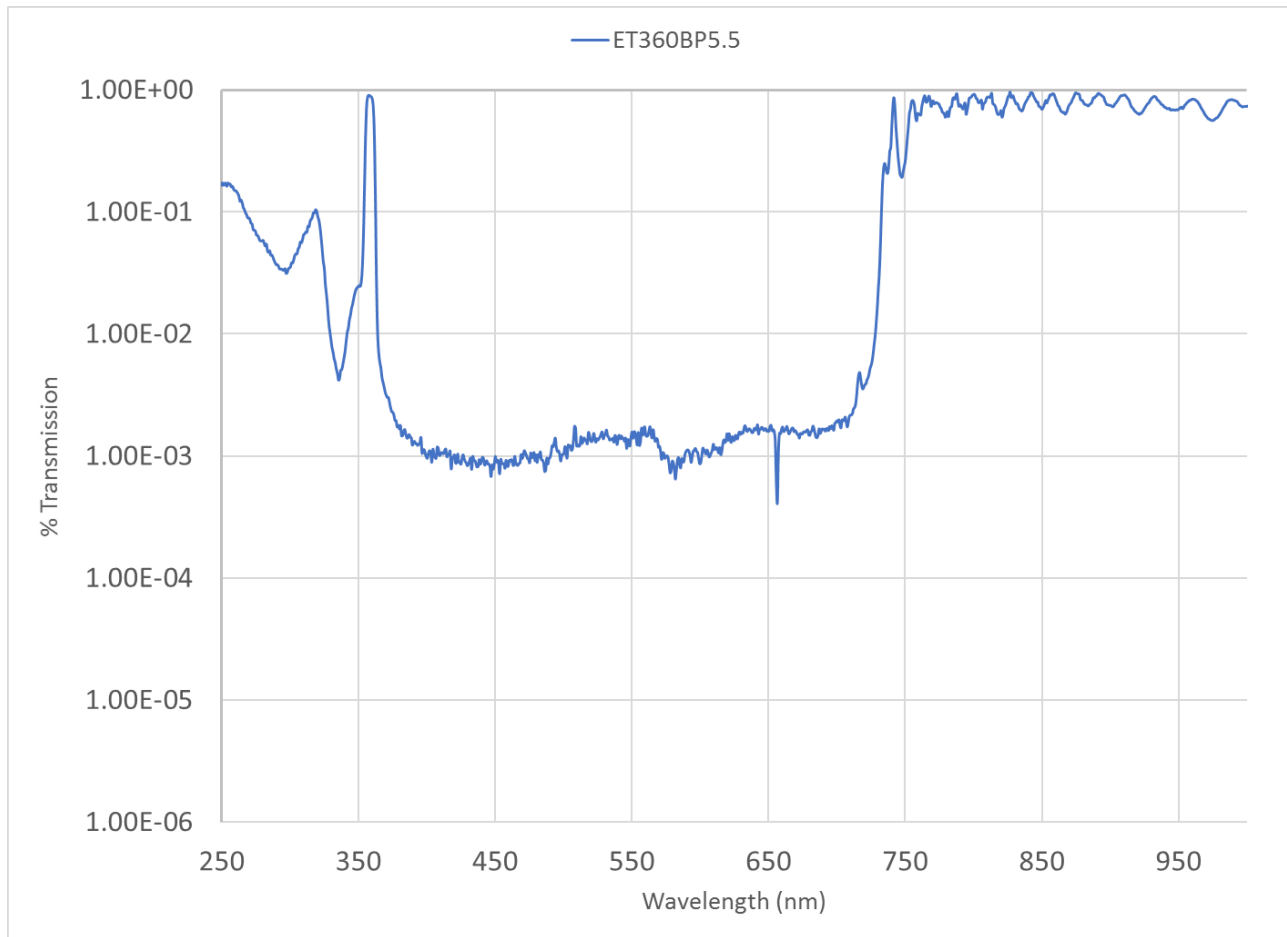


Figure 30: ET360BP5.5 Transmission

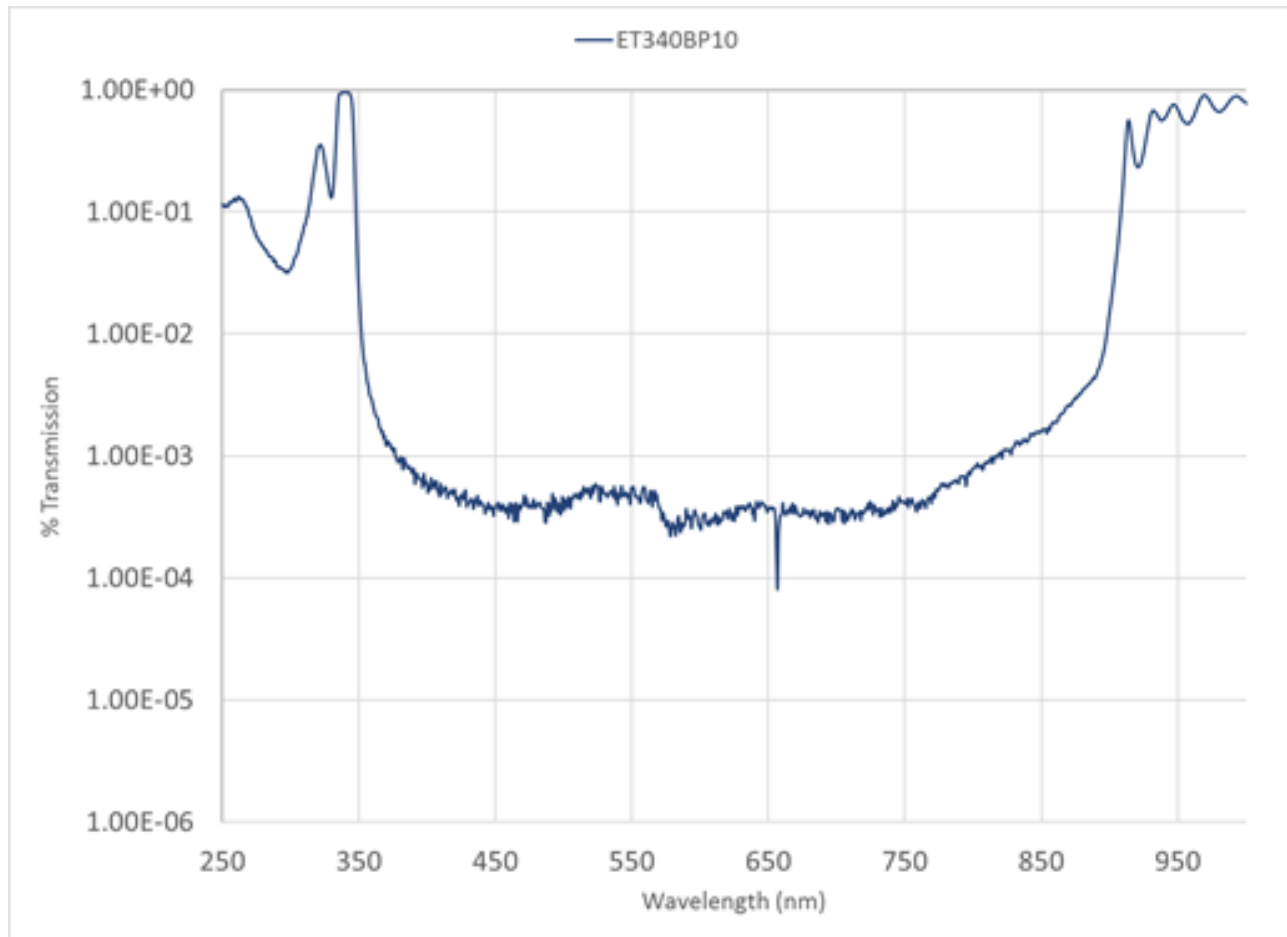


Figure 31: ET340BP10 Transmission

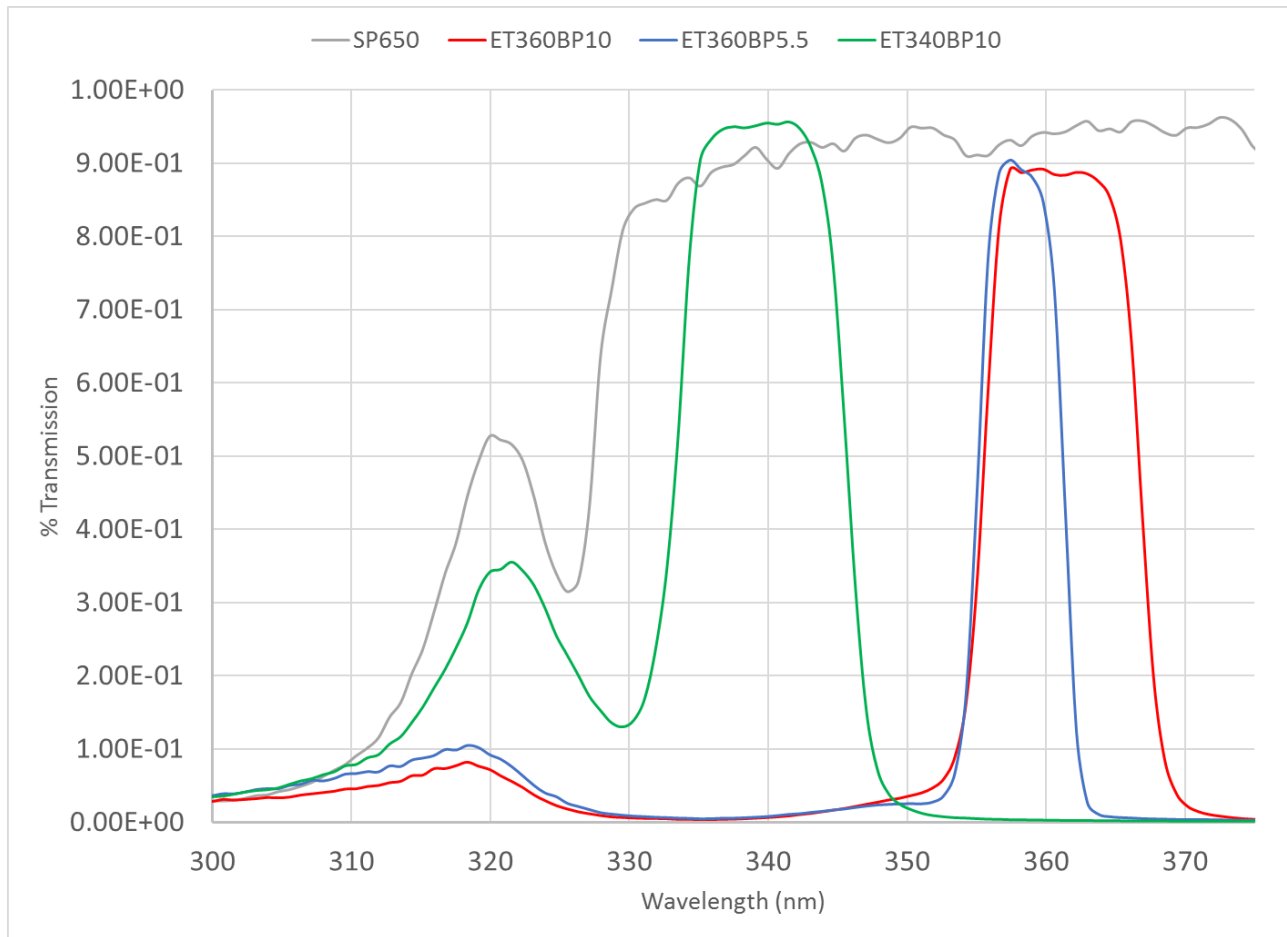


Figure 32: Single-filter transmission zoomed scale comparison

Appendix D: Transmissivity Curves of Filter Stacks

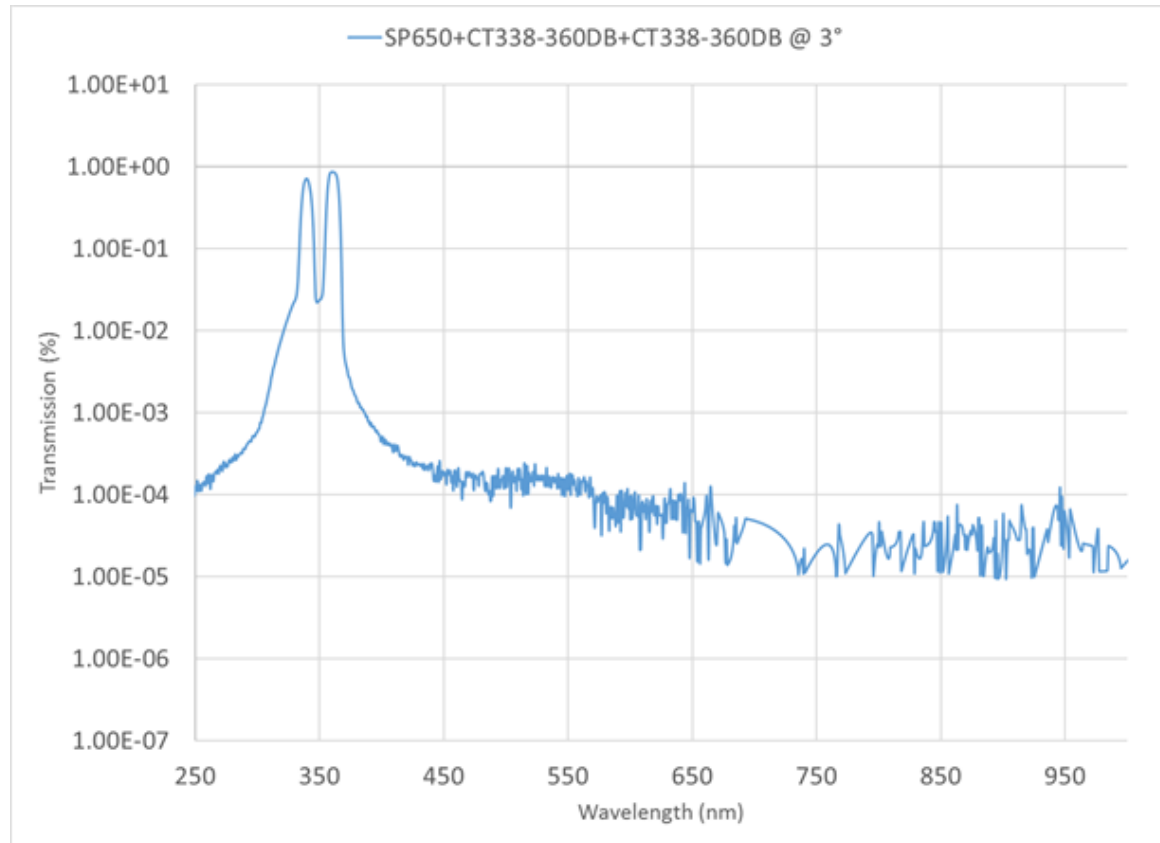


Figure 33: 2X Dual Band filter stack transmission, full scale

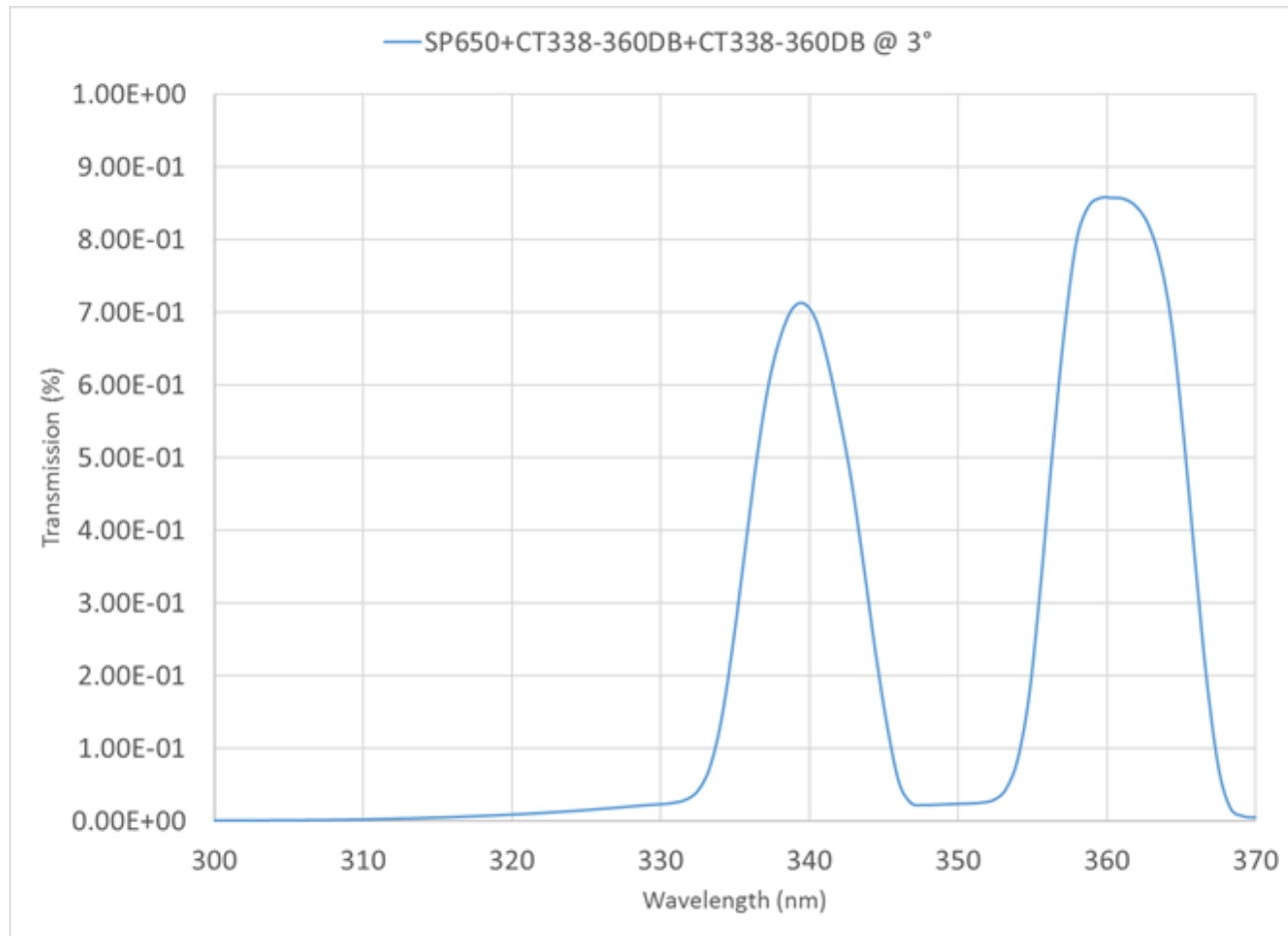


Figure 34: 2X dual band filter stack transmission, zoomed scale

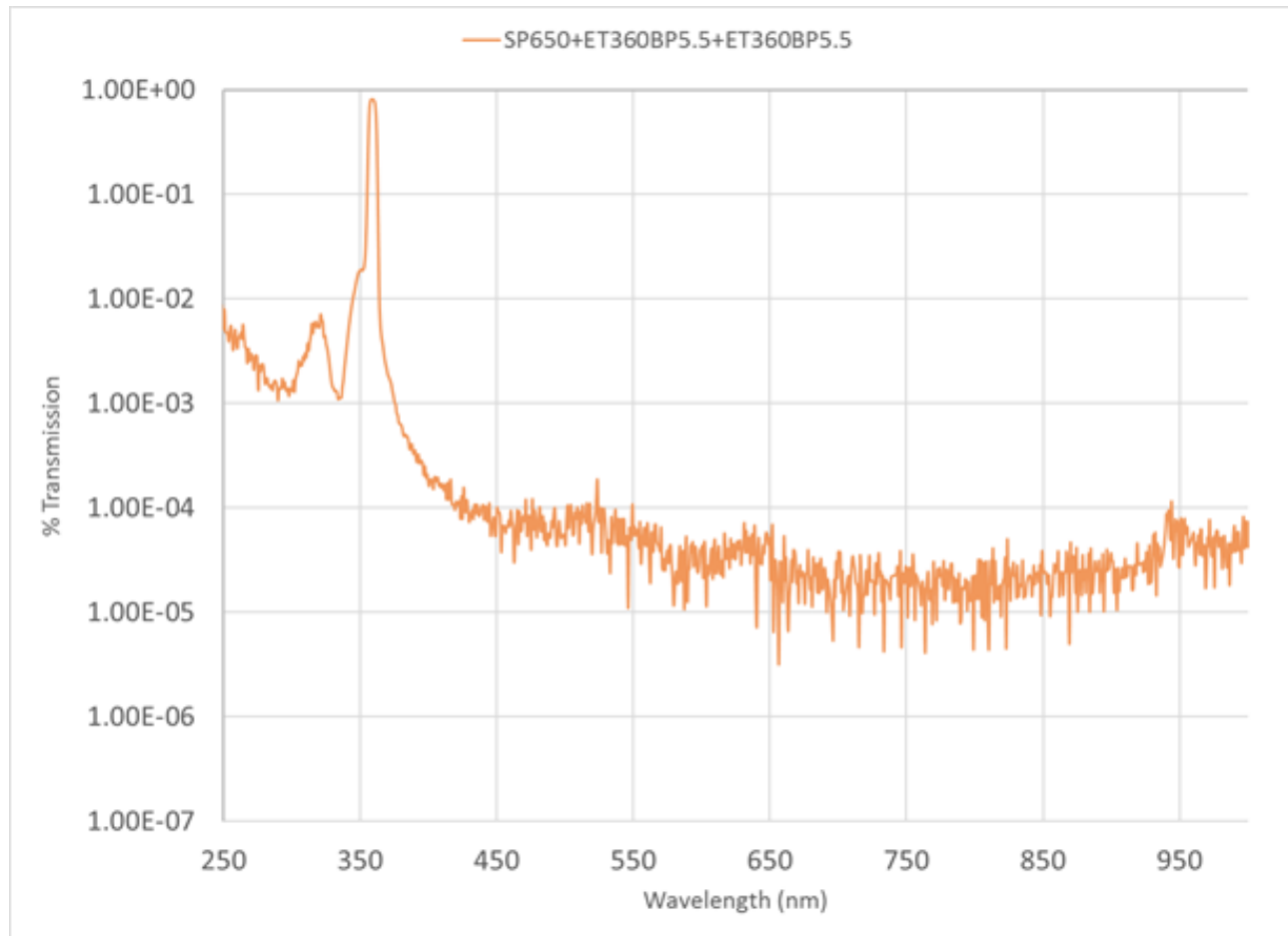


Figure 35: 2X ET360BP5.5 filter stack transmission, full scale

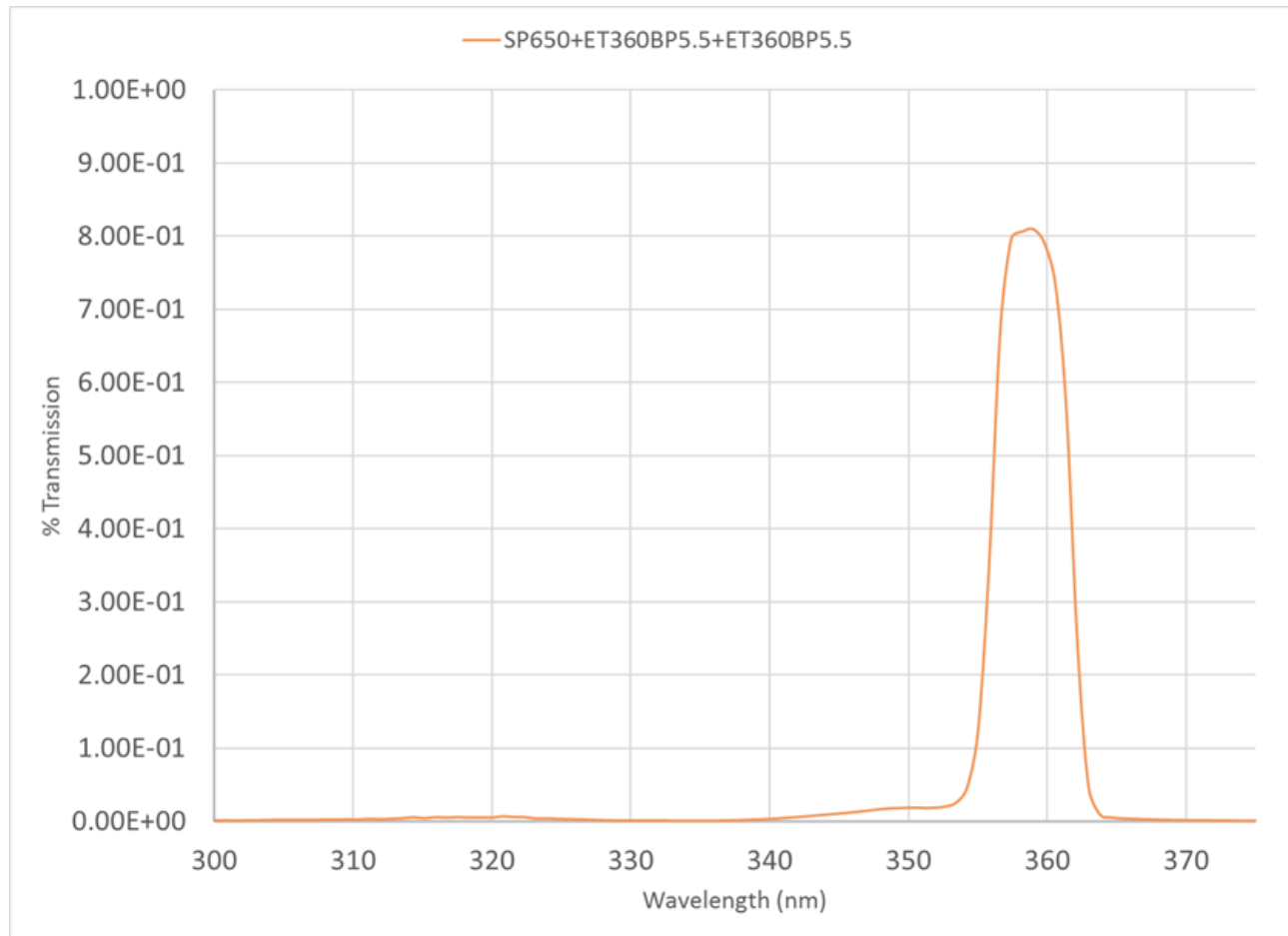


Figure 36: 2X ET360BP5.5 filter stack transmission, zoomed scale

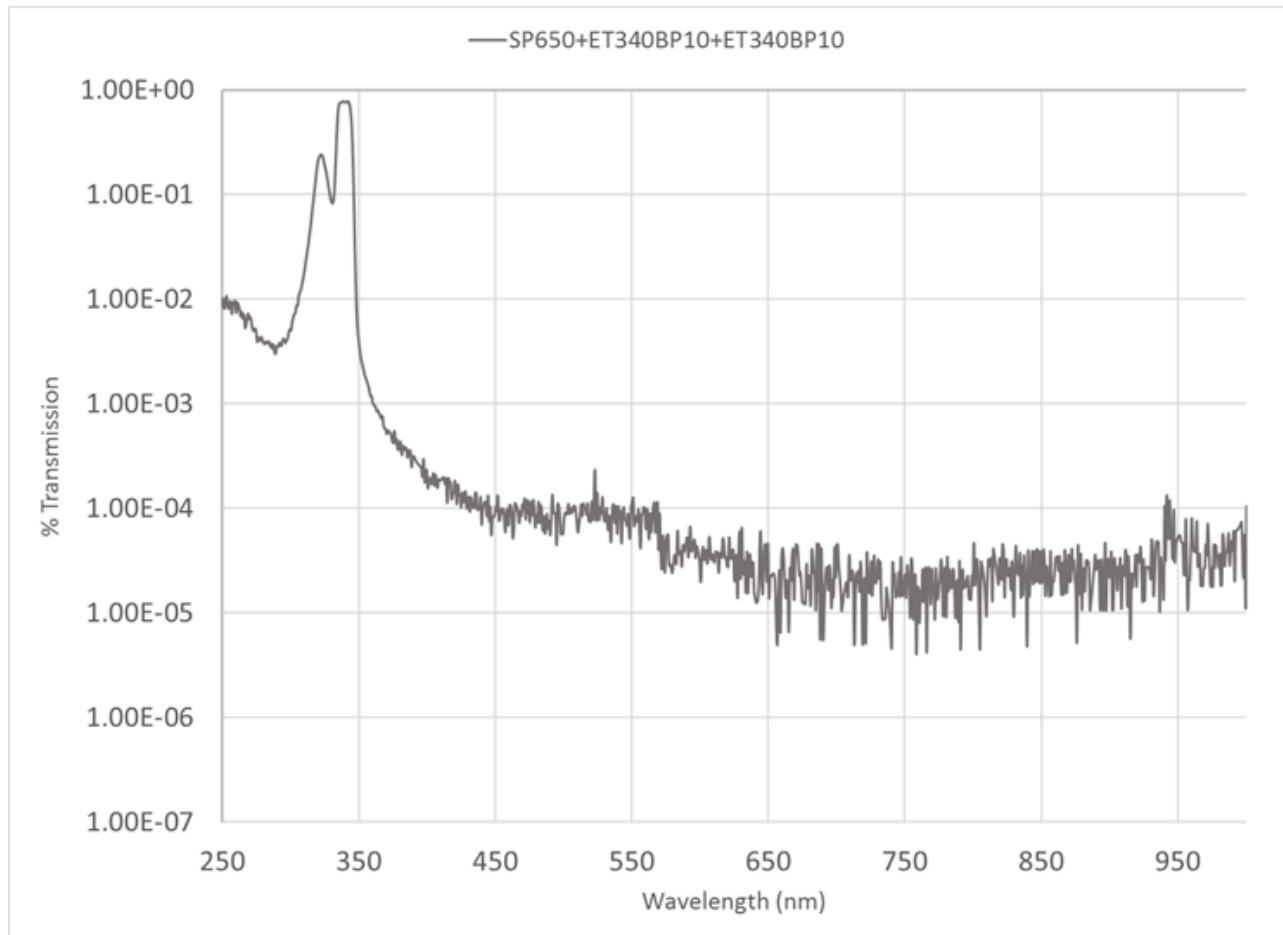


Figure 37: 2X ET340BP10 filter stack transmission, full scale

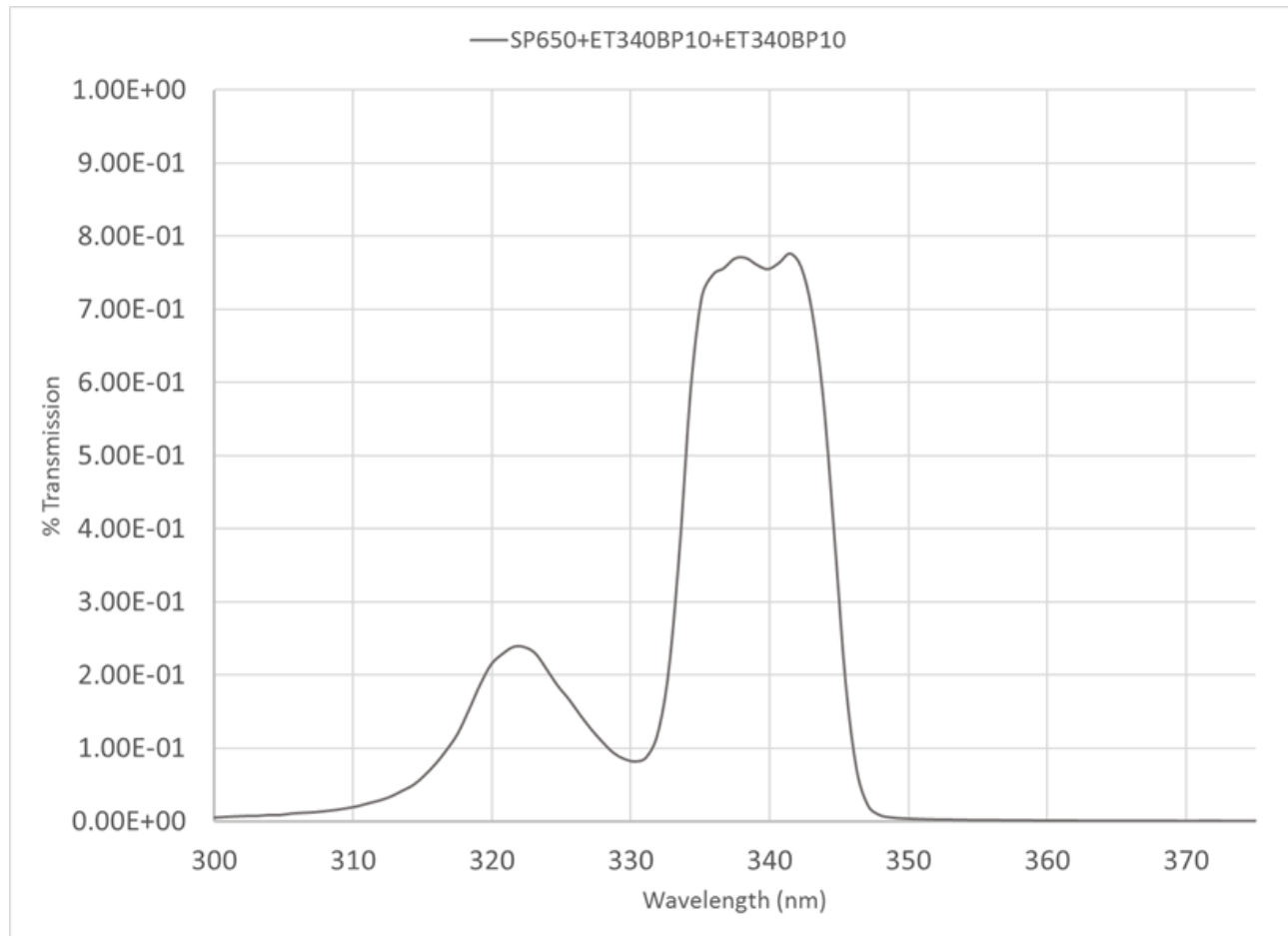


Figure 38: 2X ET340BP10 filter stack transmission, zoomed scale